Analysis of Non-Uniform Cathode Emission and Backward Wave Oscillations in a Traveling Wave Tube

by

Abhijit Jassem

A dissertation submitted in partial fulfillment
of the requirements for the degree of
Doctor of Philosophy
(Nuclear Engineering and Radiological Sciences)
in the University of Michigan
2021

Doctoral Committee:

Professor Yue Ying Lau, Chair
Professor Ronald M. Gilgenbach
Professor Ryan McBride
Professor Eric Michielssen

Abhijit Jassem

ajassem@umich.edu

ORCID iD: 0000-0003-2974-4882

Dedication

This thesis is dedicated to my family for their unending support and love

Acknowledgements

This thesis would not have been possible without the support of my mentors, my friends and colleagues, and my family.

I have been extremely fortunate to have the opportunity to work with a number of world class scientists. First, I would like to thank my advisor, Professor Y. Y. Lau, for his guidance, wisdom, kindness, and patience. It has truly been an honor to work with such an esteemed scientist and remarkable educator and I will be eternally grateful to him. I must also thank Dr. David Chernin for his invaluable contributions, which much of the work in this thesis relies on. Professor Ryan McBride has been a wonderful source of inspiration and knowledge to me since he joined Michigan, shortly after I did. I have always appreciated the time he has taken for me, whether I was his student, teaching assistant, or simply asking him for advice. Next, I must thank Professor Ronald Gilgenbach for all his motivation and support as well as his unique insights into the world of vacuum electronics. I would also like to thank Professor Eric Michielssen, who taught an excellent course on numerical electromagnetics and readily joined my thesis committee on extremely short notice. I am indebted to Professor Ágúst Valfells for graciously inviting me to work on simulations with him at Reykjavik University and allowing me to stay with his family; it was an unforgettable experience. Special thanks also go to Dr. Bruce Carlsten, Dr. Muhammed Zuboraj, and Dr. Kimberley Nichols for offering me an internship at Los Alamos National Laboratory. I must also acknowledge the faculty and broader plasma physics community at Michigan, particularly Professor Mark Kushner and Professor John Foster, who has always been a wonderful person to talk to. Garnette Roberts has been eminently helpful and supportive as the

graduate program coordinator. Lastly, I would be remiss if I did not acknowledge Professor Allen Garner at Purdue University, who first gave me the chance to participate in undergraduate research and fostered my interest in plasma physics. I still remember our first meeting, during which he plotted out a detailed research and study plan all the way to graduate school, despite me being just a sophomore. Without his mentorship, I simply would not be here today.

In light of the coronavirus pandemic, it has never been clearer how much we rely on our friends, family, and support system. My fellow graduate students Drew Packard, Dr. Foivos Antoulinakis, and Dr. Patrick Wong have taught me so much and been wonderful friends. As an undergraduate researcher at Purdue, I was inspired by my senior group members Dr. Russell Brayfield, Dr. Andrew Fairbanks, and Dr. Amanda Loveless. I must also thank the many other friends who have done so much for me and kept me going: Evan, Julio, Joe, Arnaud, Tess, Emily, Marlon, Cara, João, Landon, Ilka, Jesse, Janis, Vasupradha, Neelesh, Shane, and countless others. To Taïna Jean-Louis, thank you for being a wonderful partner in this stressful time and for teaching me how to grow past my limitations.

My family has been an incredible source of strength and love throughout my life. Ammumma, I couldn't have asked for a more loving grandmother. Chechi, thank you for being a wonderful sister and for teaching me to live life more fully. Amma and Uppa, I can't thank you enough for all your sacrifices, for believing in me, and for loving me no matter what.

This research was supported by the Defense Advanced Research Projects Agency (DARPA) with Leidos under Contract HR0011-16-C-0080, by L3Harris Electron Devices Division, and by the Air Force Office of Scientific Research (AFOSR) Grants No. FA9550-15-1-0097, No. FA9550-14-1-0309, No. FA9550-18-1-0153.

Table of Contents

List of Tables

List of Figures

Abstract

The traveling wave tube (TWT) is a vacuum electronic device that provides wide bandwidth and high gain amplification of radio-frequency signals for applications in radar, electronic warfare, and satellite communications. The TWT operates by transferring the kinetic energy of an electron beam to the input signal via synchronous interaction with a periodic circuit structure. In this thesis, we theoretically analyze various realistic effects that are of contemporary interest.

The classical theory describing TWTs was developed by J. R. Pierce some 70 years ago. A recent exact theory on a tape-helix TWT concluded that Pierce's theory omitted the potentially important detuning effect on the circuit mode at high beam currents. However, this exact theory excluded ohmic losses in the circuit, which are always present in a realistic TWT. This thesis included circuit loss in the exact theory. We find that the exact and Pierce's classical theories agree well only in a restricted frequency range. The discrepancies are due to the effect of higher order circuit modes and their space harmonics, included in the exact theory but neglected in Pierce's classical theory.

Backward wave oscillations (BWOs) pose a threat to the stable operation of TWTs. They are caused by the interaction of the electron beam with the backward propagating wave on the circuit. The threshold condition for BWO excitation was formulated by H. R. Johnson. This thesis extends Johnson's theory to include the effects of random manufacturing errors on the circuit, motivated by recent attempts to operate TWT in the terahertz regime. At such high frequencies, the circuit size is substantially reduced, making manufacturing errors proportionally

much more significant. We showed that, surprisingly, Johnson's threshold beam current required for BWO excitation is insensitive to the effect of random manufacturing errors whose presence could alter the delicate synchronous interaction between the electron beam and the circuit's backward wave. An interpretation of this unexpected result is given. We found, however, that the threshold conditions for BWO excitation depend sensitively on the phase and magnitude of the reflection coefficients at the ends of the TWT.

Lastly, we consider thermionic cathodes used in TWTs. To preserve cathode life, and therefore the life of the TWT and the satellite carrying it, it is imperative to operate the cathode at the lowest possible temperature that provides sufficiently high current. Thus, thermionic cathodes are typically operated near the transition between thermionic emission and space-charge-limited emission. In the plot of anode current vs cathode temperature (Miram curve), this transition is smooth and broad in experiments, a feature no physical theory can replicate to date. A sharp and abrupt transition is highly desirable, usually simulated but difficult to achieve in practice. This thesis made an attempt to solve this outstanding puzzle. An analytic theory is formulated to show how non-uniform emission arising from 2-dimensional work function variations on the cathode surface can affect the shape and location of this transition. Also addressed are various factors which could affect the Miram curve, such as strongly-emitting local spots, various non-emitting regions, and the emission feature size. We show that the anode current is still governed by the 1-dimensional Child-Langmuir law, as if the entire cathode was emitting despite the existence of significant non-emitting areas. The analytical theory is in excellent agreement with particle-in-cell simulation.

Chapter 1 Introduction

Vacuum electronic microwave sources are a class of device employed in a wide range of applications including satellite communications, radar, plasma heating, charged particle accelerators, and various defense applications [1], [2]. These devices generally operate by transferring the kinetic energy of an electron beam into electromagnetic radiation, typically via interaction with a periodic electromagnetic structure. Although the science of vacuum electronics may be considered mature, having originated in the early 20th century, the field remains an active area for scientific research due to its evolving needs. These include enhanced performance in communication satellites which face increasing demands but crowded orbital space, and high power microwave sources for various defense and homeland security applications. Contemporary research includes further increasing the power and frequency of these devices to the gigawatt and terahertz regimes, as well as reducing costs and optimizing performance [1]–[4]. One widely used microwave device is the traveling wave tube (TWT), which provides high efficiency, wide bandwidth, low noise, and high gain amplification of radiofrequency (RF) signals in a compact and robust package [4]. As such, they are the final amplifiers of choice for radar, electronic warfare, or satellite communication systems. In this thesis, we will explore several issues in modern TWTs by incorporating realistic effects such as random manufacturing errors and cathode non-uniformities into theoretical models and assessing how they impact the operation and design of TWTs.

1.1 Traveling wave tubes

The traveling wave tube is a linear beam device that amplifies an input radiofrequency signal by extracting the kinetic energy from a DC electron beam. The input signal is fed into one end of the tube and is propagated down a periodic structure (for example, a helix) with the electron beam. As the signal and beam travel down the tube, a mutual interaction between the two continuously transfers the beam's kinetic energy to the signal, resulting in an amplified output signal that is extracted at the downstream end of the tube.

The history of the invention of the traveling-wave tube is somewhat controversial. Although the possibility of such a traveling wave interaction between a beam and a signal was recognized as early as 1933 by Haeff [3], [5], [6], it was not until the 1940s that Nils Lindenblad in the US [7] and later, Rudolf Kompfner in the UK [8] independently designed vacuum tubes with an electron beam propagating down the axis of a helix that could amplify an RF signal. At the time, the most powerful microwave amplifier was the klystron [3]. However, the klystron only allowed the amplification mechanism to occur in discrete regions near the klystron cavities, limiting the coupling between the beam and wave as well as the device's bandwidth. Kompfner, recognizing this, sought to replace this discrete interaction with a continuous interaction using a traveling wave, as he later [9] described in an account of the TWT's invention, with which he was widely credited. However, a recent article [10] claims that Haeff sold his patent, along with a working prototype, to RCA in 1934, six years before Lindenblad, also working at RCA, filed for a patent on an improved TWT. This was also well before Kompfner invented and tested his TWT, in 1943. Regardless, the powerful implications of the device were recognized, promoted, and described theoretically using a small signal analysis [11] by J. R. Pierce at Bell Labs, who

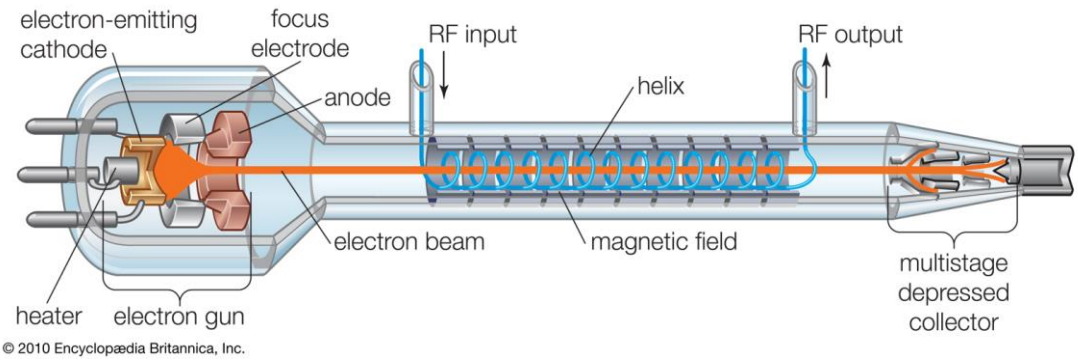

Figure 1.1: Schematic of a traveling wave tube (TWT). Image from [25].

later became known as the "father of the communication satellite". He soon published a book [12] that became the standard reference for the theory of traveling wave tubes [3], [13] as well as laying the foundations for the theory of other contemporary radiation sources, such as free electron lasers [1], [2], [14]–[19], Smith-Purcell radiators [15], [20], and gyrotron amplifers [2], [21]–[24]. Before we describe this mathematical theory in the following section, we will take a moment to describe the operating mechanism of the TWT in an intuitive, physical manner.

A schematic of a modern TWT is given in Figure 1.1 [25]. Although the device is complex, with many components, we may divide it into three stages: (i) generation of the electron beam, (ii) beam-circuit interaction region, and (iii) collection of the spent electron beam. In this thesis, we will only consider the physics in stages (i) and (ii).

1.1.1 The electron beam

In a TWT, the electron beam is generated by either boiling them off a hot thermionic cathode (thermionic emission) or by pulling them out of the cathode using strong electric fields (field emission); the former method is used in virtually all commercial TWTs [3]. The thermionic cathode is heated to some temperature T and readily emits electrons according to the Richardson-Dushman Law [26], [27]:

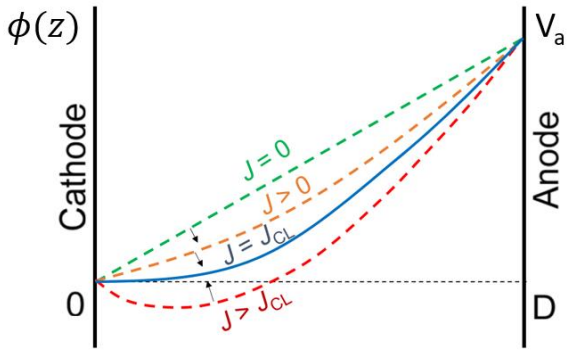

Figure 1.2: Potential profiles in a 1D diode with gap spacing *D* and gap voltage V_a for various values of injected current density *J*. The solid line denotes the steady state space-charge-limited current density J_{CL}. Image from [30].

$$J_{RD} = A_0 T^2 \exp\left(-\frac{\phi}{k_b T}\right) \tag{1.1}$$

where J_{RD} is the emitted electron current density, A_0 =1.201732 ×10^6 A/(m·K)^2 is the Richardson coefficient, k_b is the Boltzmann constant, and ϕ is the work function, which describes the energy required to liberate an electron from the metal cathode surface.

The emitted electrons are then accelerated and transported into the next stage of the TWT by a voltage V_a applied between the anode and cathode, which determines the kinetic energy of the beam. Neglecting relativistic effects, the beam's DC velocity is then:

$$v_0 = \sqrt{\frac{2eV_a}{m_e}} \tag{1.2}$$

where e is the electron charge and m_e is the electron mass. We further assume that the beam is monoenergetic, with no temperature effects, and that its motion is 1 dimensional, i.e. that there is an infinite axial magnetic field that confines the beam.

The anode-cathode (A-K) voltage V_a also sets the maximum current that may be extracted from the A-K gap. Consider the 1D planar diode in Figure 1.2 where the cathode is grounded and the potential at the anode is given by V_a. The potential distribution $\phi(z)$ within the gap is governed by Poisson's equation

$$\frac{d^2\phi(z)}{dz^2} = \frac{\rho}{\epsilon_0} \tag{1.3}$$

where ρ is the charge density and ϵ_0 is the permittivity of free space. If no electrons are emitted into the gap ($J = 0$, where J is the current density), then $\rho = 0$ and the potential distribution is simply given by the vacuum solution $\phi(z) = \frac{V_a}{D} z$ (dotted green curve, Figure 1.2). As the current density is increased ($J > 0$), the space charge of the emitted electrons depresses the potential distribution (dotted orange curve, Figure 1.2). However, if the current is increased further to some critical value J_{CL}, (solid blue curve, Figure 1.2). the density of the electrons near the cathode surface becomes so large that it depresses the potential such that the electric field is equal to zero at the cathode surface; this potential depression would reflect electrons back to the cathode with any further increase in the emission current beyond J_{CL}. Assuming zero electron emission velocity, this maximum current density J_{CL} may be calculated by solving Eq. 1.3 subject to the boundary condition $d\phi/dz = 0$ at $z = 0$ and is given by the Child-Langmuir law [28], [29]

$$J_{CL} = \frac{4}{9}\epsilon_0 \sqrt{\frac{2e}{m}} \frac{V_a^{3/2}}{d^2} \tag{1.4}$$

Under these assumptions, no steady state solution exists when the injection current density $J > J_{CL}$. This is the reason why J_{CL} is also known as the space-charge-limited current density. However, if electrons are allowed to be emitted with *non-zero* velocity, Poisson's equation does permit solutions where the potential is depressed below zero at some location into the gap (red dotted curve, Figure 1.2), allowing the steady state solution for injection current density J to exceed J_{CL} [30]. In this case, only the emitted electrons with a sufficiently high initial velocity can overcome the potential barrier to reach the anode, and the anode current density is still well

represented by Eq. (1.4) [3], [29], [31]. It is very important to note that J_{CL} is independent of cathode material, cathode temperature, and emission mechanism; it is a constraint imposed by the Poisson equation [30]. Thus, in a thermionic cathode operating at a fixed anode voltage V_a at a low temperature, the current reaching the anode is governed by the Richardson-Dushman law, Eq. (1.1), and the diode is said to operate in the temperature limited regime, because the anode current is limited by the operating temperature of the cathode. As the temperature of the cathode becomes very high, the anode current is limited by the Child-Langmuir law, Eq. (1.4), and the diode is said to operate in the space-charge-limited regime, because the anode current is limited by the constraint imposed on the space charge allowed in the diode, as described by the Poisson equation, or from a capacitance consideration [32]. The transition between these two regimes, as the cathode temperature increases, has great practical importance and will be studied in detail in in Chapter 4 of this thesis.

In general, the maximum steady state current allowed in a diode is a function of geometry and voltage. Of course, a real electron gun may not have a 1D planar diode geometry; the geometric effects are characterized by the gun perveance P, and the space-charge-limited current I_{SCL} is written as [3], [13]

$$I_{SCL} = PV_b^{\frac{3}{2}} = J_{SCL}S \tag{1.5}$$

where S is the beam cross-sectional area and J_{SCL} is the corresponding space-charge-limited current density. Equation (1.5) thus acts as an analogue to Ohm's Law for diodes.

Since the temperature of the cathode may fluctuate, the electron current will also vary considerably if the cathode is operated in the temperature-limited regime, i.e. according to Eq. (1.1) when $J < J_{SCL}$. It is therefore desirable to operate TWTs in the space-charge-limited regime to maintain a consistent electron current, where that electron current will also be the maximum

allowed. In fact, for reasons we will outline in Chapter 4, to preserve the working life of the cathode, TWTs are typically operated near the transition from temperature-limited to space-charge-limited emission, i.e., at the lowest cathode temperature with maximum anode current.

Given some current density J for a given electron gun configuration, we may also calculate the steady state electron number density $n_0 = \frac{J}{ev_0}$ in the drift region past the gun where the beam velocity becomes a constant. If there are no perturbations, the beam would continue down the tube with velocity v_0 and density n_0. However, a signal of frequency ω injected at the start of the beam-circuit interaction region (see Figure 1.1) would induce density perturbations on the beam with a characteristic propagation constant

$$\beta_e = \omega/v_0 \tag{1.6}$$

This simple relation $\omega = \beta v_0$ is known as the beam mode, where β is the wavenumber (usually designated as k in the plasma physics literature [33]).

1.1.2 The circuit wave

In a vacuum, electromagnetic signals travel at the speed of light c in free space in the form of transverse electric and magnetic (TEM) waves. However, for this signal to interact appreciably with the electron beam, which has a drift velocity v_0 ($v_0 < c$), they must both travel with similar velocities such that $v_p \approx v_0$, where v_p is the phase velocity component of the wave that co-propagates with the beam. The situation is analogous to that of a surfer and an ocean wave, as recognized by Haeff before he proposed the mechanism for a TWT [10]. If the surfer is stationary, any waves moving past them will only serve to bob them up or down. However, if the surfer paddles in the same direction as the wave to gain some velocity, the wave will then propel the surfer forward, properly making use of the wave's energy. Of course, in a TWT, we wish to

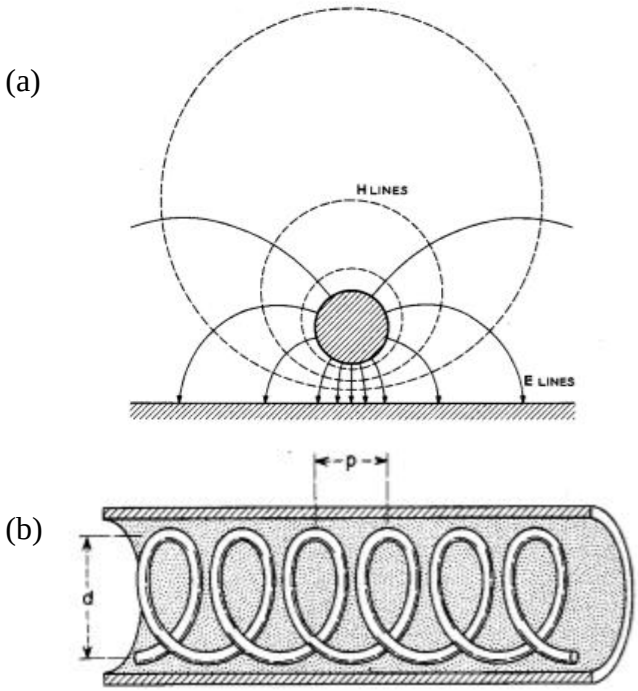

Figure 1.3: (a) Transmission line composed of a single wire above a ground plane (b) Single wire wrapped into a helix, surrounded by a conducting cylinder. Image from [13].

use the particle's (the surfer's) energy to make the wave stronger, but this principle of velocity synchronism still applies.

However, this raises the question: Since electrons cannot travel at the speed of light, how could they match the wave's velocity? The answer is to slow down the phase velocity of the wave in the direction of beam propagation through the use of a slow-wave structure (SWS). An ideal SWS would maintain the synchronism condition over a wide range of frequencies, allowing for broadband amplification, i.e. it must be non-dispersive. For this purpose, a helical SWS is unmatched. We may explain the reason in qualitative terms using Figure 1.3.

First, consider a metallic wire held above a conducting ground plane in Figure 1.3a. From electromagnetic image theory, we may replace the ground plane with an oppositely charged wire (within the ground plane) forming a common two-wire transmission line, which propagates a transverse electromagnetic (TEM) mode at the speed of light with zero dispersion. As long as the

electric field lines from the wire terminate entirely on the ground plane and the distance between the ground and wire is kept constant, any gradual bends in the wire should only have a minor effect on the propagation characteristics of the line. The TEM mode propagates at the speed of light, c, *along the wire,* and the field intensity will be highly concentrated in the immediate vicinity of the wire. We may next wrap the line into a helix, maintaining a constant ground-wire separation through the use of a conducting cylinder, as in Figure 1.3b. The condition of a "gradual" bend in the wire is met by keeping the ground-wire separation distance much smaller than the pitch of the helix. Since an electromagnetic wave launched on this structure will follow the wire at the speed of light, the component of velocity along the center axis of the helix must be slower than c and can be approximately calculated from geometric projection as,

$$v_p = c\frac{p}{\sqrt{p^2 + (\pi d)^2}} \tag{1.7}$$

where p and d are respectively the pitch and diameter of the helix shown in Figure 1.3b. Since v_p is independent of frequency in this approximation, it is highly non-dispersive and the synchronism condition $v_0 \approx v_p$ may be maintained over a wide frequency band. This permits the unmatched broadband amplification capabilities of helix TWTs, which span multiple octaves [1], [3]. Thus, denoting β as the propagation constant along the axis, we write the vacuum circuit mode dispersion relation as

$$\beta = \omega/v_p \tag{1.8}$$

Pierce [12] quantified the power gain in a TWT in terms of the synchronous interaction between the beam mode [Eq. (1.6)] and the circuit mode [Eq. (1.8)], which we shall describe shortly, in both physical and mathematical terms.

Helix TWTs have relatively poor power handling capabilities, with peak power usually limited to a few kilowatts. One reason for this is the thin, delicate structure of the helix, which must be adequately cooled. Another reason is that beam interception can easily destroy the delicate helix. Alternative slow wave structures such as ring-bar [34], [35] or coupled cavity [36] allow for higher powers, but these suffer from stronger dispersion and therefore have smaller bandwidths. In the latter cases, the vacuum circuit mode is still described by Eq. (1.8), in which the circuit phase velocity v_p, will become a function of frequency, ω.

Excessively high beam currents (required for high power operation) may induce instabilities in the device, such as regenerative oscillations and backward wave oscillations (BWO) [3]. We will discuss BWOs and their impact on realistic TWTs in Chapter 3. Common strategies to suppress BWO include introducing lossy attenuators into the structure or severing the circuit [3], [13]; the impact of these design choices on TWT performance is addressed in Chapter 2.

1.1.3 The beam-circuit interaction

Thus far, we have briefly described the electron beam and the circuit wave separately. Next, we qualitatively describe the interaction between the two that allows amplification of an injected signal. Consider an electron beam propagating alongside a weak input signal near the start of the tube, in the reference frame of the traveling wave, as shown in Figure 1.4a. The DC velocity of the beam is chosen to be slightly greater than that of the wave, so the electrons will slowly drift to the right in this reference frame. (This is known as the "slow wave" in the plasma and beam physics literature [3], [13], [33], as the wave moves at a velocity slower than the beam. This wave carries a "negative wave energy density", meaning that its excitation requires removal of kinetic energy from the DC beam [33]). The short vertical lines with letter labels represent

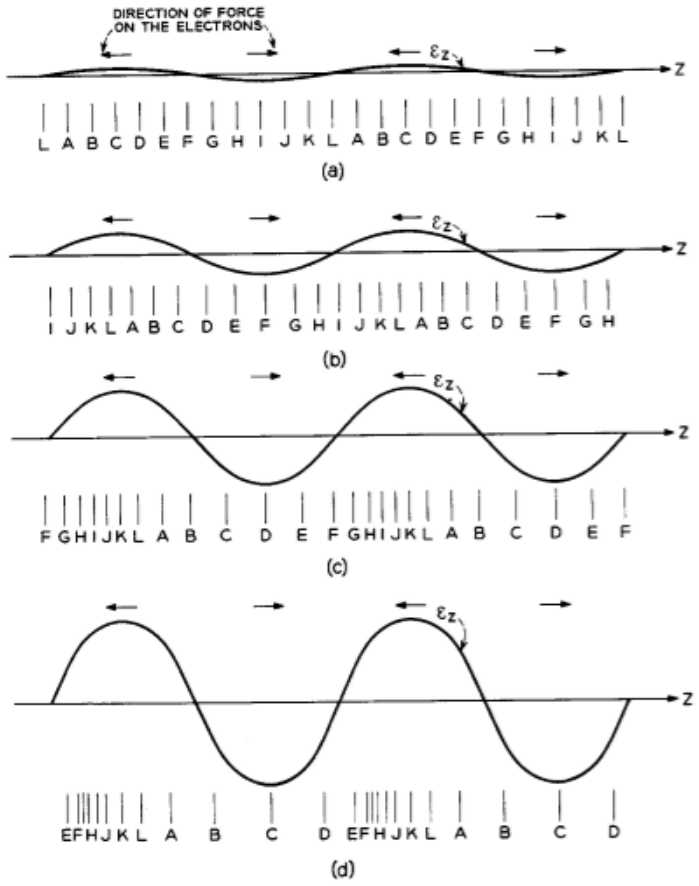

Figure 1.4: Electrons interacting with a traveling wave. The short vertical lines represent cross-sectional electron disks and the black sinusoid represents the electric field E_z (a) The picture near the input of the tube. Increased bunching and wave growth is observed at successive positions down the tube, illustrated by (b), (c), and (d). Image from [13].

cross-sectional disks of the electron beam; their uniform spacing in Figure 1.4a indicates that the density of the beam is initially uniform. The axial component of electric field of the input signal causes disks A-F to be decelerated while disks G-K are accelerated, tending to form a bunch centered on disk L, near the nodes of the wave. However, due to the DC beam velocity being slightly greater than the traveling wave's velocity, disk L has drifted into a decelerating electric field as shown in Figure 1.4b. Since there are more electrons in retarding field regions than in accelerating field regions, the net effect is a transfer of energy from the beam to the wave, causing the axial electric field to grow. This process continues in Figure 1.4c, with increased bunching accompanying increased wave amplitude growth. Since the beam is overall drifting to

the right in this reference frame, more and more electrons enter the retarding field regions, continuing the wave amplification process. Finally, in Figure 1.4d, near the output of the tube, the bunch is very tight, with very few electrons left in accelerating field regions. A significant amount of the beam's kinetic energy has been transferred to the wave, and the wave amplitude can be much higher than at the input. This amplified wave may then be extracted while the spent electron beam enters the collector region (See Figure 1.1) where its energy is harvested to improve the overall device efficiency through a depressed collector [3]. As an aside, note that if the beam velocity was chosen so that it was exactly equal to the wave phase velocity, no net energy transfer would occur. This suggests that the amplification mechanism saturates when the electron beam is slowed down to a velocity equal to the phase velocity of the wave [2], [3]. If the beam velocity was less then the phase velocity, energy would then be transferred from the wave to the beam; this situation describes a particle accelerator [2].

This amplification process may be described mathematically by quantifying the beam density perturbations due to the wave and the fields excited by these perturbations in beam current using a linear theory, also termed small signal analysis; this shows exponential growth of the RF signal with distance along the tube. The space charge effects of the beam, which cause electron bunches to spread apart due to repulsive forces, may be included. This linear small-signal analysis was first performed by Pierce [11], [12], and will be described in the next section. However, it fails to include several important effects, such as the overall slowing down of the beam due to the loss of its kinetic energy to the wave until saturation of the amplification mechanism occurs, i.e. when the amplified wave traps the electrons [2], [17]–[19], [22]. Other phenomena, such as electrons overtaking one another [37], harmonics of the drive signal [38], and the reversal of electrons must be analyzed using non-linear theory [2] and are beyond the

scope of this thesis. Linear theory is known to accurately describe ~85% of the tube length [2], [3] and essentially feeds into the non-linear theory. In the next section, we will derive the standard linear theory first developed by Pierce [11], [12], which describes the amplification of an input signal of frequency ω through the complex wavenumber β that is a solution of what is known as the Pierce dispersion relation $\beta(\omega)$. This dispersion relation describes the coupling between the beam and circuit modes and has also been used in the validation of non-linear, large signal numerical codes in the small-signal regime.

1.2 The Pierce theory of traveling-wave tubes

To treat the problem of mutual interaction between the electron beam and the circuit wave, we must initially treat each component separately. First, we will calculate the motion of the electron beam in response to an arbitrary RF electric field (the electronic equation). Next we will calculate the electric field excited on the circuit by some arbitrarily bunched beam, i.e., by some AC current in the beam (the circuit equation). Finally, we will combine these two expressions to yield a dispersion relation that will describe the behavior of the system for some input frequency ω. We will follow Pierce's [11], [12] approach, which is also detailed in most textbooks on vacuum electronics [2], [13]. This treatment has since found use in the description of various other radiation sources, including free electron lasers [14]–[19], gyro-TWTs [2], [21], [22], [24], Smith-Purcell radiators [15], [20] and metamaterial TWTs [39], [40].

1.2.1 The electronic equation

The electron beam may be treated using the cold fluid model, i.e. assuming zero temperature. The force law describing the velocity response $\vec{v}$ of an electron fluid element to an arbitrary electromagnetic field is given by

$$\frac{D\vec{v}}{Dt} = -\frac{e}{m_e}(\vec{E} + \vec{v} \times \vec{B}) \tag{1.9}$$

where $\frac{D}{Dt} = (\frac{\partial}{\partial t} + \vec{v} \cdot \nabla)$ is the convective derivative operator using the Eulerian formulation and $\vec{E}$ and $\vec{B}$ are respectively the electric and magnetic fields. An infinite focusing magnetic field is assumed in the z direction along the axis of the tube; this allows us to significantly simplify our analysis by limiting all electron motion to 1D, hence $\vec{v} = v\hat{z}$, reducing Eq. (1.9) to

$$\left(\frac{\partial}{\partial t} + v\frac{\partial}{\partial z}\right)v = -\frac{e}{m_e}E \tag{1.10}$$

where E is the total electric field, including both the circuit electric field as well as the space-charge fields due to the beam. We may also describe v in terms of the displacement s of an electron fluid element as

$$v = \left(\frac{\partial}{\partial t} + v\frac{\partial}{\partial z}\right)s \tag{1.11}$$

Under the small signal assumption, we may assume that all relevant parameters may be separated into an unperturbed DC component and a perturbative component with wavelike dependence, as follows.

$$s = s_0 + \tilde{s}_1 e^{j(\omega t - \beta z)} \tag{1.12a}$$

$$v = v_0 + \tilde{v}_1 e^{j(\omega t - \beta z)} \tag{1.12b}$$

$$E = E_0 + \tilde{E}_1 e^{j(\omega t - \beta z)} \tag{1.12c}$$

where the DC component has subscript "0", while the perturbative component has subscript "1", indicating first order, and a tilde, indicating that it is a complex amplitude. If no perturbations are induced, the zeroth order approximation holds, i.e. $s_0 = v_0 t$, $E_0 = 0$, and v_0 is given by Eq. (1.2). Pierce's small signal theory uses a first-order perturbation analysis, so any higher order terms, such as the product of two parameters with subscript "1", are considered very small

compared to the first order terms and are thus neglected. The power of this approach is that it allows us to reduce complicated differential equations to a set of algebraic equations, which may be more readily solved. Partial differential operators with respect to time or space on all perturbation quantities may then be replaced by the following multiplicative terms

$$\frac{\partial}{\partial t} \rightarrow j\omega \tag{1.13a}$$

$$\frac{\partial}{\partial z} \rightarrow -j\beta \tag{1.13b}$$

allowing us to write the linearized force law

$$j(\omega - \beta v_0)\tilde{v}_1 = -\frac{e}{m_e}\tilde{E}_1 \tag{1.14}$$

where

$$\tilde{v}_1 = j(\omega - \beta v_0)\tilde{s}_1 \tag{1.15}$$

Next, we separate the total electric field $\tilde{E}_1$ into the circuit field component $\tilde{E}_C$ and the electric field due to space charge $\tilde{E}_{SC}$

$$\tilde{E}_1 = \tilde{E}_C + \tilde{E}_{SC} \tag{1.16}$$

This decomposition of $\tilde{E}_1$ into $\tilde{E}_c$ and $\tilde{E}_{SC}$ requires care and is not straightforward because the space charge field can always be represented in terms of the vacuum circuit mode, very much like a discontinuous function may be represented by a Fourier sine or cosine series, each term of which is infinitely differentiable [41]. Following the customary treatments, we may combine Eqs. (1.14), (1.15) and (1.16) to give

$$(\omega - \beta v_0)^2 \tilde{s}_1 = \frac{e}{m_e}(\tilde{E}_C + \tilde{E}_{SC}) \tag{1.17}$$

An expression for $\tilde{E}_C$ will be derived in the next section. The space charge component $\tilde{E}_{SC}$ may be treated by means of Gauss's Law $\nabla \cdot \vec{E} = \rho/\epsilon_0$, which reduces to

$$\frac{\partial \tilde{E}_{SC}}{\partial z} = -j\beta \tilde{E}_{SC} = -\frac{e\tilde{n}_1}{\epsilon_0} \tag{1.18}$$

where we have substituted $\rho = -e\tilde{n}_1$, noting that n_0 does not contribute to the electric field along z. Using the continuity equation

$$\frac{\partial n}{\partial t} + \nabla \cdot n\vec{v} = 0 \tag{1.19}$$

which, after linearization reduces to

$$j(\omega - \beta v_0)\tilde{n}_1 = j\beta n_0 \tilde{v}_1 \tag{1.20}$$

we may substitute $\tilde{n}_1$ into Eq. (1.18), yielding

$$\tilde{E}_{SC} = \frac{e n_0 \tilde{v}_1}{j\epsilon_0(\omega - \beta v_0)} \tag{1.21}$$

Next, by substituting Eq. (1.15) and making use of the plasma frequency $\omega_p = \sqrt{\frac{e^2 n_0}{m_e \epsilon_0}}$, we may construct the following expression

$$\frac{e}{m}\tilde{E}_{SC} = \omega_p^2 \tilde{s}_1 \tag{1.22}$$

However, this treatment of space charge is overly simplistic. To account for the finite beam size as well as its interaction with higher order modes [2], [13] (the fundamental synchronous mode is accounted for when calculating $\tilde{E}_C$, as shown in the next section) we must replace ω_p^2 with the reduced plasma frequency $\omega_q^2 = R^2\omega_p^2$, where R^2 is the plasma frequency reduction factor. This reduction factor is dependent on the geometry of the tube as well as the frequency ω. In Pierce's original work [11], [12] and most TWT literature [2], [3], [13], these effects are designated by the dimensionless so-called Pierce space-charge parameter QC, defined such that [12]

$$QC = \frac{\omega_q^2}{4C^2\omega^2} \tag{1.23}$$

where C is the dimensionless Pierce gain parameter, defined as [12], [13]

$$C^3 = \frac{KI_0}{4V_b} \tag{1.24}$$

where I_0 is the DC beam current, V_b is the beam voltage, and K is the interaction impedance, which will be defined in the next section when we consider the circuit wave. Before continuing with our treatment of the electronic equation, we note that QC is notoriously difficult to calculate and properly account for [41], although several approximate models exist [42]–[46]. We will later describe a recent *exact* calculation of QC for a realistic TWT model [47], [48] and show how to include the effects of losses in a TWT into this calculation in Chapter 2.

Incorporating QC into Eq. (1.22) yields

$$\frac{e}{m}\tilde{E}_{SC} = R^2\omega_p^2\tilde{s}_1 \tag{1.25a}$$

$$= \omega^2(4QC^3)\tilde{s}_1 \tag{1.25b}$$

where we have used Eq. (1.23). We note that in the absence of the circuit electric field $\tilde{E}_C = 0$, combining Eq. (1.17) and Eq. (1.25b) allows us to express the beam mode including AC space-charge effects in Pierce's notation:

$$(\omega - \beta v_0)^2 - \omega^2 4QC^3 = 0 \tag{1.26}$$

Substituting Eq. (1.25b) into Eq. (1.17) while retaining $\tilde{E}_C$ gives the electronic equation, in Pierce notation:

$$[(\omega - \beta v_0)^2 - \omega^2(4QC^3)]\tilde{s}_1 = \frac{e}{m_e}\tilde{E}_C \tag{1.27}$$

Before we continue on to the treatment of the circuit wave, we note that the AC beam current $\tilde{I}_1$ may be expressed as:

$$\tilde{I}_1 = \tilde{J}_1 S = -e(n_0 \tilde{v}_1 + \tilde{n}_1 v_0) S \tag{1.28a}$$

$$\tilde{I}_1 = -jen_0 S\omega \tilde{s}_1 \tag{1.28b}$$

where S is the beam cross-sectional area and Eqs. (1.15) and (1.20) have been used.

1.2.2 The circuit equation

Here, we calculate how perturbations in the beam current induce currents on the circuit structure, leading to an amplification of the circuit wave. To relate the power on the circuit to the amplitude of the electric field, we may define the beam interaction impedance K, which characterizes the degree of coupling between the beam and the wave, as [12], [13]

$$K = \frac{\int |E_z|^2 dS}{2\beta_p^2 PS} \tag{1.29}$$

where $\beta_p = \frac{\omega}{v_p}$ is the cold circuit propagation constant, P is the power flow on the slow wave circuit and S is the cross-section of the slow wave structure. We will later find that high interaction impedance is associated with high gain per unit length in the TWT. K is dependent only on the geometry and frequency ω. We note that here, both K and β_p relate only to the fundamental space harmonic that is synchronous with the beam.

From Eq. (1.29) we may write the differential power on the slow wave structure from an infinitesimal segment dz of the beam as

$$dP = \frac{2E_z dE_z}{\beta_p^2 K} \tag{1.30}$$

This differential power is also equal to $dP = -\tilde{I}_1 E_z dz$, following transmission line theory. Using this with Eq. (1.30), we may calculate the differential electric field

$$dE_z = -\frac{\beta_p^2 K \tilde{I}_1}{2} dz \tag{1.31}$$

induced on the circuit by a beam segment dz. Eq. (1.31) illustrates how the interaction impedance K couples the beam current modulation $\tilde{I}_1$ to the circuit electric field. Two waves are launched at location z: a forward wave dE_{z+} and a backward wave dE_{z-}; by symmetry $dE_{z+} = dE_{z-}$

The total electric field is then given by

$$E_z(z,t) = \left(E_{inp} e^{-j\Gamma_0 z} + \int_0^z dE_{z+} e^{-j\Gamma_0 (z-z')} + \int_z^L dE_{z-} e^{-j\Gamma_0 (z'-z)} \right) e^{j\omega t} \tag{1.32a}$$

$$= \left[E_{inp} e^{-j\Gamma_0 z} - \frac{\beta_p^2 K}{2} \left(\int_0^z \tilde{I}_1(z')\, e^{-j\Gamma_0 (z-z')} dz' + \int_z^L \tilde{I}_1(z')\, e^{-j\Gamma_0 (z'-z)} dz' \right) \right] e^{j\omega t} \tag{1.32b}$$

Eq. (1.32a) makes use of a generalized complex propagation constant $\Gamma_0 = \beta_p - j\mathrm{Im}(\Gamma_0)$ where the imaginary part accounts for attenuation in the circuit. Here, we are summing up the contribution from (1) the input signal E_{inp} injected into the circuit at $z = 0$ (first term) (2) the electric field from beam segments before z (second term), and (3) the electric field from beam segments after z (last term). By differentiating Eq. (1.32b) twice with respect to z and using Eq. (1.32b) to eliminate E_{inp}, we can construct the differential equation

$$\frac{d^2 E(z)}{dz^2} + \Gamma_0^2 E_z(z) = j\Gamma_0 \beta_p^2 K \tilde{I}_1(z) \tag{1.33}$$

where E_z and $\tilde{I}_1$ have an implicit $e^{j\omega t}$ dependence. We may then set $E_z = E_C = \tilde{E}_C e^{j(\omega t - \beta z)}$ and reduce Eq. (1.33) to

$$\tilde{E}_C = \frac{j\Gamma_0 \beta_p^2 K}{\Gamma_0^2 - \beta^2} \tilde{I}_1 \tag{1.34}$$

This is the circuit equation, which gives the circuit electric field $\tilde{E}_C$ excited by the modulated beam current $\tilde{I}_1$ at frequency ω. Before we combine this expression with the electronic equation

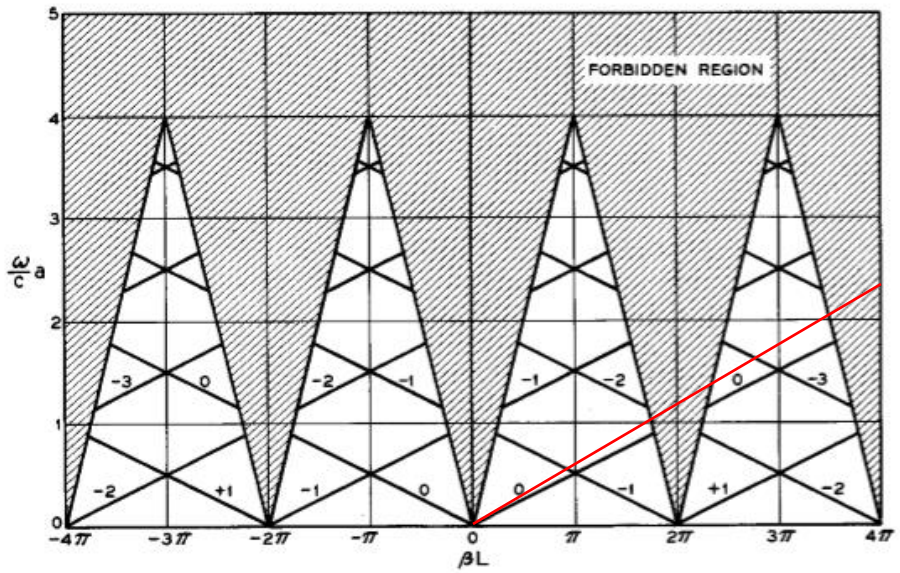

Figure 1.5: Dispersion diagram for an idealized tape helix showing circuit modes ($\beta = \beta_n$) labeled by their order n. The beam mode $\beta = \omega/v_0$ is also included in red. Here, a is the helix radius and $L=p$ is the helix pitch (See Figure 1.3). Image from [13].

to yield solutions for cumulative interaction, we will comment on the existence of higher order modes and space harmonics in a slow wave structure [13].

Figure 1.5 gives the Brillouin or dispersion (ω vs β) diagram for an approximate model of a tape helix [13]. The modes in the range of βL between $(0,2\pi)$ are called the fundamental branch, and those outside this range are called space harmonics. Note that all the space harmonic modes that can be supported on the SWS, neglecting lossy effects $(\mathrm{Im}(\Gamma_n) = 0)$ have the propagation constant of the nth spatial harmonic given by

$$\beta_n = \beta_0 + \frac{2\pi n}{p}, n = 0, \pm 1, \pm 2, \ldots, \tag{1.35}$$

where β_0 is the fundamental mode and p is the pitch of the helix [2], [12], [13].

Note that the dispersion diagram Figure 1.5 shows both the forward wave (straight lines with a positive slope) and backward wave (straight lines with a negative slope), representing, respectively, circuit waves that transport power in the forward and backward directions on the helix. The forbidden regions in Figure 1.5 are regions in which energy is radiated away; here, the

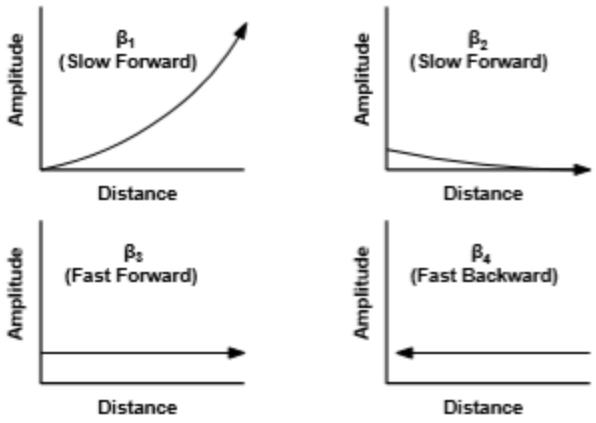

Figure 1.6: The Pierce 4-wave dispersion relation admits 4 roots. This figure illustrates the behavior of each wave. Image from [3].

helix acts as an antenna [13]. As we noted above, Pierce's theory uses only the interaction between the fundamental mode $n = 0$ and the beam mode, marked in red on Figure 1.5. TWTs may achieve appreciable gain when the beam mode is in the vicinity of the circuit mode, i.e., where the synchronism condition $v_0 \approx v_p$ is satisfied. Indeed, from Figure 1.5 we can see that this synchronism condition between the beam mode and $n = 0$ mode is satisfied for a wide range of frequencies; this gives the helix TWT its characteristically wide bandwidth. In Pierce's theory, the interaction between the beam mode and higher order circuit modes is characterized by QC, although until recently [47], [48], no exact determination of this parameter could be made, except for a hypothetical dielectric TWT [49].

Note that the beam mode (the red line in Figure 1.5) intersects the backward wave mode at $\beta L \approx \pi$. Thus, strong interaction between the beam and the backward wave mode is expected for (ω, β) near that intersection point. Indeed, this strong interaction is known to give rise to backward wave oscillation (BWO), which has long been recognized to pose a serious threat to the stability of the TWT [50]. We shall devote Chapter 3 of this thesis to the analysis of BWO.

1.2.3 The Pierce dispersion relation

Now that we have separately solved for the electronic and circuit wave equation, we may combine the two to yield a solution for cumulative interaction. We substitute Eq. (1.28b) into Eq. (1.34) to give

$$\tilde{E}_C = \frac{j\Gamma_0\beta_p^2 K}{\Gamma_0^2 - \beta^2}(-jen_0 S\omega\tilde{s}_1) \tag{1.36}$$

We may then multiply Eq. (1.36) by the electronic equation Eq. (1.27) and cancel the $\tilde{s}_1\tilde{E}_C$ factors to give the Pierce 4-wave dispersion relation:

$$[(\beta - \beta_e)^2 - \beta_e^2 4QC^3](\beta^2 - \Gamma_0^2) = -2\beta_e\beta_p^2\Gamma_0 C^3 \tag{1.37}$$

The first square bracket represents the beam mode, the second parenthesis represents the cold-tube circuit mode, and the RHS represents the coupling between the two. Note that in Pierce's theory, the circuit mode which is represented by the second parenthesis in Eq. (1.37), is unaffected by the beam current, in sharp contrast to the beam mode that is represented by the square bracket in Eq. (1.37); this deficiency in Pierce's theory was corrected only recently by Wong et al. [47], [48].

The relation (Eq. 1.37) admits four complex roots for β, corresponding to four waves that must be superimposed to fully describe the TWT behavior. As illustrated in Figure 1.6, three of the roots propagate in the forward direction; two of which result in spatial amplification and decay at the same rate, and the third is a neutral circuit wave. The fourth root is in the backwards direction and may give rise to backward wave interaction and oscillation (see Chapter 3). However, to describe the forward wave gain in a TWT, we may neglect this backward propagating wave by assuming $\beta \approx \Gamma_0 = \beta_p$, approximating the circuit mode term in Eq. (1.37) as $\left(\beta^2 - \beta_p^2\right) \approx 2\beta_p\left(\beta - \beta_p - jCd\beta_e\right)$. Here we have included the effect of losses in the circuit

[previously represented by $\mathrm{Im}(\Gamma_0)$] using the Pierce cold-tube loss parameter d, defined in Eq. (1.40d), below . This approximation yields the standard Pierce 3-wave dispersion relation [12]

$$[(\beta-\beta_e)^2-\beta_e^2 4QC^3]\left(\beta-\beta_p+jCd\beta_e\right)=-\beta_e\beta_p^2C^3 \tag{1.38}$$

This dispersion relation may also be expressed in dimensionless form through the use of the normalized propagation constant δ, as proposed by Pierce also [12],

$$(\delta^2+4QC)(\delta+jb+d)=-j \tag{1.39}$$

where

$$\delta=\frac{\beta-\beta_e}{j\beta_eC} \tag{1.40a}$$

$$b=\frac{v_0-v_p}{Cv_p} \tag{1.40b}$$

$$C^3=\frac{KI_0}{4V_b} \tag{1.40c}$$

$$d=\frac{\mathrm{Im}(\Gamma_0)}{\beta_eC} \tag{1.40d}$$

The three solutions to Eq. (1.39) depend only on the four dimensionless Pierce parameters, b, $C, d,$ and QC, which respectively, represent the degree of synchronism between the beam and wave (known as the detune parameter b), the degree of coupling in the beam-circuit interaction (known as the Pierce gain parameter C), the attenuation in the cold circuit wave (known as the cold-tube loss parameter d), and the effect of space charge including its interaction with higher order circuit modes (known as the Pierce space charge parameter QC). The gain in TWT may be expressed in dB at a distance L from the input as [2], [13]

$$G=20\log\left|\sum_{k=1}^{3}\frac{\delta_k^2+4QC}{(\delta_k-\delta_l)(\delta_k-\delta_m)}e^{\delta_k\beta_eCL}\right|\ \mathrm{dB} \tag{1.41}$$

where $\delta_{k,l,m}$ are the three roots to Eq. (1.39). Equation (1.41) was derived assuming that at the input location of the TWT, the electron beam has zero initial displacement, zero initial velocity, and the input circuit wave has a unit amplitude (for the linear theory). These three conditions give the amplitude of the three waves whose propagation constant is solved from Eq. (1.39).

1.3 Crossed-field devices

The work in this thesis almost exclusively concerns traveling-wave tubes, so most of the introduction has been devoted to the theory of their operation. However, in Chapter 4, concerning the transition from temperature-limited to space-charge-limited emission regimes for thermionic cathodes, we include some simulation results where, in addition to an electric field being applied across an anode-cathode gap, we apply a magnetic field orthogonal to the electric field, parallel to the cathode. This is known as the crossed-field geometry, and devices utilizing a crossed electric and magnetic field are known as crossed-field devices [1], [3]. The best known crossed-field device is the ubiquitous magnetron (See Figure 1.7), used in domestic microwave ovens around the world. Here, we will make some brief comments on crossed-field devices that are relevant to our work in Chapter 4.

Recall from basic single charged particle motion theory in plasma physics [51] that an electron in a crossed-field geometry will execute circular orbits as it drifts in the $\vec{E} \times \vec{B}$ direction with drift velocity $v_{E\times B} = E/B$. If this drift velocity is designed to maintain synchronism with an excited circuit wave that travels on the vanes of an anode slow wave structure (See Figure 1.7), the electron's potential energy is transferred to the circuit wave [52]. This results in the formation of electron spokes, analogous to the electron bunching effect in a TWT (cf. Figure 1.4). This synchronism condition is given by the Buneman-Hartree condition [1], [52]–[56].

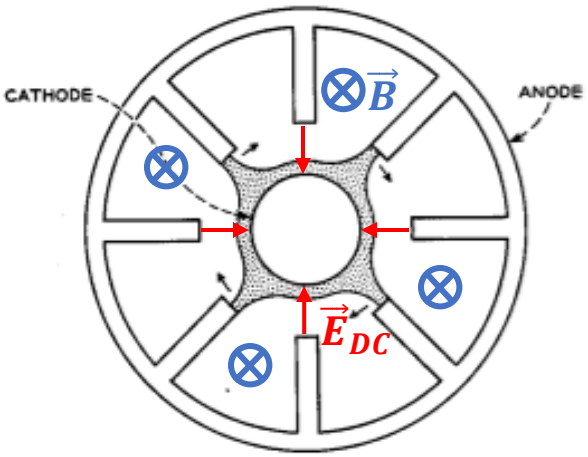

Figure 1.7: Schematic of an 8-cavity magnetron showing direction of DC electric and magnetic fields and formation of electron spokes. Image from [13].

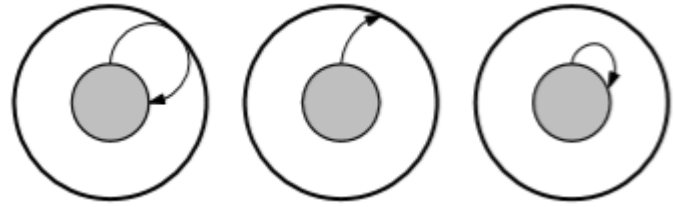

Figure 1.8: Electron trajectories for magnetic fields (a) at, (b) below, and (c) above Hull cutoff B_H. Image from [3].

An additional condition must be met for proper operation of the magnetron: A-K gap magnetic insulation, i.e. the applied magnetic field must be sufficiently strong to prevent electrons emitted at the cathode from reaching the anode. The critical magnetic field at which an emitted electron just barely misses the anode is the Hull cutoff magnetic field B_H (See Figure 1.8a) [3], [52]. If the applied magnetic field is small ($B < B_H$), the electron will reach the anode, shorting the gap (See Figure 1.8b). If the magnetic field exceeds the Hull cutoff ($B > B_H$), the electron is turned back to the cathode, magnetically insulating the gap (See Figure 1.8c). The range of operation for a magnetron in terms of the A-K voltage and applied magnetic field is thus bounded by these two conditions: the Hull cutoff and the Buneman-Hartree condition. [3], [53]–[55].

We remark that two models for electron flow in crossed field devices exist [52]: a cycloidal flow based on the single particle orbits and a shear flow (also called Brillouin flow [52]–[54]) where electron velocity is parallel to the cathode surface and increases from zero at the cathode surface up to the top of the electron hub. Although the Hull cutoff condition is independent of the electron flow model, the two orbits give different results for the Bunemann-Hartree condition for a cylindrical magnetron [55]. It is generally agreed that the Brillouin flow is the preferred state for crossed-field devices [57].

Other crossed field high power microwave sources include the crossed field amplifier (CFA) [1], [3], [56], [58], which amplifies an input RF signal passed along the slow wave structure similar to a TWT, and the magnetically insulated line oscillator (MILO) [59], where the insulating magnetic field is generated by the high anode current, without the use of any external magnetic field. Our work in Chapter 4 may also be relevant to power flow in linear transformer drivers (LTDs) and magnetically insulated transmission lines (MITLs) [60]. Finally, we remark that the theory of crossed-field devices is not well established compared with that of linear beam tubes such as TWTs and klystrons, one reason being that the electron orbits are not as readily characterized, especially when an RF electric field is present; another reason being that the RF energy is primarily converted from the potential energy of the electrons instead of the kinetic energy [52].

1.4 Prior work and thesis organization

Now that we have described the foundations of TWT theory, we may proceed to extend it to include various realistic effects. In Chapter 2, we will describe how the effect of idealized and realistic cold circuit loss profiles may be included in a novel exact hot-tube dispersion relation for a tape helix TWT. In Chapter 3, we will assess how random manufacturing errors and tube

end reflections may impact the onset of the backward wave oscillation that is known to disrupt TWT operation. In Chapter 4, we will focus our attention solely on the generation of the electron beam via thermionic cathode, examining the role of 2D work function variations on the cathode surface. We summarize the major results at the end of each chapter. Before proceeding, we will first briefly discuss the prior work on these topics.

1.4.1 Exact dispersion relation for a tape helix

In our derivation of the electronic equation and the Pierce dispersion relation, we have remarked that the space charge parameter Q is notoriously difficult to calculate for realistic TWTs [41]. Q is closely related to the plasma frequency reduction factor R^2, which, in principle, depends on the geometry of the structure and the beam's interaction with higher order circuit modes. The most widely used model in the TWT community is given by Branch & Mihran [42], who assume that the helix may be replaced with a perfectly conducting metallic cylinder. While more sophisticated models exist [44]–[46], they do not give a procedure for directly evaluating Q. This is an important matter, since small discrepancies in Q may lead to a large change in the predicted gain [See Eq. (1.39) and (1.41)] in linear theory as well as in non-linear codes such as CHRISTINE [61]. Furthermore, as we will show in Chapter 3, the threshold conditions for the BWO instability are dependent only on QC and d.

Recently, our group calculated [47], [48] an exact hot-tube dispersion relation for a thin, tape helix surrounded by a dielectric support region (See Figure 2.1). This work was built on an earlier paper by Chernin et al. [62], who determined all the cold circuit modes that could propagate on this electromagnetic structure when the electron beam was absent. Wong et al. [47] included the effect of a pencil beam to calculate a very complicated expression for the dispersion relation that yields three numeric roots $\beta_1, \beta_2, \beta_3$, corresponding to the solutions to the Pierce 3-

wave dispersion relation [Eq. (1.38)]. From this, Wong et al. not only was able to give an exact determination of Q by numerical means, but also found that the circuit mode in Pierce's dispersion relation, Eq. (1.38), must be modified by a new space charge parameter, which they called q. For realistic TWTs, this may detune the circuit phase velocity by as much as 2%, which is quite significant. However, Wong's formulation was not able to include the effects of cold circuit losses, characterized by the Pierce parameter d.

In Chapter 2, we will present a method for modeling the combined effect of $Q, d,$ and the new circuit mode space charge parameter q, for the realistic tape helix.

1.4.2 Threshold conditions for backward wave oscillations

The small dimensions of the slow wave structure of a helix TWT are prone to random variations in pitch and other deformation due manufacturing errors. Several studies [63]–[67] have demonstrated the impact of these random manufacturing errors on the performance of TWTs. These problems are only expected to compound as the operating frequencies are increased into the THz regime, due to the accompanying drop in the length scale of the slow wave structure. The effect of these errors may be simulated by introducing random variations in the Pierce parameters, particularly in the most sensitive detune parameter b [63], [65], [66], [68]. It is unclear how these errors may affect the onset of backward wave oscillation, which is a zero drive instability arising from the backward propagating mode that may significantly disrupt tube operation, as discussed toward the end of Section 1.2.2. The classical theory for the threshold of BWO is given by Johnson [50].

In Chapter 3, we describe Johnson's classical theory and extend it to model the effects of these random manufacturing errors, and, separately, the effects of reflections off the ends of the tube.

1.4.3 Thermionic cathodes

In Section 1.1.1, we described the temperature-limited and space-charge-limited operation of a thermionic cathode, characterized respectively by the Richardson-Dushman [26], [27] and Child-Langmuir [28], [29] laws. The transition between these two regimes is described by the Miram curve [69], a plot of anode current vs cathode temperature. While thermionic cathodes have been used for over a century, there exists a major unsolved mystery concerning the Miram curve [3]. This old problem is important, because communication satellites are critically dependent on the traveling wave tube amplifier on board, and the life of a TWT is largely determined by the life of its cathode. The Miram curve naturally shows the transition from temperature-limited emission (Richardson-Dushman Law) to space-charge limited emission (Child-Langmuir Law), as the cathode temperature is increased. This transition occurs at the "knee" on the Miram curve. Typically the knee is smooth and broad in experiments, a feature no physical theory has replicated in all these years. A sharp and abrupt knee is highly desirable, usually simulated but difficult to achieve in practice. This discrepancy has been an important, unresolved mystery, because thermionic cathodes almost always operate around this knee to obtain the maximum anode current at the lowest possible cathode temperature so as to preserve cathode life. The smoothness and roundedness of the knee has generally been attributed to variations on the cathode surface, particularly in the non-uniformity of the work function.

Recently, Chernin et al. [70], building on the thermal emission models of Fry and Langmuir [29], [31], incorporated work function variations along one spatial dimension of the cathode. This work demonstrated how these work function 'stripes' could serve to broaden the knee via a 2D space charge effect. Furthermore, when work function variations were included along *both* spatial dimensions of the cathode, particle-in-cell simulations using the electron gun

code MICHELLE [71] showed smooth and rounded Miram curves, similar to those obtained experimentally. When cathode work function variations are restricted to 1D, excellent agreement between Chernin's analytic theory and MICHELLE simulation was found; these comparisons were made using work function distributions extracted from recent experiments at the University of Wisconsin [72], [73]. It is therefore of considerable interest to extend Chernin et al.'s model [70] to incorporate 2D work function patterns. Such an analytic study would provide substantial saving of computer time for parametric studies. The computational time required to solve the anode current at a single temperature is on the order of hours for a MICHELLE simulation, compared to several minutes using the analytic formulation to be presented in this thesis [74].

In Chapter 4, we describe the major results of [70] and present results from the extended model [74], studying a variety of idealized and realistic 2D work function patterns and evaluating their effect on the shape of the Miram curve. Furthermore, we present particle-in-cell simulations used to validate an analytical thermal emission model for crossed-field flow [75].

Chapter 2 Inclusion of Cold Tube Loss in an Exact Dispersion Relation for Traveling Wave Tubes

2.1 Introduction

In a traveling wave tube, the amplification mechanism is due to the continuous transfer of the electron beam's kinetic energy through a synchronous interaction between the electron beam with the forward propagating wave of the surrounding electromagnetic structure. This interaction is described by the Pierce's dispersion relation, Eq. (1.38), which is a third degree polynomial for the propagation constant, β, whose imaginary part gives the spatial amplification rate of the input signal of frequency ω The underlying physics for this three-wave theory, which led to this third degree polynomial, was described in Chapter 1.

In Chapter 1, we described how recent work by Wong et al. [47], [48] found that the classical Pierce three-wave TWT dispersion relation, Eq. (1.38) requires revision at high beam currents to include additional space charge effects on the circuit mode. These effects are included via a new space charge parameter, *q*, which modifies the circuit mode of the dispersion relation in an analogous manner to how Pierce's original space charge parameter *Q* modifies the beam mode. This modified Pierce three-wave dispersion relation reads [47],

$$[(\beta - \beta_e)^2 - 4\beta_e^2 Q C^3]\left[\beta - \beta_p - 4\beta_p q C^3\right] = -\beta_e^3 C^3 \tag{2.1}$$

where β is the propagation constant at frequency ω, $\beta_e = \omega/v_o$ is the propagation constant of the beam mode, $\beta_p = \omega/v_p$ is the propagation constant of the vacuum circuit mode which is assumed to be lossless ($d = 0$), v_0 is the beam velocity, v_p is the phase velocity of the forward circuit wave, and C is the gain parameter which determines the coupling between the beam mode

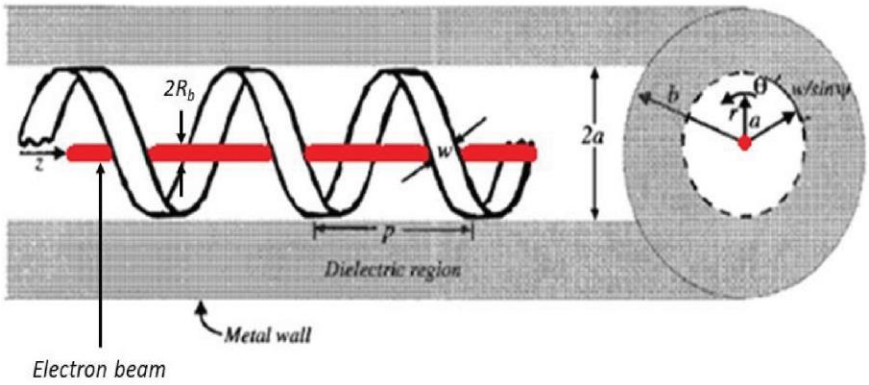

Figure 2.1: Schematic of tape helix TWT model with dielectric support layer.

[the first square bracket] and the circuit mode [the second square bracket], with C^3 being proportional to the DC current on the electron beam [See Eq. (1.40c)]. It is seen from Eq. (2.1) that the presence of q in effect introduces a potentially significant detune in the circuit phase velocity, by $4qC^3$, which amounts to approximately two percent in a realistic example of a tape helix TWT [47]. Setting $q = 0$ in Eq. (1) recovers Pierce's classical 3-wave dispersion relation Eq. (1.38) [12], [13].

The discovery of q arose from an electromagnetic analysis of a thin, perfectly conducting (i.e. lossless) tape helix surrounded by a supporting dielectric layer (Figure 2.1). This treatment, first performed by Chernin et al. [62] for a cold tube, i.e. in the absence of an electron beam, was then extended by Wong et al. [47], [48] to include the effect of a pencil electron beam. The resulting hot-tube dispersion relation is analytically exact, but due to its complexity must be solved numerically. For a given frequency ω in the range of interest, Wong showed that [47], [48] the dispersion relation always yields three roots for β, one of which is purely real (neutral wave) while the other two are complex conjugates of each other (spatially growing and damping waves). We may write the dispersion relation in the form

$$(\beta - \beta_1)(\beta - \beta_2)(\beta - \beta_3) = 0 \qquad (2.2)$$

where $\beta_{1,2,3}$ are the numerical roots to the exact dispersion relation. By comparing Eq. (2.2) to Eq. (1.38) in the lossless case of $d = 0$, it may be seen that is impossible for Eq. (1.38) to yield three roots of β that satisfy Eq. (2.2) *unless* there is an additional term modifying the circuit mode in the manner shown in Eq. (2.1). We may now solve for the parameters qC^3, QC^3, and C^3 in terms of the numerical roots β_1, β_2, and $\beta_3$by equating the coefficients of β^2, β^1, and β^0 in Eqs. (2.1) and (2.2), as follows [47], [48],

$$qC^3 = \frac{1}{4}\left(\frac{\beta_1 + \beta_2 + \beta_3 - 2\beta_e}{\beta_p} - 1\right) \tag{2.3a}$$

$$QC^3 = \frac{1}{4}\left(1 - \frac{\beta_1\beta_2 + \beta_2\beta_3 + \beta_1\beta_3 - 2\beta_e\beta_p(1 + 4qC^3)}{\beta_e^2}\right) \tag{2.3b}$$

$$C^3 = \frac{\beta_e^2(1 - 4QC^3)\beta_p(1 + 4qC^3) - \beta_1\beta_2\beta_3}{\beta_e^3} \tag{2.3c}$$

This process for accurately determining Q is important for several reasons. There is no general calculation of Q in the literature [41], [49], instead only approximate models are available [42]–[46]. The results of non-linear TWT simulation codes such as CHRISTINE [61] as well as predictions of small-signal gain may be sensitive to small discrepancies in Q [44], [47]. Additionally, the threshold conditions for backward wave oscillation in Johnson's classical theory depend only on QC and d, so predicting the onset of BWO requires accurate calculation of these parameters [47], [50], [76]. Note that the exact determination of C and Q yield different values from the classical theory of Pierce, who assumed only a dominant beam mode and a dominant circuit mode, whereas the exact theory [Eqs. (2.3a-2.3c)] has accounted for all circuit modes and beam modes, including their space harmonics, as explained in Chapter 1.

If the tape helix is lossy, as is the case for all real TWTs, solving the exact hot-tube dispersion relation gives three complex roots for β and leads to complex values for the

parameters $q, Q,$ and C, which are very difficult to physically interpret. In the rest of this chapter, we explore an intuitive, physical method of modeling the combined effect of q and cold tube loss d, including realistic examples of uniform and non-uniform loss profiles.

2.2 Formulation

We propose that to include the effects of cold tube loss, the dispersion relation must be further modified to [77]

$$[(\beta - \beta_e)^2 - 4\beta_e^2 Q C^3]\left[\beta - \beta_p - 4\beta_p q C^3 + jCd\beta_e\right] = -\beta_e^3 C^3 \qquad (2.4)$$

where $q, Q,$ and C are determined *exactly as if the circuit were lossless*, i.e. following Eq. (2.1) and (2.3), and d is Pierce's conventional cold tube loss parameter. The rationale for Eq. (2.4) follows. We want to be as close to Pierce's classical 3-wave TWT theory as possible [cf. Eq. (1.38)], both in the form of the dispersion relation and in its interpretation. First, the cold tube propagation constant reads $\beta = \beta_p - jCd\beta_e$, which is consistent with the classical Pierce results. The beam mode, which is represented by the first square bracket on the LHS of Eq. (2.4), remains unchanged from the exact theory of Wong. We further assume that the modifications to the lossless circuit mode, due to the space charge effect (modelled by *q*), and due to the circuit loss (modelled by *d*) are both small. Each of these two effects will enter linearly and independently in the circuit mode factor [second square bracket in Eq. (2.4)], and their mutual interaction becomes a higher order effect, which we ignore. Furthermore, we assume that the small correction due to the circuit loss would not change the coupling impedance that is represented by the RHS of Eq. (2.4), in which C has been calculated from the exact dispersion relation, so that this value of C is different from Pierce's theory (in which C was derived using only the dominant cold-tube circuit mode) but is identical with Wong's exact theory.

Eq. (2.4), as written, then has three attractive properties: (1) the parameters Q, q, and C are all real because they were derived assuming $d = 0$, (2) Eq. (2.4) reduces to Wong's formulation Eq. (2.1) when $d = 0$, and (c) Eq. (2.4) reduces to the form of Pierce's classical theory [Eq. (1.38)] for a lossy tube when $q = 0$.

While this dispersion relation [Eq. (2.4)] describes a spatially uniform tube with a constant value for d (and for all the other Pierce parameters), we may generalize it to include distributed loss along the tube axis z with $d = d(z)$ (or additionally, some z dependence for any or all of the other Pierce parameters). Note that this generalized description of $d(z)$ may include cold tube loss from many sources, including the helix itself, the support rods, or from some arbitrarily imposed loss profiles, by design, for example to resistively damp the unwanted modes.

To model distributed circuit loss in the exact theory, we begin with the linearized force law applied to a cold electron fluid element

$$\left[\left(\frac{\partial}{\partial z} + j\beta_e\right)^2 + 4\beta_e^2 Q C^3\right] s = a \tag{2.5}$$

where s is the displacement of this fluid element from its unperturbed position in response to the normalized AC electric field a on the circuit. Equation (2.5) may be compared with Eq. (1.27). This modulation in displacement is proportional to the current modulation which in turn excites the circuit field according to

$$\left[\frac{\partial}{\partial z} + j\beta_p(1 + 4qC^3) + \beta_e C d\right] a = -j\beta_e^3 C^3 s \tag{2.6}$$

where the usual expression for the circuit mode [63], [68] has been modified to include the detuning effect of q. The square bracket in Eq. (2.6) may be compared with the parenthesis in the LHS of Eq. (1.38). Additionally, we define a normalization variable f such that $s = e^{-jx} f(x)$

where $x = \beta_e z$ is the normalized axial distance. Combining Eqs. (2.5) and (2.6) yields the third-order ordinary differential equation

$$\frac{d^3 f(x)}{dx^3} + jC\left(b - jd + 4qC^2\frac{\beta_p}{\beta_e}\right)\frac{d^2 f(x)}{dx^2} + 4QC^3\frac{df(x)}{dx} + jC^3\left[4QC\left(b - jd + 4qC^2\frac{\beta_p}{\beta_e}\right) + 1\right]f(x) = 0 \tag{2.7}$$

which governs the evolution of the normalized circuit field

$$a(x) = f''(x) + 4QC^3 f(x) \tag{2.8}$$

subject to the initial conditions

$$f(0) = 0, \qquad f'(0) = 0, \qquad f''(0) = 1 \tag{2.9}$$

which represent, respectively, zero ac current, zero ac velocity, and unit output electric field [63], [65], [78]. Note that when d (and all the other Pierce parameters) are constant with respect to z, the solution to Eq. (2.7) is consistent with Eq. (2.4) for a uniform tube, whose gain (in dB) in the circuit wave power $|a^2|$ at a distance L from the input is given by Eq. (1.41) [4, Eq. (11.5-15)]

$$G = 20\log\left|\sum_{k=1}^{3}\frac{\delta_k^2 + 4QC}{(\delta_k - \delta_l)(\delta_k - \delta_m)}e^{\delta_k\beta_e CL}\right| \text{ dB} \tag{2.10}$$

where the three roots of β, $(\beta_k, \beta_l, \beta_m)$, to Eq. (2.4) are represented by δ, $(\delta_k, \delta_l, \delta_m)$, in Eq. (2.10) where $\delta_{k,l,m} = -j(\beta_{k,l,m} - \beta_e)/C\beta_e$. Note that $\delta_{k,l,m}$ are the three roots of δ when the solution to the third degree ordinary differential equation, Eq. (2.7) assuming constant coefficients, assumes the simple exponential form, $f(x) = e^{C\delta x}$, as in Pierce's notation [see Eq. (1.39) in Chapter 1].

2.3 Numerical Results

As a test case, we shall use a tape helix TWT model with the same beam and circuit parameters as Chernin et al [62] and Wong et al [47], summarized in

Table 2.1; however, we extend it to include a lossy dielectric support layer (Figure 2.1). While we assume that the dielectric layer has the same real part of the dielectric constant, $\epsilon_r = 1.25$, the imaginary part is specified via the loss tangent, $\tan(\delta) = \epsilon_i/\epsilon_r$, which we will vary in a number of test cases.

Table 2.1 Tape helix parameters for test case [See Fig. 2.1]

Parameter	Value
Tape radius a	0.1245 cm
Helix pitch p	0.080137 cm
Pitch angle ψ	5.85°
Tape width w	0.0159 cm
Real dielectric constant of supporting area ϵ_r	1.25
Beam voltage V_b	3 kV
Tape radius a	0.1245 cm

The lossless tube corresponds to $\epsilon_i = 0$, for which the cold tube circuit mode propagation constant is designated as β_{p0}, which is real, and is calculated exactly as in [62]. A nonzero ϵ_i introduces an imaginary part, and a shift in the real part of the cold tube propagation constant. The percentage change of these real and imaginary parts is shown in Figure 2.2 for a uniform tube with $\epsilon_i/\epsilon_r = 0.01, 0.05, 0.1, 0.2$. We need to retain the change in the real part because it yields a similar effect as q according to Eq. (2.4). However, a comparison of Figure 2.2(a) and (b) shows that the change in the real part is much smaller than the change in the imaginary part of the cold tube propagation constant. We also find that this change in the real part of β_p (from

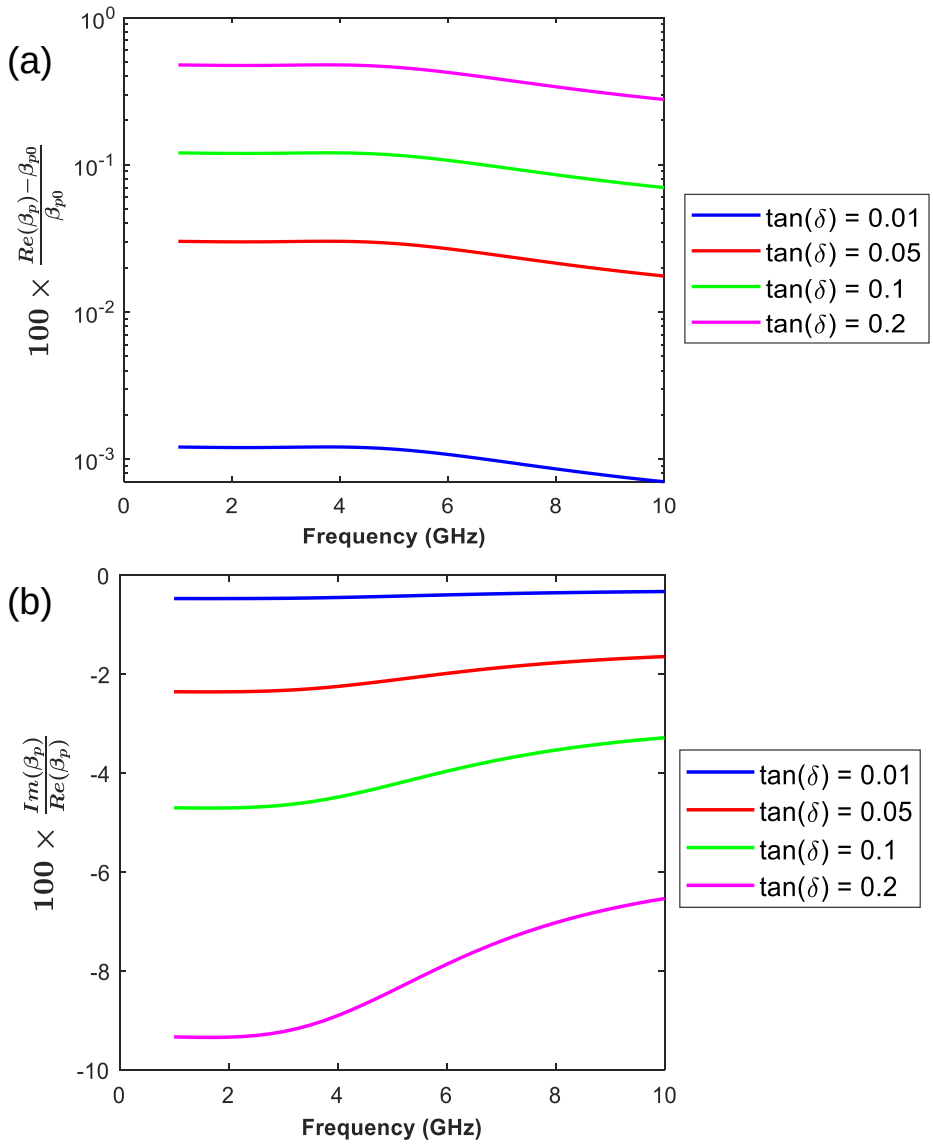

Figure 2.2: (a) Percent difference between the real part of lossy β_p and the lossless β_{p0} (b) Ratio (in percent) between the imaginary and real components of lossy β_p.

β_{p0}) is also much smaller than the detuning effect due to q for our numerical examples [cf. Eq. (2.4)]. The loss parameter, d, is [12], [13]

$$d = \mathrm{Im}(\beta_p)/\beta_e C = 0.01836\,\Lambda/C \tag{2.11}$$

where Λ is the cold-tube loss in dB per axial wavelength of the beam mode.

Next, we compare results from the "exact" theory with those of the "Pierce" theory. By "exact" theory, we mean that that Q, q, and C are obtained from the exact hot tube dispersion

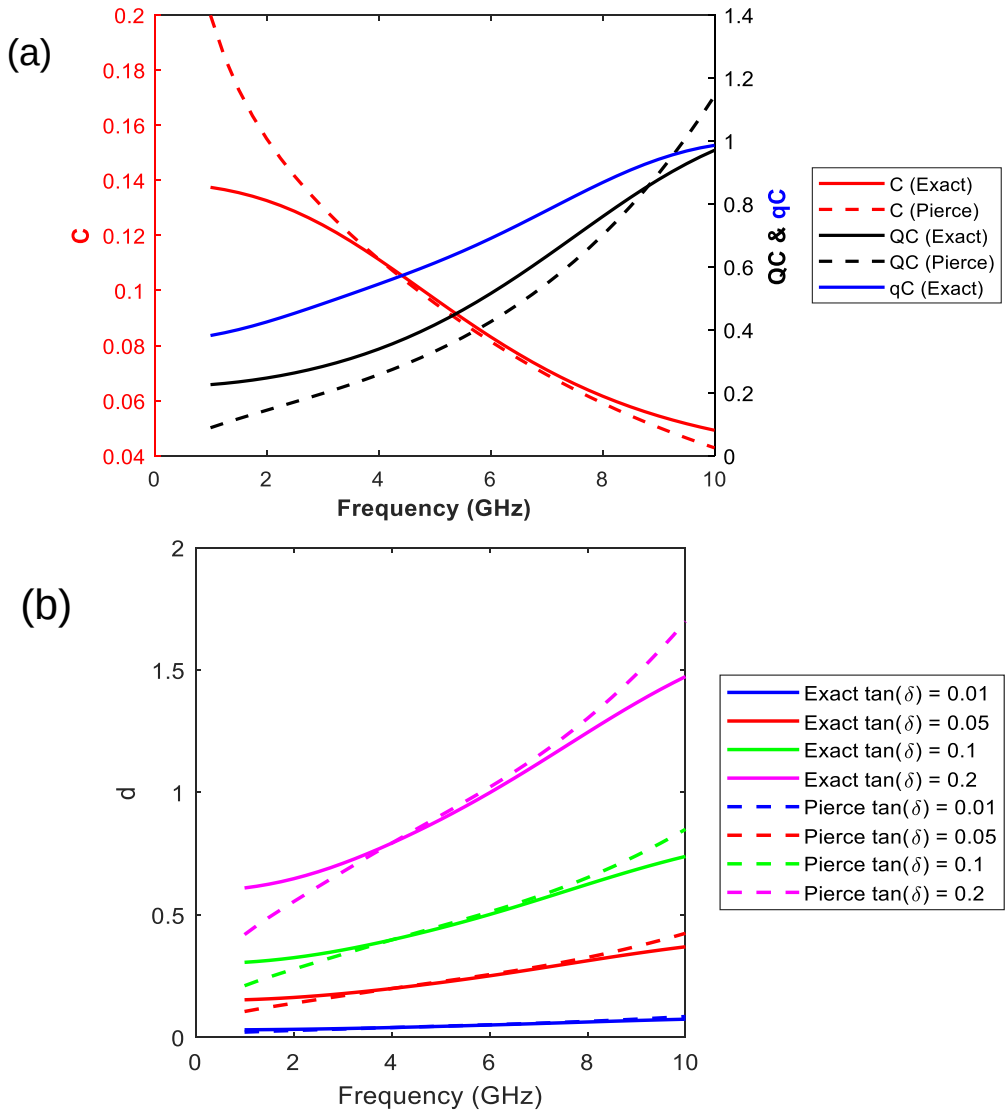

Figure 2.3: Plots of Pierce parameters (a) *C*, *QC*, and *qC* for *d* = *0*; (b) *d* from the exact solution and the classical Pierce approach.

relation, Eqs. (2.3a) – (2.3c), assuming a lossless tube [47], [48], and this value of C is used in Eq. (2.11) to obtain *d*. By "Pierce" theory, we mean $q = 0, QC$ is determined from the Branch-Mihran model [42], and $C^3 = K_0 I_b/(4V_b)$ where K_0 is given by [13, eqs. 10.3-22 and 10.2-21]

$$K_0 \cong \frac{15\ \Omega}{ka} \times \frac{1}{S I_0^2(\gamma_0 a)} \int I_0^2(\gamma_0 r) dS \tag{2.12}$$

where $k = \omega/c$, S is the beam cross-sectional area, $\gamma_0^2 = \beta_p^2 - k^2$, and $I_0(x)$ is the modified Bessel function of the first kind of zeroth order.

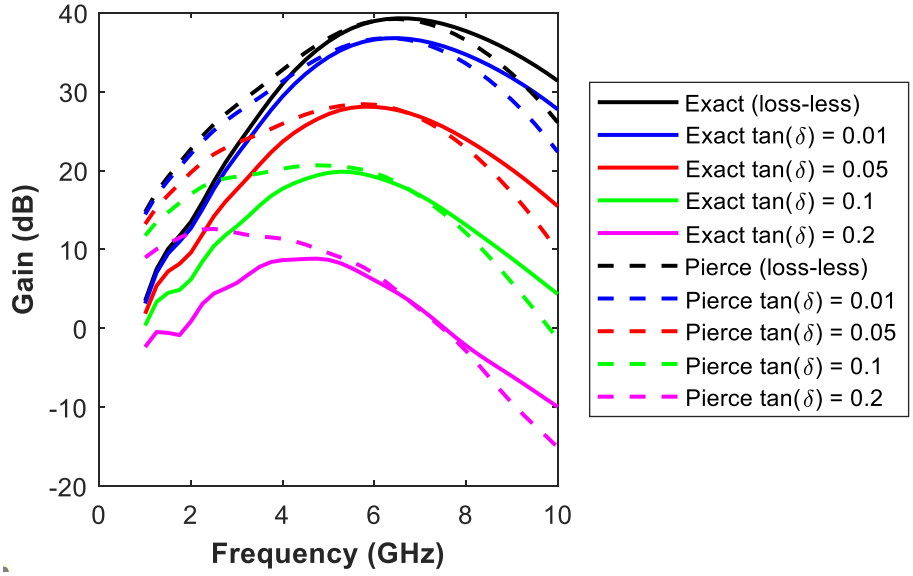

Figure 2.4: Gain for a TWT of interaction length L = 10 cm from exact and Pierce solutions.

This classical value of C is used in Eq. (2.11) for the "Pierce" theory. We emphasize that this classical value of C, which employs only the dominant cold-tube circuit mode, is different from the C obtained from the exact theory [47], as shown in Figure 2.3a. It is this exact value of C that is used in Eq. (2.4) which marks one of the departures from the classical Pierce's theory [the second departure is the value of Q, the third departure is the value of d because the value of d depends on the value of C, as shown in Eq. (2.11), and, finally, the fourth departure is the presence of q in Eq. (2.4).]. Figure 2.3(b) shows the differences between the value of d in the "exact" theory and "Pierce" theory.

The gain for a tube with interaction length $L = 10$ cm, calculated using Eq. (2.10), is plotted in Figure 2.4. The exact and Pierce theory agree well only in a restricted frequency range, and significant divergence is observed below 4 GHz and above 8 GHz. This is most likely attributed to the discrepancy in the same frequency range in C and in d (Figure 2.3), which in turn originates from the approximate formula for interaction impedance used in the Pierce theory (Eq. 2.12).

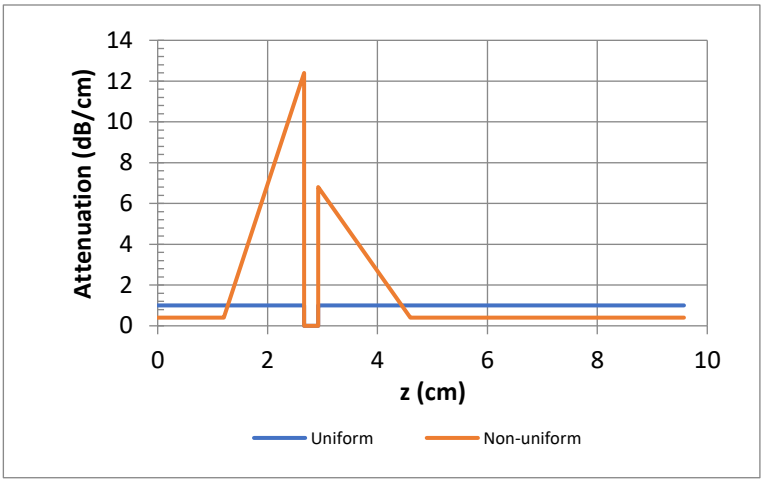

Figure 2.5: Attenuation profiles of TWT with sever between z_- = 2.667 cm and z_+ = 2.921 cm. From [38].

We next consider two realistic test cases of TWTs with severs [38]; one has uniform attenuation while the other has a variable attenuation profile (Figure 2.5). Fixing the frequency at 4.5 GHz, we find that the attenuation in the uniform case corresponded to a loss tangent of 0.03, where we made use of Equation (2.11). The attenuation profile, $d(z)$, for the non-uniform case in Figure 2.5 may then be scaled accordingly (excluding the sever region, $z_- < z < z_+$). Calculations of the power in the sever and non-sever regions must be performed with care [38]. The power in the pre & post-sever regions, where the beam and circuit effects are combined, is calculated from Eq. (2.8), after numerical integration of Eq. (2.7). The sever region $(z_- < z < z_+)$ is modelled by assuming the electric field is completely cut off and that all information is transferred to the post sever region by the beam alone. In mathematical terms, this amounts to solving the differential equation $a(x) = 0$, ensuring that $f(x)$ and $f'(x)$ are continuous at z_- and z_+ and that the initial condition of the field at z_+ is $f''(z_+) = -4QC^3 f(z_+)$. Figure 2.7 shows a comparison of the power along the length of the tube between the Pierce & exact cases using both the uniform & non-uniform attenuation profiles. For both the Exact & Pierce results, we observe higher gain in the uniform case immediately before and after the sever, illustrating the effects of increased

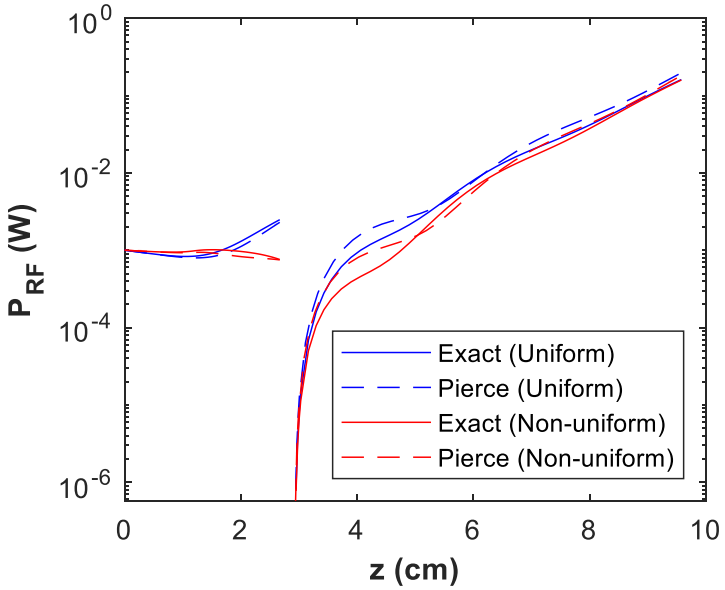

Figure 2.7: RF power profile for the Pierce and Exact cases using the uniform and non-uniform attenuation profiles at 4.5 GHz with input power of 1 mW.

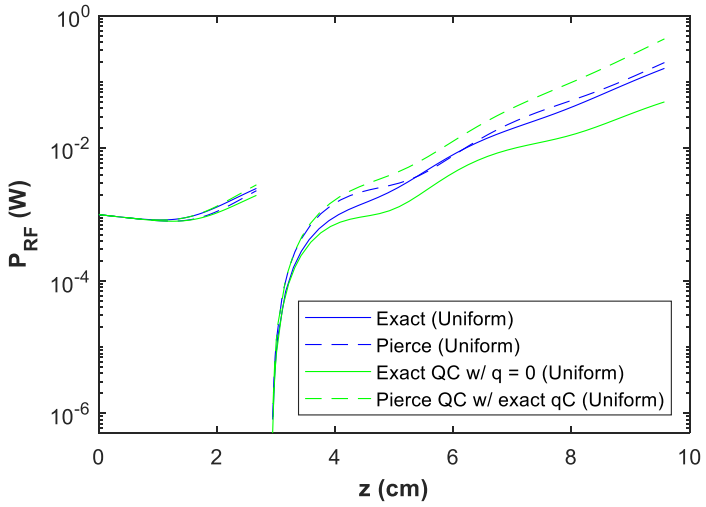

Figure 2.6: Comparison of four RF power profiles using uniform attenuation profile at 4.5 GHz with input power of 1mW: (i) Exact case (ii) Pierce case, (iii) Exact case but artificially setting $q = 0$ (iv) Pierce case but artificially setting QC to that of the Exact case.

attenuation in those regions in the non-uniform case. For both attenuation profiles, we find general agreement between the exact and Pierce theory over the length of the tube, although significant divergence is observed immediately after the sever. This discrepancy is due to the detuning effect of q, although Q is compensated which leads to good agreement between the two solutions (see Figure 2.3a). In other words, trying to artificially include the effects of q in the Pierce approach

or, vice versa, setting $q = 0$ in the Exact approach results in a much greater discrepancy, as shown in Figure 2.6.

2.4 Conclusions

This chapter describes an exact linear theory of a lossy tape helix TWT that includes the space charge effects on both the beam mode and in the circuit mode, comparing its results to those of the classical Pierce theory [12], [13]. The effects of uniform and non-uniform cold-tube loss are readily incorporated.

We found that for the uniform loss case, the exact and Pierce theories agree well only in a restricted frequency range. This discrepancy arises from the approximate formula for interaction impedance used in the Pierce theory, which only incorporates effects of the dominant beam and circuit modes, as opposed to the exact formulation which accounts for all higher order circuit and beam modes, including their space harmonics. At a frequency within this restricted range of agreement, we again compared the Pierce and exact theories for TWTs with realistic loss profiles and a sever, finding good agreement in the power along the length of the tube with only a slight discrepancy immediately after the sever region. We demonstrated how to account for the combined effect of (q, Q, d) in the exact theory as compared to the classical Pierce theory.

We have separately found that if the loss tangent in a uniform tube is less than 0.03 there is little difference in the gain whether we use $(\beta_k, \beta_l, \beta_m)$ obtained from Eq. (2.4) as we have done in this paper, or the three complex roots of β that are obtained directly from the exact, hot tube dispersion relation [47], [48] with a complex ϵ.

Finally we note that when the beam voltage exceeds ~10 kV a relativistic formulation is necessary in order to ensure that an accurate value of the beam velocity, and therefore of the detune

factor $(\beta_e - \beta_p)$, is used in the dispersion relation. Otherwise the resulting error in the detune factor could become comparable or even greater than the detune effect due to q.

Chapter 3 Extensions of Johnson's Theory of Backward-Wave Oscillations in a Traveling Wave Tube

3.1 Introduction

In this chapter, we discuss how the stability of traveling wave tubes may be impacted by a phenomenon known as backward wave oscillation. The stable operation of a traveling wave tube may be disrupted by various types of unwanted oscillations, including regenerative, band edge, or backward wave oscillations (BWOs) [3]. Regenerative oscillations are caused when signals at or near the driven frequency or its harmonics reflect off mismatches at the inputs, sever, or outputs of the tube and are consequently re-amplified. Due to the high gain inherent to TWTs, these partially reflected waves may lead to regenerative oscillation if the gain between two points of reflection exceeds unity [79]–[81]. Band edge oscillations, also referred to as cutoff or π-point oscillations, occur near the zero group velocity point of the dispersion diagram for the slow wave structure, i.e. where the slope of the dispersion curve is zero. These zero group velocity points usually define the edges of the propagation bands in the dispersion diagram for the electromagnetic circuit. One form of these band oscillations is an "absolute instability" of beam interaction with a dispersive medium that requires an analysis via the Briggs-Bers criterion [23], [23], [80]–[84] in which the feedback was provided internally without explicit reflection at the ends. These absolute instabilities were analyzed in [81], [85], and much more thoroughly in [80], who pointed out the errors in [81], [85]. These band edge oscillations have also been proposed as a source of coherent radiation [20], [86].

Backward wave oscillation is actually one of the earliest mechanisms studied in TWTs for consideration of its stability [13], [50]. While TWTs achieve amplifier gain through the

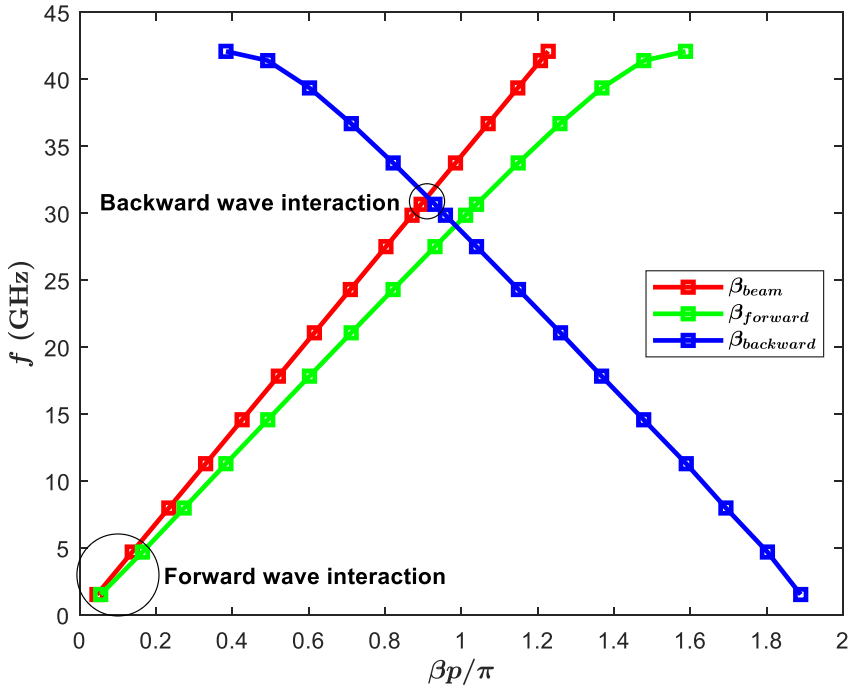

Figure 3.1: Dispersion diagram for traveling wave tube test case of Table 2.1 showing interaction of beam mode with forward & backward wave modes.

beam's synchronous interaction with the forward wave of the circuit, unwanted oscillation may also occur if this beam interacts with a backward wave of the circuit. Both types of interactions are identified in the dispersion diagram, Figure 3.1 (see also Figure 1.5), which shows the forward beam mode propagation constant ($\beta_{beam} = \omega/v_0$), the forward circuit wave propagation constant $\beta_{forward}$, and the backward circuit wave propagation constant $\beta_{backward}$. The forward (backward) wave interaction occurs where β_{beam} approximately equals to $\beta_{forward}$ ($\beta_{backward}$), signifying synchronous interaction. Backward wave interactions are distinct possibilities because the forward beam mode necessarily intersects some backward wave circuit modes in a slow wave structure [13], as also clearly shown in Figure 3.1 and Figure 1.5. Note that the backward wave modes have a forward (positive) phase velocity but a backward (negative) group velocity, implying that the power of the backward wave flows opposite to the

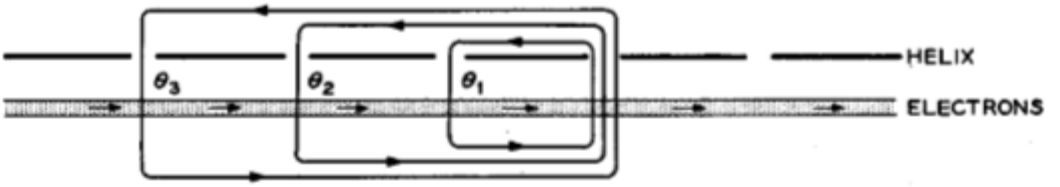

Figure 3.2: Electrons near a tape helix interacting with the fields in the helix gaps demonstrating how the backward wave interaction arises from internal feedback loops. Image from [13].

direction of the beam. In this case, the beam not only acts as a source of energy, as in the forward wave interaction, but also as a feedback path.

The process for backward wave gain is shown in Figure 3.2 for a tape helix TWT. Consider the electrons on the outer edge of the beam, i.e. adjacent to the tape helix circuit. The gaps between the tape may be considered points of interaction between the beam and the wave traveling on the helix circuit. The resulting coupled system effectively comprises a series of internal feedback loops where the total phase shift around each loop is an integral multiple of 2π radians [13]. Consequently, if the gain per feedback loop is small, this interaction may be exploited to amplify some input signal in a backward wave amplifier configuration [87], [88]. However if the gain is sufficiently high, oscillations may build up from noise and the tube instead acts as a highly tunable *source* of radiation, i.e. a backward wave oscillator [50], [88]. However, in a standard TWT, this backward wave interaction is unwanted; it may interfere with the normal operation of the device and must be suppressed or avoided via specific design choices, such as the inclusion of lossy attenuators to prevent feedback [3], [89]. In this chapter, we discuss how the stability of traveling wave tubes may be affected by backward wave oscillations. In particular, we examine how the onset of these oscillations is affected by random manufacturing errors in the slow wave structure. We also explicitly include end reflections

The classical theory for the onset of backward wave oscillations in a TWT for a uniform circuit with no end reflections was developed by Johnson [50]. As we will show, this theory

gives a pair of values of the Pierce gain and detune parameters C and b which describe, respectively, the threshold electron beam current that must be exceeded for BWO to occur and the frequency at which it will occur. Note that the gain parameter C for the backward wave is different from the C for the forward wave that was described in Chapter 2. At beam currents greater than the threshold, the output power increases with beam current while oscillation frequency decreases slightly; this effect is called frequency pushing [13]. Interestingly, Johnson's threshold conditions depend *only* on the other two Pierce parameters QC and d, i.e. the space charge and cold tube loss parameters, both evaluated at the BWO frequency. These two parameters are (loosely) considered to be of secondary importance, so it is mildly unusual, intuitively, that they become the sole predictors of the much more significant gain and detune parameters according to Johnson's theory. Another complicating issue is that, as pointed out in the previous chapter, the space charge parameter QC is notoriously difficult to accurately calculate for a realistic slow wave structure. Nevertheless, Johnson reported that his theory yielded good agreement with experimental observations [50], though we have no way to verify such claims because of the insufficient details provided in Johnson's old paper. We shall see that more recent dedicated experiments on BWO in a TWT could not readily be explained by the Johnson's theory, as described next.

The work in this chapter was in part motivated by a test experimental helix TWT built by L3 Technologies, designed specifically for the study of BW excitation in a TWT. However, despite meeting the conditions predicted by Johnson's theory, the tube failed to oscillate and remained stable. A preliminary report of this experiment and the comparison with Johnson's theory was presented as a conference abstract [90]. While our extensions of Johnson's theory, given here, were not able to explain why this dedicated tube did not oscillate, these examples

serve as an important reminder that BWO suppression is a serious issue that is not yet fully understood, particularly in an experimental context.

3.2 Johnson's theory of backward wave oscillation

For a uniform tube, Pierce's 3-wave dispersion relation for the backward wave with $e^{j\omega t - j\beta z}$ dependence is given by [See Eq. (1.39) and the discussions after Eq. (2.10)]

$$(\delta^2 + 4QC)(\delta + jb - d) = j \tag{3.1}$$

A full derivation of this backward wave dispersion relation will not be provided here, but is available in textbooks such Refs.[2], [13]. Chiefly, the forward beam mode is still described by the linearized force law, Eq. (2.4), in which the circuit wave amplitude, a, now represents the backward wave circuit mode, which is represented by the second parenthesis of Eq. (3.1), and its excitation by the AC beam current. In the present notation, it is given by Sengele et al. [89]. Thus, there is a close resemblance between Eq. 3.1 and Eq. 1.39, (which is the forward wave dispersion equation); they only differ by a few negative signs (See Sengele et al. [89]). If the circuit parameters are allowed to vary along the tube axis z, the three waves are governed by the non-dimensional differential equation [65]

$$\frac{d^3 f(x)}{dx^3} + jC(b + jd)\frac{d^2 f(x)}{dx^2} + C^2(4QC)\frac{df(x)}{dx} + jC^3\,(4QC(b + jd) - 1)f(x) = 0 \tag{3.2}$$

derived in a similar manner to that of Eq. 2.7, where as before, $x = \beta_e z$ is the normalized axial distance, $f(x) = e^{jx}s(x)$ and $s(x)$ is the small signal displacement of an electron from its unperturbed orbit. In terms of f, the circuit wave rf electric field $a(x)$ evolves according to

$$\frac{a(0)}{a(x)} = \frac{f''(0) + 4QC^3 f(0)}{f''(x) + 4QC^3 f(x)} = \frac{1}{f''(x) + 4QC^3 f(x)} \tag{3.3}$$

where we have used the initial conditions

$$f(0) = 0,\ \ f'(0) = 0,\ \ f''(0) = 1 \tag{3.4}$$

which represent, respectively, zero AC current, zero AC velocity, and unit output electric field in the linear theory [63], [65], [68].

To study the backward wave interaction, first consider a backward wave amplifier that produces a circuit wave of amplitude $a(0) = 1$ at the output location $z = 0$, as implied by Eqs. (3.3) and (3.4). The input signal is located downstream at $z = L$, as shown in Figure 3.3. For a uniform tube, we may solve for the electric field at $z = L$ by summing up all the electric field contributions from each of the three waves as follows (Eq. 11.1.15 of [13])

$$\frac{a(\beta_e L)}{a(0)} e^{j2\pi N} = \frac{\delta_1^2 + 4QC}{(\delta_1 - \delta_2)(\delta_1 - \delta_3)} e_1^{2\pi\delta_1 CN} + \frac{\delta_2^2 + 4QC}{(\delta_2 - \delta_3)(\delta_2 - \delta_1)} e_1^{2\pi\delta_2 CN} + \frac{\delta_3^2 + 4QC}{(\delta_3 - \delta_1)(\delta_3 - \delta_2)} e_1^{2\pi\delta_3 CN} \tag{3.5}$$

where $N = \beta_e L/2\pi$ is the length of tube, measured in the number of axial wavelengths of the beam mode, and δ_1, δ_2 and δ_3 are the three roots of the 3-wave dispersion relation, Eq. (3.1). At the threshold conditions for backward wave oscillations, the tube must produce some finite non-zero output at $z = 0$ for zero input signal, i.e. a zero drive instability. Thus the LHS of Eq. (3.5) is set to zero to obtain the Johnson threshold condition for backward wave oscillation [13], [50]

$$0 = \frac{\delta_1^2 + 4QC}{(\delta_1 - \delta_2)(\delta_1 - \delta_3)} e_1^{2\pi\delta_1 CN} + \frac{\delta_2^2 + 4QC}{(\delta_2 - \delta_3)(\delta_2 - \delta_1)} e_1^{2\pi\delta_2 CN} + \frac{\delta_3^2 + 4QC}{(\delta_3 - \delta_1)(\delta_3 - \delta_2)} e_1^{2\pi\delta_3 CN} \tag{3.6}$$

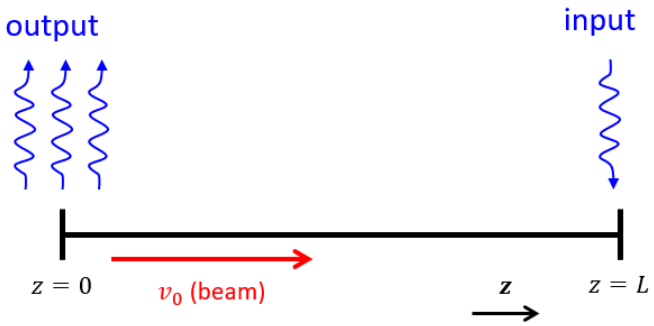

Figure 3.3: Schematic for a backward wave amplifier. If the beam current is sufficiently high, the tube acts as an oscillator, generating an output signal from noise even when the input signal is zero.

In Johnson's theory, it is assumed that QC and d are given. The analytic equations (3.1) and (3.6) are solved numerically to yield values of CN (determining starting length or threshold current) and b (determining BWO frequency). These two values, CN and b, are determined by requiring that the real and imaginary parts of Eq. (3.6) equal to zero. Thus, the threshold current and the oscillation frequency of BWO, according to Johnson's theory, depend only on the secondary parameters, QC and d. For $QC = 0$ and $d = 0$, Johnson found $CN = 0.314$ and the $b = 1.522$. For nonzero values of QC and d, the values of CN and b are tabulated [50]. Johnson claimed that his threshold condition gave good agreement with experiments, but there was insufficient information for us to validate such claims, as the values of QC and d are largely unknown for the experiments.

While the procedure given above is only valid for a uniform tube, it is straightforward to extend it to non-uniform tubes by applying the same strategy to Eq. (3.2). Here, we enforce the zero drive unstable condition by finding the pair of values of CN and b that minimizes the value of the electric field at the input $z = L$, i.e. forcing $f''(L) + C^2(4QC)f(L)$ to zero. The methodology for this approach will be described in more detail in the next section when we include the effects of random variations in the phase velocity due to manufacturing errors [76].

3.3 Effects of random manufacturing errors

Random manufacturing errors in the slow wave structures of TWTs have been shown to significantly affect TWT performance as well as the manufacturing yield and cost [63], [66]–[68], [89]. This problem becomes increasingly pernicious as the frequency range of TWTs is extended into the sub-mm or THz regimes, since the length scale of the periodic elements in the slow wave structure must drop accordingly; deformations in this structure therefore become comparatively more common and significant [65]. Previous work on this topic has demonstrated that introducing random variations in the Pierce parameters, especially in the detune parameter b, along the axis of the tube results in significant variations in gain and phase for the forward wave using Pierce's 3-wave theory [64], [68]. Including the effects of multiple internal reflections using Pierce's 4-wave theory further increased the variation in gain and phase and led to small-signal gain ripples across the band of operation [91]. Sengele et al. [65] also introduced variations in the Pierce parameters to study the backward wave, but neglected the effect of multiple internal reflections. They found that random variation in the phase velocity (effected through the Pierce detune parameter b) also had a large effect on backward wave gain while only having a minor effect on the forward-wave mode behavior, leading them to suggest that a device with such errors may be more stable against unwanted oscillations. Here, we explore how these circuit phase velocity variations *directly* affect the onset of backward wave oscillation using Johnson's theory.

We assume that there is random variation only in Pierce's detune parameter b, while all other parameters C, QC, and d are assumed to be constants in Eq. (3.2). We set $b(x) = b_0 + b_1(x)$ where b_0 is a constant mean value and $b_1(x)$ is the perturbative quantity that is obtained by linearly interpolating between randomly generated neighboring "nodes", as shown in Figure

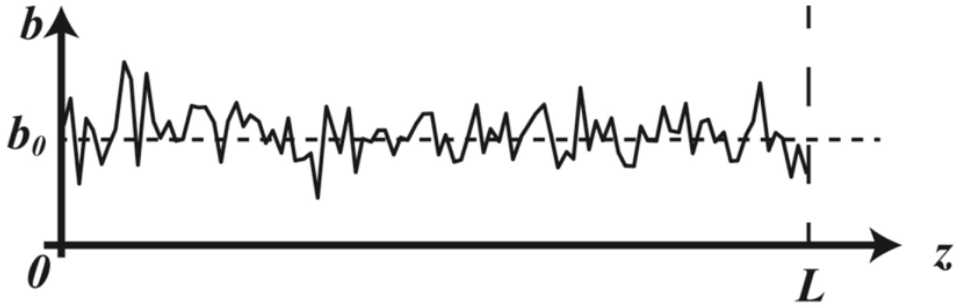

Figure 3.4: Example of random variations along tube axis; *b* is Pierce's detune parameter.

3.4 [64], [65], [92]. We set $x = \beta_e L = 100$, and the value of b_1 at $x = 1,2,3, \ldots ,100$ is set by an independent Gaussian random number generator with a specified standard deviation σ_b. The standard deviation in the circuit phase velocity, σ_q, where $q = (v_p - v_{p0})/v_{p0}$, is approximately related to σ_b, by $\sigma_b = (\sigma_q/C)(1 + Cb_0)$ [64].The piecewise linear function shown in Figure 3.4 serves as one "case" that simulates a TWT with random variations in the phase velocity. To obtain good statistics, 1000 such cases were generated, each of which was applied to Eq. (3.2).

To extract the threshold BWO conditions, we have to determine the values of b_0 and C that solve the third order differential equation, Eq. (3.2), subject to the initial conditions in Eq. (3.4), which yield a zero normalized circuit electric field at $z = L$. This was done through the use of the unconstrained optimization algorithm "fminsearch" in Matlab, which uses the Nelder-Mead simplex algorithm described in Lagarias et al [93]. For each random sample $b_1(x)$, an initial guess at the value of b_0 and C is provided by the pristine tube solution. The optimization algorithm is then run; this essentially guesses values of b_0 and C, solves Eq. (3.2) for each guess, then tries to find the guess that minimizes the value of the electric field, i.e. $f''(x) + C^2(4QC)f(x)$ at $x = 100$. To validate this approach, an error-free case was run with $QC = 0$ and $d = 0$ with an arbitrary initial guess; this resulted in values of $b = 1.522$ and $C = 0.0197$. Since $x = \beta_e L = 100$, $N = 100/2\pi = 15.92 \Rightarrow CN = (0.0197)(15.92) = 0.314$. These values match the published results

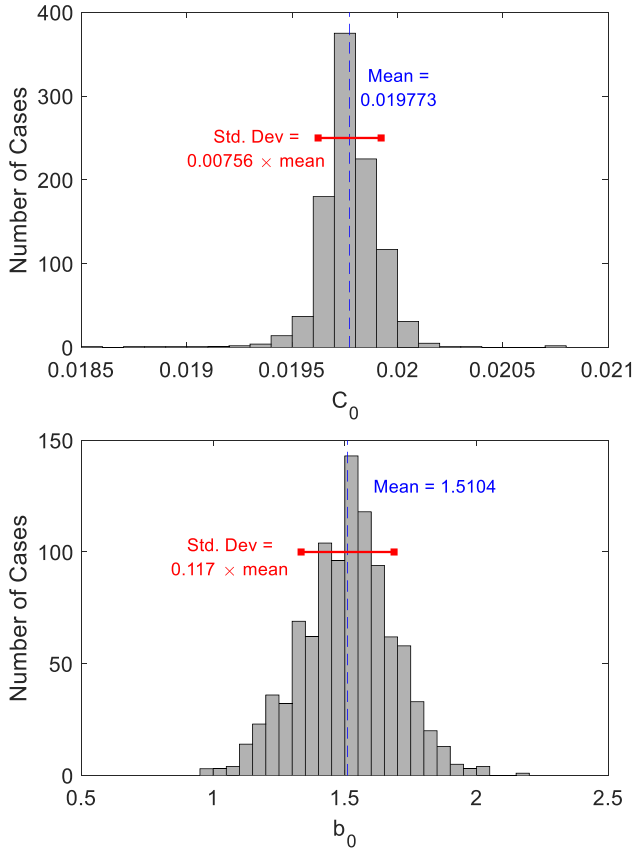

Figure 3.5: Distribution in threshold for the *QC = 0, d = 0* case. (a) Top, Pierce gain parameter *C* and (b) bottom, detune parameter *b* for variations in detune parameter σ_b = 1.7 (corresponding to standard deviation in circuit phase velocity of 3.4%).

of Johnson under the same conditions of $QC = 0$ and $d = 0$ [13], [50], also quoted above in the paragraph after Figure 3.3.

The statistical distribution of the threshold value of Pierce's gain parameter C for the onset of BWO is shown in Figure 3.5 for these 1000 cases, setting $d = 0$, and $QC = 0$. Here we see that the BWO threshold for C_0 (Figure 3.5a) was only minimally affected by random variations in the phase veolocity. As noted in [13], backward wave oscillation can principally be considered an interference effect between various waves as opposed to the growing wave effect of forward wave amplifiers. This relative insensitivity of Johnson's BWO threshold is likely due to the cancellation of all three waves at $z = L$ and therefore the sensitivity of b that

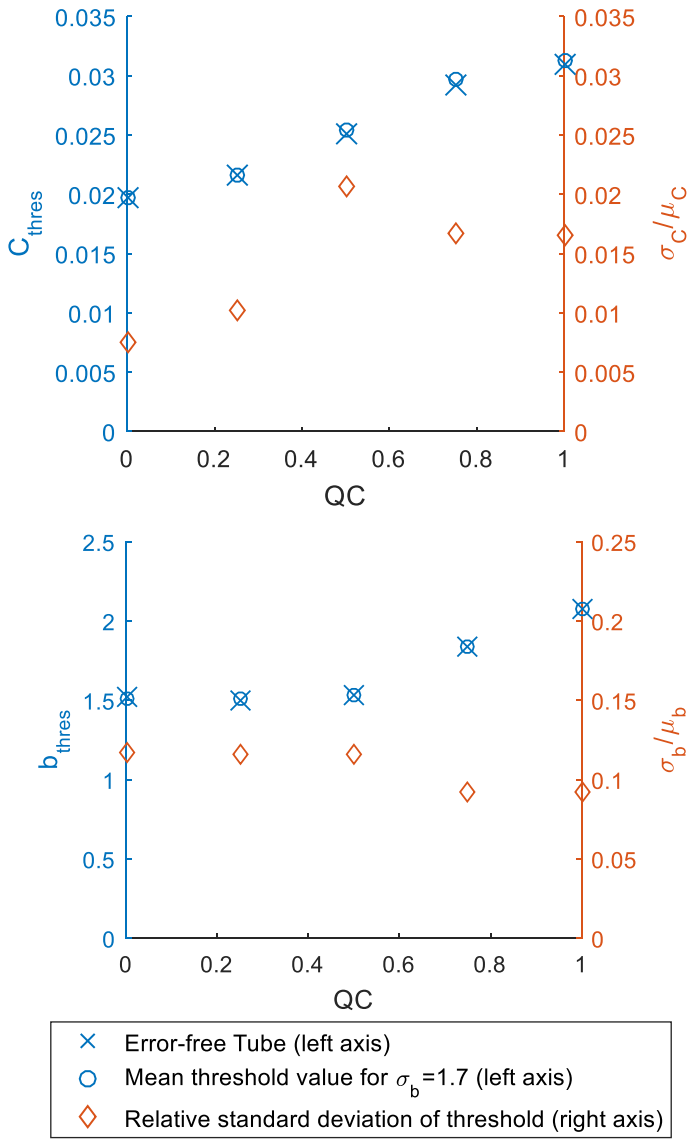

Figure 3.6: Means and relative standard deviations of (a) gain parameter *C* and (b) detune parameter *b* as a function of *QC*.

characterizes synchronous interaction is of lesser importance. The large spread in b_0 shown in Figure 3.5(b) was self imposed as we assumed $\sigma_b = 1.7$. The corresponding spread in BWO frequency is $C\sigma_b = 3.4$ percent since $C = 0.02$ from Figure 3.5(a). The spread in the threshold current, i.e., in C^3, is also of order 3.4 percent (not shown). The effect of nonzero QC is shown in Figure 3.6, which shows that the value of threshold C increases by 50 percent as QC increases from 0 to 1. Figure 3.6 shows that the mean values of threshold C and b are very close

to those in an error-free tube, and that for $QC > 0.25$, to a good approximation, $b_{thres} \cong \sqrt{4QC}$ and $C_{thres} \cong \frac{(QC)^{\frac{1}{4}}}{2N}$, as established by [50]. See also p. 407 of [13].

3.4 Effects of end reflections

Next, we assume an error-free tube to analyze the effect of end reflections on the BWO threshold, again following Johnson's theory. We remark that this approach is very different from that of Levush et al. [94], who also studied BWOs including end reflections. However, it is difficult to compare our work to that of Levush et al. since the latter authors did not formulate their theory in terms of the Pierce parameters and therefore did not show the explicit dependence on QC and d, as Johnson does. Another point of difference is that Levush et al. assumes the circuit is lossless, so their theory cannot readily be used to compare with BWO experiments that exhibit cold tube loss. Furthermore, Levush et al's threshold condition depends explicitly on the group velocity of the backward circuit mode, whereas the group velocity, as well as the backward wave signal propagation time, does not enter explicitly in Johnson's theory. We have consequently not been able to determine the precise relation between the approach and results of Levush et al. [94] and those of Johnson [50]

To consider the effects of end reflections on Johnson's BWO thresholds, we add the forward wave a_f of the circuit electric field to the backward wave a_b of the circuit electric field, as shown in Figure 3.7. Note that $a_b$was denoted as a in Eqs. (3.3) and (3.5). To simplify the analysis, in this section we suppress the axial variations in all Pierce parameters. At the BWO oscillation frequency, the forward circuit wave hardly interacts with the electron beam, so we assume that it has a constant amplitude between $z = 0$ and $z = L$, while the backward wave

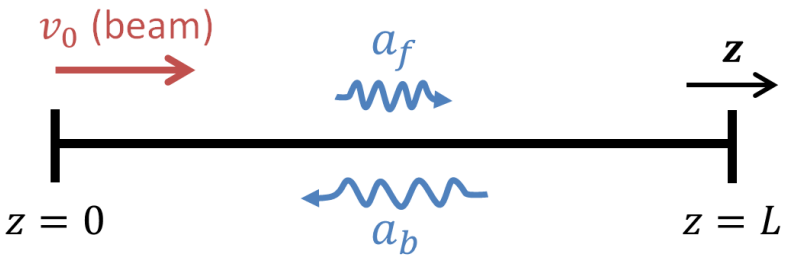

Figure 3.7: Forward and backward waves for end reflection model.

circuit electric field, a_b, could vary with z in general to accommodate its interaction with the beam. Thus, we write

$$a_f = \widetilde{a_f}\exp(j\omega t - jk_f z) \tag{3.7}$$

$$a_b = \widetilde{a_b}(z)\exp(j\omega t) \tag{3.8}$$

where $\widetilde{a_f}$ is a constant and k_f is the wavenumber of the forward propagating circuit mode, assuming no attenuation. The forward circuit wave has no gain since the beam's velocity is very different from the phase velocity of this forward wave at the BWO frequency (Figure 3.1). We next define the reflection coefficients R_0 and R_L, at $z = 0$ and at $z = L$, respectively, as

$$R_0 \equiv \frac{a_f(z=0)}{a_b(z=0)} \tag{3.9}$$

$$R_L \equiv \frac{a_b(z=L)}{a_f(z=L)} \tag{3.10}$$

Multiplying the two equations (3.9) and (3.10), we construct a composite reflection coefficient R with an associated phase θ as follows

$$\frac{a_b(z=L)}{a_b(z=0)} = R_L R_0 \frac{a_f(z=L)}{a_f(z=0)} = R_L R_0 \mathrm{e}^{-jk_f L} \equiv Re^{j\theta} \tag{3.11}$$

where we have used Eq. (3.7) and defined $R = |R_0 R_L|$. Inclusion of attenuation in the forward wave in Eq. (3.7) would only change the composite reflection coefficient, R. The effects of end reflections on the BWO threshold condition may be therefore obtained by inserting Eq. (3.11)

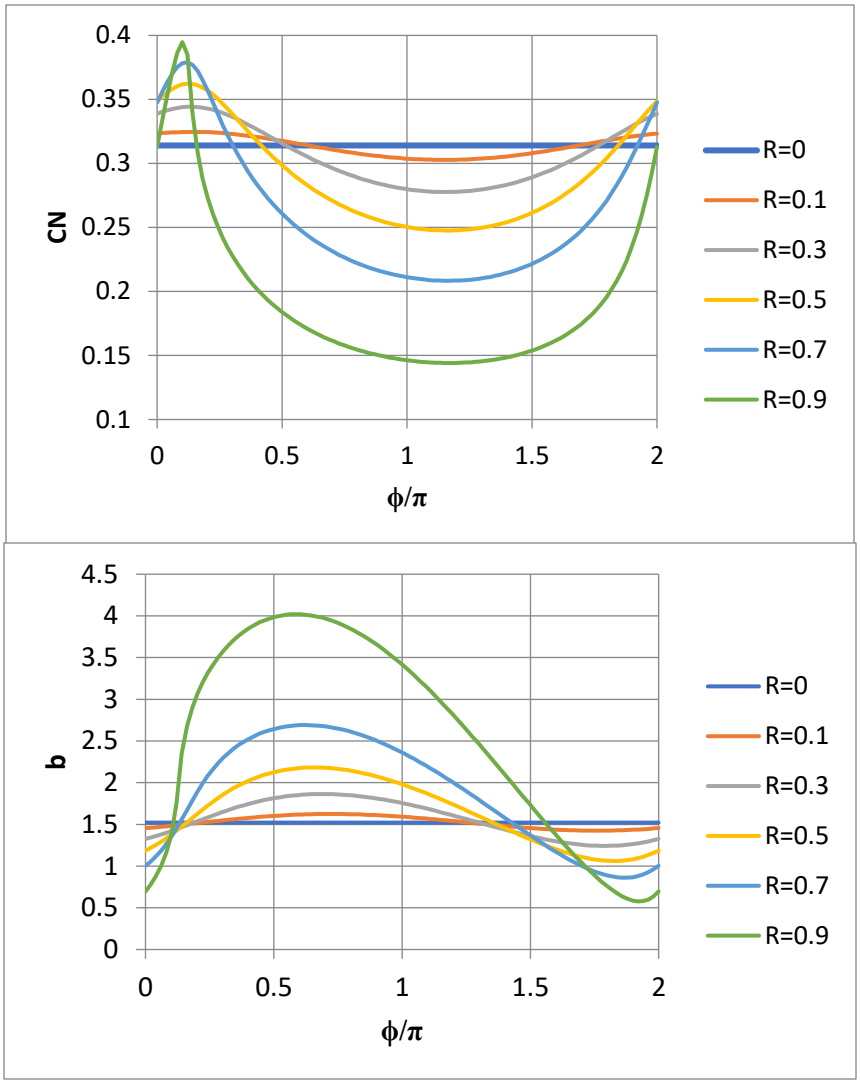

Figure 3.8: Effect of end reflections on the threshold BWO conditions (a) top, for *b* and (b) bottom, for *CN* for the *QC = 0, d = 0* case.

into Eq. (3.5), resulting in the following expression of Johnson's threshold condition including end reflections

$$Re^{j\phi} = \frac{\delta_1^2 + 4QC}{(\delta_1 - \delta_2)(\delta_1 - \delta_3)} e_1^{2\pi\delta_1 CN} + \frac{\delta_2^2 + 4QC}{(\delta_2 - \delta_3)(\delta_2 - \delta_1)} e_1^{2\pi\delta_2 CN} + \frac{\delta_3^2 + 4QC}{(\delta_3 - \delta_1)(\delta_3 - \delta_2)} e_1^{2\pi\delta_3 CN} \tag{3.12}$$

where $\phi = \theta + 2\pi N$. If $R = 0$, Eq. (3.12) reduces to Johnson's standard BWO threshold condition, i.e. Eq. (3. #6). This is the case when the slow wave TWT circuit is perfectly matched at either terminations, at $z = 0$ or at $z = L$, implying $R = 0$.

We then use an interior-point algorithm [95] with the "fmincon" Matlab optimization function to find the threshold values of b and CN that satisfy Eqs. (3.1) and (3.12) in the zero space charge and zero circuit loss ($QC = 0, d = 0$) case for a range of $R \in [0,1]$ and $\phi \in [0,2\pi]$. These solutions, given in Figure 3.8, show that end reflections can have a significant impact on the threshold conditions depending on the magnitude of the reflection coefficient. From Figure 3.8a one can claim that end reflections tend to decrease the required starting current, a result largely consistent with Levush et al.[94], whose formulation is very different from Johnson's [50].

An example with nonzero values of QC and d was also studied; this is the test TWT constructed by L-3 Technologies that did *not* oscillate, despite exceeding the threshold current predicted by Johnson's theory [90]. The threshold conditions for this case are presented in Figure 3.9 for values of R up to 0.14. However, at higher reflection coefficients ($R > 0.14$), the transcendental equation, (3.12), does not have a meaningful solution, similar to the case of N which satisfies $A = \cos(2\pi N)$ when A > 1. When no threshold condition can be found, this means that BWO does not exist for the set of parameters QC, d, R, and ϕ. Whether this is indeed the case warrants further study.

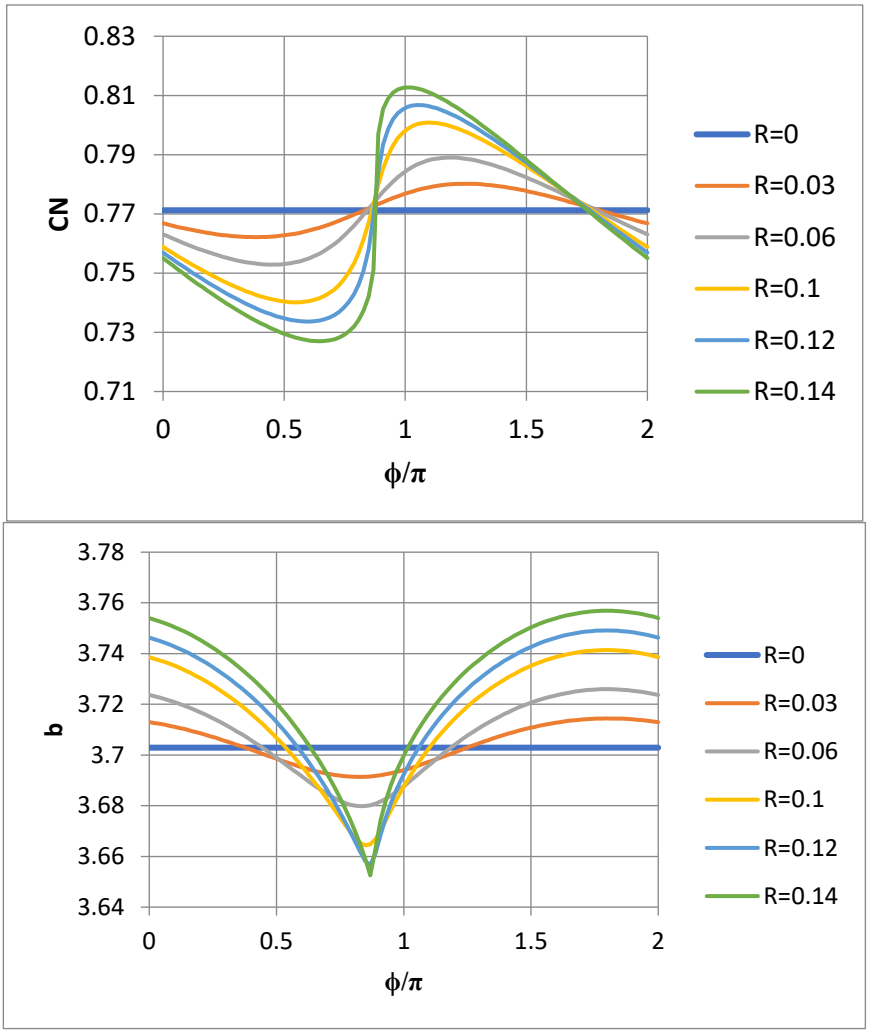

Figure 3.9: Effect of end reflections on the threshold BWO conditions (a) top, for *b* and (b) bottom, for *CN* for the *QC* = 3.392, *d* = 0.135 case (L3 Technologies test TWT) [90].

3.5 Inclusion of circuit mode space charge

Thus far in our analysis of the backward wave, we have neglected to include the effect of space charge on the circuit mode, characterized by q. This effect of q for the forward wave interaction has been included in Eq. (2.4), where q is computed exactly for the tape helix TWT. For the backward wave oscillator problem, we shall enter q phenomelogically, as in Eq. (3.13) below, and then examine its effect on Johnson's BWO threshold condition. The reason follows.

Our attempts to solve for q from the exact hot tube dispersion relation [47] near the backward wave circuit mode (See Figure 3.1) have so far been unsuccessful. The exact

dispersion relation is a very complicated expression that admits three roots that correspond to the solution to Pierce's 3-wave dispersion relation [Eq. (1.39) for the forward wave case, Eq. (3.1) for the backward wave case]. The Pierce solutions may then be used as an initial "guess" for some root-finding algorithm solving the exact hot tube dispersion relation, yielding the 3 roots of β (See Eq. 2.2) that may subsequently be used to solve for the *exact* Pierce parameters $qC^3, QC^3,$ and C^3 (See Eq. 2.3). This procedure is relatively straightforward in the forward wave case, where the solution to Pierce's dispersion relation results in a growing and a decaying wave (β_1, β_2 are complex conjugates of each other) as well as a neutral oscillating wave (β_3 is purely real) and the exact dispersion relation readily yields corresponding solutions. However, in the backward wave case, the Pierce's dispersion relation instead gives 3 neutral roots, all purely real. Solving the exact hot tube dispersion relation across the frequency range of interest does not consistently yield corresponding roots and frequently gives spurious or 'false' roots that do not appear to correspond to any of the solutions of the Pierce dispersion relation. Whether this failure is due to some underlying physical reason or simply due to the extreme complexity of the exact dispersion relation remains unclear.

However, we may examine how q directly affects the backward wave oscillation threshold, putting aside the question of how to calculate q in the first place. Consider the modified dispersion relation in Chapter 2, Eq. (2.4), that includes both the effect of cold circuit loss (characterized by d) and space charge on the circuit mode (characterized by q). This may easily be rewritten in terms of the complex propagation constant δ to match the form of Eqs (1.39) & (3.1) as follows

$$(\delta^2 + 4QC)[\delta + jb - d + j\frac{\beta_{ph}}{\beta_e}(4qC^2)] = j \tag{3.13}$$

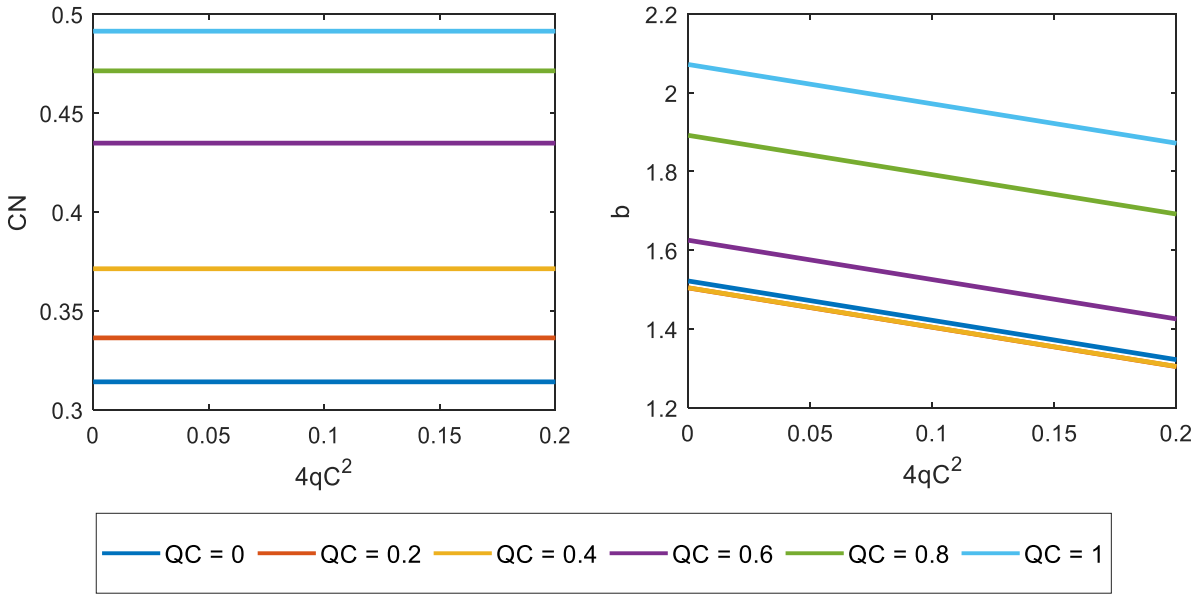

Figure 3.10: BWO threshold conditions (a) left, *CN* and (b) right, *b* as a function of $4qC^2$ for various values of *QC*.

Johnson's criterion for oscillation (Eq. 3.6), however, is unaffected. We may solve Eqs (3.13) & (3.6) for the threshold conditions b and CN for several values of q and Q setting $d = 0$, plotting the results in Figure 3.10. We observe that CN, i.e. the starting current, is unaffected by q; this is consistent with the random errors in circuit phase velocity having little effect on threshold CN (See Figure 3.5). Meanwhile, we note that b decreases linearly with $4qC^2$. Indeed, from a cursory examination of Eq. (3.13), we can see that q affects the dispersion relation in a similar manner to b, causing a detuning effect. Since the backward wave oscillation phenomenon arises from wave interference rather than an amplifying effect, it is therefore unsurprising that the starting current is unaffected while b, and therefore the oscillation frequency must drop to compensate for the detuning effect of q. Whether this drop in oscillation frequency with increased space charge effects on the circuit is related to the frequency pushing effect [13], [50] seen in backward wave oscillators when the starting current is exceeded remains an open question.

3.6 Conclusions

In this chapter, we have extended Johnson's classical theory for the onset of backward wave oscillations in a TWT to include the effects of random manufacturing errors along the TWT's axis. We found that these errors only minimally affect Johnson's threshold for the starting length while the BWO oscillation frequency and threshold current (at a fixed circuit length) were found to be affected to a similar degree as the variation in circuit phase velocity. This insensitivity is different from some previous works where large gain ripples in a forward wave TWT may result from random variations of the circuit phase velocity along the tube [91], in part due to our neglect of internal reflections that were carefully accounted for in Ref. [91], and in part due to Johnson's threshold arising from the cancellation of the three waves at the beam's downstream location, $z = L$, thereby reducing the sensitivity to the circuit phase velocity variations (i.e. to the detune parameter b). We next extended Johnson's theory to describe an error free tube with end reflections, showing that the threshold conditions depend sensitively on the phase and magnitude of the composite reflection coefficient. In the zero space charge, zero cold circuit loss case, we find that on average, the starting current is decreased due to the effect of reflections. Finally, we included the circuit mode space charge effect q in Johnson's threshold, demonstrating that BWO oscillation frequency drops with increased q, while the starting current remains unaffected.

Unfortunately, our generalizations of Johnson's theory did not explain why the L3 Technologies test helix TWT did not oscillate, despite exceeding the threshold current value. One reason, we suspect, is that the values of QC, d, the reflection coefficients, and/or the beam radius required for application of Johnson's theory (and its extensions) were not known with sufficient accuracy. Additionally, attempts to solve the exact hot tube dispersion relation [47] to

analyze backward wave operation have so far been unsuccessful due to the presence of spurious roots.

Chapter 4 Transitions Between Temperature-Limited and Space-Charge-Limited Operation for Thermionic Cathodes

4.1 Introduction

The previous two chapters concerned the interaction between the electron beam and the wave propagating on the slow wave structure. Here, we focus our attention solely on the generation of the electron beam using a thermionic cathode. Of major concern is the fundamental problem of the amount of anode current that is drawn from a cathode surface that emits electrons non-uniformly over the cathode surface, a practical problem rarely analyzed properly. This chapter offers a semi-analytic study of this difficult problem; in fact, it is the first rigorous analytic study of its kind.

For virtually all TWTs, the electron beam is formed by thermionic emission, despite significant progress towards a "cold cathode" TWT that relies on field emission [4], [96], [97]. In either case, for an electron to escape the cathode, it must overcome the potential energy barrier at the interface between the cathode and the vacuum into which it is emitted; this potential energy is known as the work function ϕ. Field emission relies on applying a large electric field normally to the cathode which distorts the shape of the potential barrier such that electrons may quantum mechanically tunnel through; the resulting current is given by the Fowler-Nordheim equation [98]. In thermionic emission, the cathode is heated so that the electrons may have sufficient energy to cross the barrier. As such, the emitted current density J_{RD} depends on the cathode temperature and the work function of the cathode, varying according to the Richardson-Dushman law [26], [27]

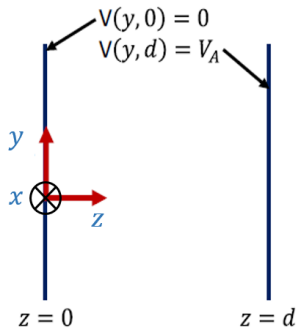

Figure 4.1: Planar diode geometry.

$$J_{RD} = A_0 T^2 \exp\left(-\frac{\phi}{kT}\right) \tag{4.1}$$

where A_0 =1.201732 ×10^6 A/(m·K)^2 is the Richardson coefficient, T is the cathode temperature in K and k is the Boltzmann constant. However, as discussed in Chapter 1, an increase in cathode temperature and emitted electron current is accompanied by an accumulation of charge due to these emitted electrons, which limits any further emission (see Figure 1.2). In a simple 1D model and assuming zero emission velocity, the maximum achievable current density at the anode is given by the Child-Langmuir law [28], [29]

$$J_{CL} = \frac{4}{9}\epsilon_0 \sqrt{\frac{2e}{m}} \frac{V_A^{3/2}}{d^2} \tag{4.2a}$$

which depends only on the diode gap distance d and gap voltage V_A while remaining independent of any cathode properties such as work function or temperature, and of emission mechanism. Eq. (4.2a) results from the constraint imposed by the Poisson equation. This current density limit is slightly modified if the electron velocity distribution is assumed to be Maxwellian [29], [31], since the extra electrons injected into the vacuum (now with non-zero emission velocities) increase the depth of the potential minimum and push its location slightly further into the anode-cathode gap. For a typical thermionic cathode, this potential minimum is typically located only a few tens of microns from the cathode surface, with a potential depth of 1 eV or less [3].The

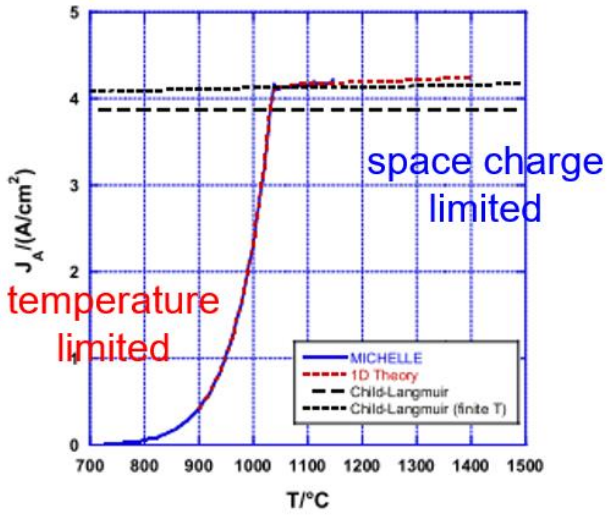

Figure 4.2: Miram curve for a 1D cathode V_A= 179.5 V and d = 0.381 mm and a uniform work function 2.0eV. The dashed curve corresponds to Eq. (4.2a) and the black dotted curve corresponds to Eq. (4.2b). Note the sharp transition at the knee at T = 1040°C. The excellent agreement between the theory and MICHELLE simulations means that the potential minimum, if it exists, is resolved in both [70].

potential minimum may be considered a virtual cathode, allowing the space-charge-limited current to be estimated using Eq. 4.2a when the gap distance d is reduced (to accommodate the position of the "virtual cathode" at which the electric field is zero) and the gap voltage is increased (to accommodate the additional dip at the virtual cathode). This effect causes a slight increase in space-charge-limited current density as the temperature of the cathode is increased. Langmuir [29] derived the space-charge limited current density, including these effects due to the Maxwellian distribution of emitted electrons at a finite cathode temperature, to be,

$$J_{CL}(\text{finite T}) = J_{CL} \times \left(1 + 2.66\left(\frac{kT}{eV_A}\right)\right)^{\frac{1}{2}} \tag{4.2b}$$

Both limiting current densities, Eqs. (4.2a) and (4.2b), are plotted in Figure 4.2 for a diode model to be studied in detail in this thesis.

The transition from the temperature-limited regime to this space-charge-limited regime is characterized by the Miram curve [69], a plot of anode current vs cathode temperature, while the

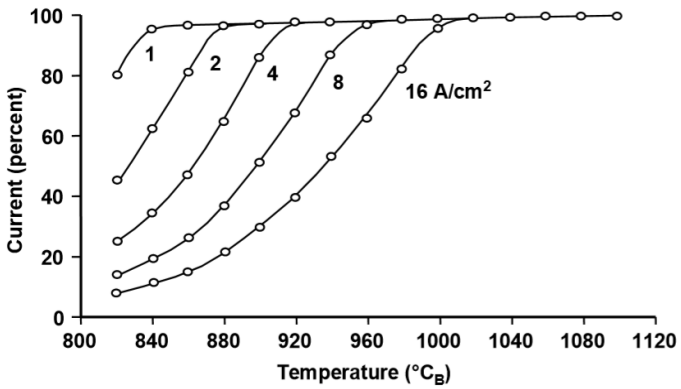

Figure 4.3: Experimental Miram curves for a good cathode. Image from [3].

transition region is referred to as the "knee" in the curve. This transition is quite sharp for an ideal cathode with a uniform work function, as shown in Figure 4.2, where results from the analytic 1D theory and particle simulations using MICHELLE [71] are shown. However, experimental curves show a much more gradual transition, yielding a smooth and rounded knee (See Figure 4.3). While the physical reasons behind this discrepancy have not been definitively identified, it has commonly been attributed to the complex surface morphology of the cathode, including spatially varying work function distributions and local field enhancement due to cathode surface roughness. Although the Schottky effect [99], a reduction in the effective work function barrier due to the applied electric field at the cathode, has also been proposed as a contributing factor [100], its effect on smoothing the curve is quite minor. This is an important issue, since thermionic cathodes for linear beam devices such as TWTs or klystrons are almost always operated in the vicinity of the knee [3]. The reasons follow.

The most commonly used thermionic cathodes in the microwave tube industry are dispenser cathodes, consisting of a porous tungsten matrix impregnated with a compound containing barium oxide, calcium oxide and aluminum oxide. When the cathode is heated to the operating temperature, the impregnant reacts with the tungsten, releasing barium that can migrate through the pores to the surface. Here, the barium may emit electrons far more readily than the

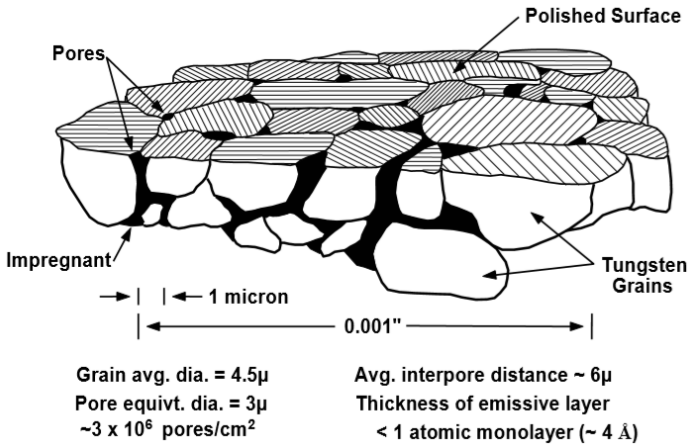

Figure 4.4: Patchy features at the surface of an impregnated dispenser cathode. Image from [3].

tungsten, due to barium's much lower work function (See Eq. 4.1). As such, the cathode surface is highly 'patchy', where the work function from patch to patch may vary drastically (See Figure 4.4, also [3]). The degree of barium surface coverage is then a balance of the diffusion of barium to the surface (from within the matrix) and the evaporation rate of barium from the surface, which is highly temperature dependent [3]. Depletion of the barium reserves inside the matrix is not the only concern; the evaporated barium may deposit on elements in the electron gun, causing arcing, which can lead to destructive failure of the device. As such, the ideal operating temperature for a cathode would be in the vicinity of the knee of the Miram curve, where the highest possible electron current density can be obtained for the lowest possible cathode temperature. This enhances the cathode life, because a 100°C reduction in the cathode operating temperature could increase the cathode life by one order of magnitude [3]. This has very significant practical implications for the operating life of a communications satellite because the traveling wave tube onboard is largely dictated by the life of its cathode. For these reasons, Longo [101] and Vaughan [102] proposed empirical rules for characterizing Miram curves, which were widely used [3], though they do not have a physical basis.

Characterizing the patchy work function distributions on the surface is a difficult matter. An adhoc "practical work function distribution" (PWFD) may be constructed directly from an experimental Miram curve [103]; this technique is frequently used in the TWT community [3]. The PWFD usually has a very sharp peak with a narrow spread of around 0.1 eV in the work function and has some practical value in tracking cathode performance over its lifetime. However, its construction does not have a sound physical basis and therefore may not be representative of the actual work function variations at the cathode surface, if at all. More detailed work by the University of Wisconsin using a combination of electron backscatter data [72] and density functional theory (DFT) [73] indicated that the cathode may consist of several discrete work function values over a fairly wide range ($\gg$ 0.1 eV). Also determined is the fractional cathode area occupied by each work function for a typical B-type cathode from L3 Technologies [70]. Surprisingly, over 20% of the cathode was found to be non-emitting, raising the question of whether a cathode could produce the current density predicted by the 1D Child-Langmuir Law, or even how the 1D Child-Langmuir law should be applied to patchy emission surfaces [104], [105].

A recent analysis by Chernin et al [70] incorporated this University of Wisconsin experimental data into calculations of the Miram curve using 3D particle-in-cell simulations using the MICHELLE electron gun code [71] and an analytical "1-1/2D" model. This analytical model solves the Poisson and Vlasov equations in 2D (details to follow) but assumes an infinite magnetic field in z (direction from cathode to anode, see Figure 4.1), thereby restricting all electron motion to the z-direction; this is the reason for the term "1-1/2D". The 1-1/2D model allowed the local work function $\phi(y)$ of the cathode to vary periodically in one spatial direction y along the cathode surface, forming work function 'stripes'. From this work, we reached the

following general conclusions: (a) electron motion parallel to the cathode surface does not significantly alter the smoothness or the shape of the Miram knee; that is, the shape of the Miram curve is insensitive to whether we assume $B = 0$ and $B = \infty$, (b) regions of different work functions do not emit independently; they compensate for each other via space-charge forces and, most surprisingly, (c) even with a significant non-emitting region, the total anode current obeys the 1D Child-Langmuir law as if the entire cathode surface were emitting. The compensatory current effect from (c) echoes the results of Umstattd & Luginsland [106] who show the formation of current density "wings" on the edges of 2D emitting patches under space charge limited conditions and assert that 20% of the active cathode surface may yield 80% of the 1D Child Langmuir current. Like these patches, low work function (highly emissive) regions are not bound by space-charge forces near their boundaries with non-emitting (high work function) regions, allowing them to provide a current density that locally exceeds the 1D Child Langmuir prediction. Thus, the enhanced emission at the wings can largely compensate for the non-emitting areas, to the extent that the total current reaching the anode is roughly governed by the 1D Child-Langmuir law, as if the entire cathode is emitting.

However, the 'striped' cathodes studied by the 1-1/2D model [70] did not quite generate the smooth transitions observed in experimental Miram curves, despite some significant "rounding" of the knees. By modeling cathodes where the width of each stripe (corresponding to some discrete work function) varies according to the fractional cathode area data calculated by the University of Wisconsin's team [72], including the non-emitting regions that were represented by $\phi = 10$ eV, Chernin [70] produced Miram curves that exhibited several distinct slopes. 3D MICHELLE simulations, performed by the Leidos scientists of [70], were able to reproduce these curves, even when using an applied magnetic field of $B = 0$ or 1 T,

demonstrating that the shape of the Miram curve is largely insensitive to changes in the magnetic field. However, if spatial variations are allowed in both the x and y directions along the cathode surface (See Figure 4.1), the 3D MICHELLE simulations do show a smooth and rounded curve, similar to experimental Miram curves. Therefore, it is of substantial interest to extend the 1-1/2D analytical model to 2-1/2D, allowing the local work function $\phi(x, y)$ to vary in both x and y directions on the cathode surface. The 2-1/2D model was the major contribution by the author. It takes significantly less computational time than MICHELLE to obtain essentially the same answers, as we shall see (Figure 4.8d below). The versatility of the 2-1/2D code may definitively answer whether the smoothness and roundedness observed in Miram curves is due mainly to the 2D effects in the work function distribution, or in large part due to the presence of significant non-emitting regions on the cathode. We may also readily examine a variety of idealized and realistic work function patterns to study how various factors, such as the length scale of work function variations and the appearance of a few local "bright spots" corresponding to highly emitting local spots, may impact the shape of the Miram curve. This chapter reports the author's findings on these issues.

In addition, we will present some results from [75] examining how Miram curves behave under the influence of a magnetic field that is applied orthogonally to the electric field, assuming a 1D model, i.e. assuming uniform electron emission from a thermionic cathode. The electron trajectories become curved through the action of the magnetic field, reducing the number of electrons reaching the anode as B increases. At some critical value $B = B_H$, called the Hull cutoff, an electron with zero emission velocity will barely miss the anode. We present results from particle-in-cell simulations (done by the author) validating an analytic formulation (done by Chernin) below the Hull cutoff. However, the author found that for thermal electron emission at

fields above the Hull cutoff, laminar electron flow within the diode breaks down into turbulent flow even at very low cathode temperatures. Some of these findings were published in [75], with more details given in Section 4.4 below.

4.2 Formulation of the 2-1/2D model

The theory extends the 1-1/2D model, which was originally developed by Chernin [70] to 2-1/2D [74]. Consider the planar diode schematic of Figure 4.1. Electrons are emitted from the cathode at $z = 0$ and are collected by the anode at $z = d$. The cathode is grounded, with potential $V = 0$, while the anode is at potential $V_A > 0$. An infinite magnetic field $B = B_z = \infty$ is also imposed, strictly limiting all electron motion to the z direction; this assumption, although apparently quite drastic, turns out to be adequate for the study of Miram curves, as shown in MICHELLE results which include both zero magnetic field and a strong magnetic field $B_z = 20$ T. These Miram curves do not deviate much from one another; all of this was demonstrated in the earlier 1-1/2D model. The work function $\phi(x, y)$ is allowed to vary across the cathode surface, but the Richardson coefficient A_0, cathode temperature T, and electrode potentials are assumed to be independent of both x and y. The Schottky effect [99] as well as the patch field effect [107], [108] are neglected; we only incorporate the isolated effect of space charge. We once more assume that all electrons are non-relativistic.

The electron distribution function may be calculated as a function of electron position (x, y, z) and velocity v_z as follows

$$f(x, y, z, v_z) = f_0(x, y)e^{-E/kT} = f_0(x, y)e^{\frac{-\left(\frac{1}{2}mv_z^2 + qV(x,y,z)\right)}{kT}} \tag{4.3}$$

where $f_0(x,y)$ is a normalization factor, E is the electron's total energy, m is the electron mass, q is the electron charge, and $V(x,y,z)$ is the electrostatic potential. Since x, y, and E are all constants of motion, f is a solution of Vlasov's equation.

The normalization factor $f_0(x,y)$ may be determined by asserting that the emitted current density at $z = 0$ is given by the local Richardson-Dushman current density $J_{RD}(x,y)$, (See Eq. 4.1) where the (x,y) dependence originates from the local value of the work function $\phi(x,y)$ on the cathode surface and noting that the current (momentum) density is the first order moment of the Vlasov equation. In fact, any arbitrary (x,y) dependence in $J_{RD}(x,y)$ may be included in Eq. (4.5) below, including the local value of the temperature and an arbitrary multiplier to designate non-emitting areas, or "hot spots" that are emitting at abnormally high values. The normalization factor will incorporate the unit of charge

$$\int_0^\infty dv_z v_z f(x,y,z=0,v_z) = J_{RD}(x,y) \tag{4.4}$$

The LHS of 4.4 reduces to an elementary integral, yielding

$$f_0(x,y) = \frac{1}{v_{th}^2} J_{RD}(x,y) \tag{4.5}$$

where $v_{th} = \sqrt{\frac{kT}{m}}$ is the thermal velocity.

Next, we solve Poisson's equation

$$\nabla^2 V(x,y,z) = \frac{\rho}{\epsilon_0} \tag{4.6}$$

where ρ is the charge density, calculated by integrating the distribution function over all possible values of velocity at that position.

$$\rho = \int_{v_{min}(x,y,z)}^\infty dv_z f(x,y,z,v_z) \tag{4.7}$$

The lower bound of this integral is $v_{min}(x,y,z)$, the minimum value of velocity of any electron originating at location (x,y) at the cathode reaching location z. This requires care, since the expression for v_{min} differs on either side of the potential minimum, if it exists.

If no potential minimum is formed within the gap, the potential an emitted electron would see as it travels from the cathode to the anode is a monotonically increasing function of z. In this case, $v_{min}(x,y,z)$ is the velocity at z of an electron emitted with zero velocity, so it follows via conservation of energy that

$$v_{min}(x,y,z) = \sqrt{\frac{2eV(x,y,z)}{m}} \tag{4.8}$$

when no potential minimum exists (to be precise, when the potential minimum is $V_m(x,y) = 0$ at the cathode, $z = 0$)

If a potential minimum $V_m(x,y)$ is formed at $z = z_m > 0$ within the gap, only electrons emitted from the cathode with a velocity greater than $\sqrt{\frac{2qV_m}{m}}$ will make it over the potential barrier and reach the anode, while the other electrons are reflected back to the cathode. Therefore for $0 < z < z_m$, which we define as the α-region

$$v_{min,\alpha}(x,y,z) = -\sqrt{\frac{2e(V(x,y,z) - V_m(x,y)}{m}} \tag{4.9}$$

while for $z_m < z < d$, which we define as the β-region,

$$v_{min,\beta}(x,y,z) = +\sqrt{\frac{2e(V(x,y,z) - V_m(x,y)}{m}} \tag{4.10}$$

Having defined $v_{min}(x,y,z)$ for all cases and for all locations within the A-K gap, we may continue to evaluate Eq. (4.7)

$$\rho = \frac{1}{v_{th}^2} J_{RD}(x,y) e^{eV(x,y,z)/kT} \int_{v_{min}(x,y,z)}^{\infty} dv_z e^{-\frac{\frac{1}{2}mv_z^2}{kT}} \tag{4.11}$$

The integral on the RHS may be treated by means of the complementary error function $erfc(u) = \frac{2}{\sqrt{\pi}} \int_z^{\infty} e^{-t^2} dt$, giving

$$\rho = \frac{1}{v_{th}} \sqrt{\frac{\pi}{2}} J_{RD}(x,y) e^{eV(x,y,z)/kT} erfc\left(\frac{v_{\min}(x,y,z)}{\sqrt{2} v_{th}}\right) \tag{4.12}$$

Finally, the expression of Poisson's equation may be given as

$$\begin{aligned} \nabla^2 V(x,y,z) &= \frac{1}{\epsilon_0 v_{th}} \sqrt{\frac{\pi}{2}} J_{RD}(x,y) e^{eV(x,y,z)/kT} erfc\left(\frac{v_{min}(x,y,z)}{\sqrt{2} v_{th}}\right) \\ &\equiv S(x,y,z) \end{aligned} \tag{4.13}$$

Although this expression is exact, the solution may only be obtained numerically, via a self-consistent iteration.

We now follow Chernin's 1D analysis [70] and extend it to consider a 2D distribution of work function on the cathode surface. The work function $\phi(x,y)$ is assumed to be periodic functions of (x,y) with periods p_x and p_y. We define N_x and N_y 'cell centered' values of x and y respectively as

$$x_i = \frac{i + 1/2}{N_x} \frac{p_x}{2} \tag{4.14}$$

$$y_j = \frac{j + 1/2}{N_y} \frac{p_y}{2} \tag{4.15}$$

for $i = 0,1,2,\ldots,N_x - 1$ and $j = 0,1,2,\ldots,N_y - 1$. We may then express the potential as a Fourier series

$$V_{ij}(z) = \frac{4}{N_x N_y} \sum_{l=0}^{N_x-1}{}' \sum_{m=0}^{N_y-1}{}' \tilde{V}_{lm}(z) \cos\left(\frac{2\pi l x_i}{p_x}\right) \cos\left(\frac{2\pi m y_j}{p_y}\right) \tag{4.16}$$

for $l = 0,1,2,\ldots,N_x - 1$ and $m = 0,1,2,\ldots,N_y - 1$ where the prime marks on the summations denote that the $l = 0, m = 0$ terms each have an additional factor of ½. We discretize the second derivatives with respect to x and y in (4.13) and reduce the 3D problem to a set of coupled 1D problems to find that $\tilde{V}_{lm}(z)$ satisfies

$$\frac{d^2}{dz^2}\tilde{V}_{lm}(z) - 2\left[\frac{1-\cos\theta_l}{\Delta x^2} + \frac{1-\cos\theta_m}{\Delta y^2}\right]\tilde{V}_{lm}(z) = \tilde{S}_{lm}(z) \tag{4.17}$$

where $\theta_l = \frac{\pi l}{N_x}$ and $\theta_m = \frac{\pi m}{N_y}$, and $\tilde{S}_{lm}(z)$ is the discrete Fourier transform of $S(x,y,z)$ [RHS of Eq. 4.13], which is given by

$$\tilde{S}_{lm} = \sum_{i=0}^{N_x-1}{}'\sum_{j=0}^{N_y-1}{}' S_{ij}\cos\left(\frac{2\pi l x_i}{p_x}\right)\cos\left(\frac{2\pi m y_j}{p_y}\right) \tag{4.18}$$

The required boundary conditions on $\tilde{V}_{lm}(z)$ are:

$$\tilde{V}_{lm}(0) = 0 \tag{4.19a}$$

$$\begin{cases} \tilde{V}_{lm}(d) = N_x N_y V_a \text{ for } l = 0, m = 0 \\ \tilde{V}_{lm}(d) = 0 \text{ otherwise} \end{cases} \tag{4.19b}$$

The computation of Miram curves for a defined work function distribution $\phi(x,y)$ thus uses the following procedure. We begin with an approximate solution for the potential which we denote as $V_{ij}^{(n)}(z)$ where the superscript (n) denotes the n-th approximation in our iterative solution. We then evaluate $S_{ij}(z)$ by computing the RHS of Eq. (4.13), which requires finding the potential minimum of $V_{ij}^{(n)}(z)$ and the use of Eqs. (4.8)-(4.10). Next, we compute the Fourier coefficients of $\tilde{S}_{lm}$ using Eq. (4.18) and solve Eq. (4.17) subject to the boundary conditions in (4.10) using, for example, the Thomas algorithm [109], [110] for tri-diagonal systems on a grid in z. We may then transform this solution back to $V_{ij}(z)$ using Eq. (4.16). As in [70], rather than

using $\tilde{V}_{lm}(z)$ as the $(n+1)$-th iteration, we denote this solution as $V_{ij}^{(n+)}(z)$ and instead define the next iteration of the potential as

$$V_{ij}^{(n+1)}(z) = \alpha V_{ij}^{(n)}(z) + (1-\alpha)V_{ij}^{(n+)}(z) \tag{4.20}$$

where the mixing parameter α is a real number satisfying $0 < \alpha < 1$. The value of α must be obtained empirically, but were typically set in a range from 0.8-1. We iterate this algorithm until the solution converges everywhere to 1 part in 10^4.

4.3 Results from 2-1/2D model of Miram curves

We use the same diode parameters as [70], setting $V_A = 179.5\text{V}$ and $d = 0.381\text{mm}$ and apply our 2-1/2D model to a variety of work function distributions to assess their impact on the Miram curve.

First, to demonstrate the space charge shielding effect (and its lack) and resulting current compensation that low work function regions have on their high work function neighbors, we begin with simple arrangements of two work functions: $\phi_1 = 2.0$ eV and $\phi_2 = 2.2$ eV (Figure 4.5). We compare the Miram curves resulting from a striped pattern (Figure 4.5a), first tested in [70], to its natural 2-1/2D analogue: a checkered pattern (Figure 4.5b), using two different values for the width of each stripe (and of each square side) $s = 53$ μm, 265 μm. For the following tests, unless indicated otherwise, 1024 simulation cells ($N_x = N_y = 32$) were used to model the cathode area while the vacuum region was discretized into $N_z = 500$ cells. Since the boundaries in x and y are periodic, the entire pattern as shown in. Figure 4.5a and b need not be simulated in its entirety; a smaller selection can be made such that each 'tile' is modelled by 256 (16x16) simulation cells. We see from Figure 4.5c that for both stripe widths, the current in the checkered case exceeds that of the striped case in the knee region, forming a slightly more rounded knee akin to an experimental Miram curve. Since the current compensation effect occurs primarily at

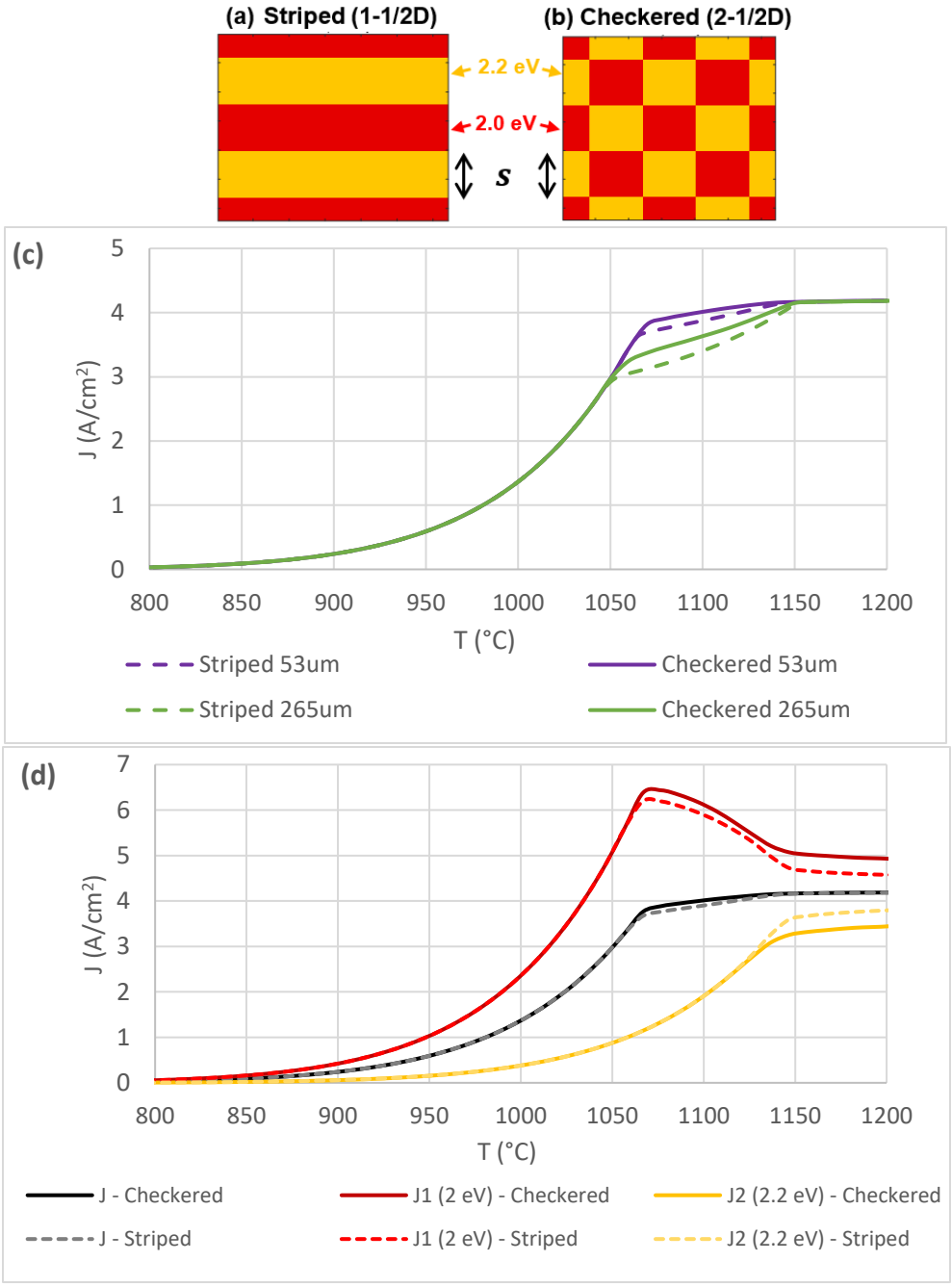

Figure 4.5: (a) Striped pattern (1-1/2D) (b) Checkered pattern (2-1/2D) (c) Comparison of striped vs checkered arrangements of ϕ_1 = 2.0 eV and ϕ_2 = 2.2 eV for two square/stripe widths s = 53µm, 265µm, (d) Separate current density contributions from ϕ_1 (red curves) and ϕ_2 (yellow curves) for checkered and striped cases, and the total current density (black curves). Here, s = 53µm. Note that at high temperatures, the 1D space charge-limited current densities of 4.2 A/cm^2 is attained (see Fig. 4.2).

the boundaries between different work functions, it is enhanced by an arrangement that emphasizes these boundaries, either by creating more of them or, as in the checkered case, by

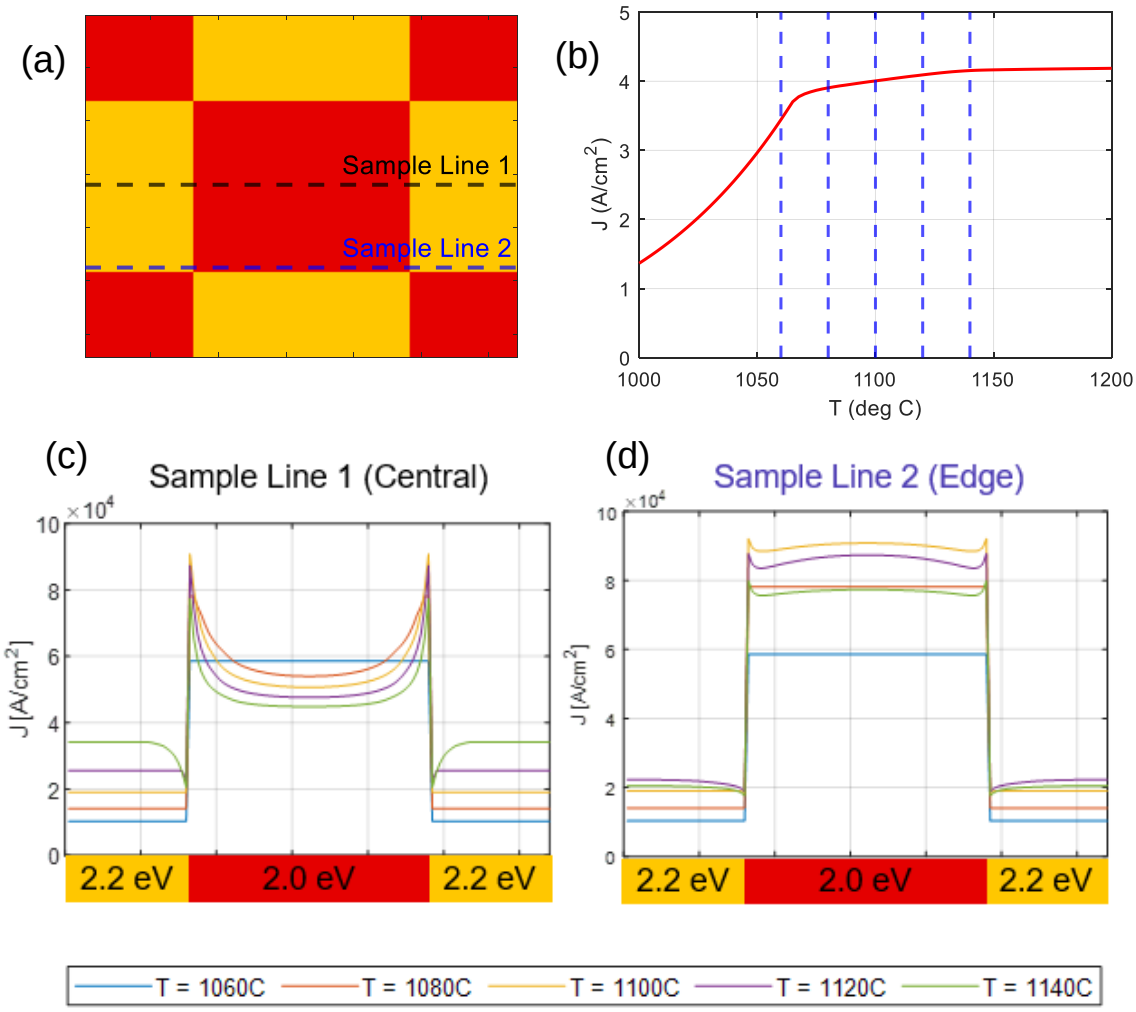

Figure 4.6: Current profiles sampled along the edge and center of the checkered pattern, *s* = 53 µm. (a) shows the location of the sample lines (b) shows the temperatures sampled around the knee. The current profiles for the central and edge lines are respectively given in (c) and (d).

causing additional current enhancement at the tile corners. We will demonstrate this local enhancement shortly. The compensation effect is examined in more detail in Figure 4.5d, which shows the current density contribution from each work function for the $s = 53$ µm case. The current from the higher work function regions (2.2 eV, yellow curves) has a typical Miram curve shape, showing the standard transition from temperature limited into space-charge limited operation. However, since they emit less than their 2 eV neighboring regions, the 2.2 eV regions have weaker space charge forces and a smaller potential minimum in front of them, near the

cathode. This allows the low work function neighbors (2 eV, red curves) to then locally exceed the Child-Langmuir current density to make up current. This effect continues well into the space-charge limited regime, acting in a way to force the overall cathode current density to obey the 1D Child-Langmuir Law (black curves in Figure 4.5d). That is, at sufficiently high temperatures, Figure 4.5c and d show that the 1D space-charge-limited current desnity of 4.2A/cm^2 is attained (compare with Figure 4.2)

This physics involved in Figure 4.5d may be made clearer by sampling the current density on the checkered pattern at various temperatures around the knee of the Miram curve. Figure 4.6a shows the location of the sample points, at lines along the center and edge of the checkered pattern while Figure 4.6b shows the temperatures that were sampled. The current profiles are given in Figure 4.6c & d. Note the peaked current density at the tile boundaries and tile corners due to the 2D space charge effect, similar to the current density 'wings' described by Umstattd & Luginsland [106], as well as the changes in current density from each region as the temperature is increased, in accordance with Figure 4.5.

Next, we replace one in every four 2 eV tiles in the checkered pattern with a non-emitting tile, modeled as having a 10 eV work function (Figure 4.7a) and labeled "checkered variant". The resulting Miram curves for $s = 53\mu m, 265\mu m$ compared to the standard checkered pattern is given in Figure 4.7b. First, we note that including a non-emitting region significantly lowers the current in the temperature-limited region and generally shifts the entire Miram curve to the right. The current is also reduced in the space-charge-limited regime, but this behavior is highly dependent on the tile size s. Smaller tile sizes increase the effective boundary regions where current compensation occurs, thereby sharpening the knee and allowing for a higher anode current at lower cathode temperatures. In addition, we observe that at sufficiently high

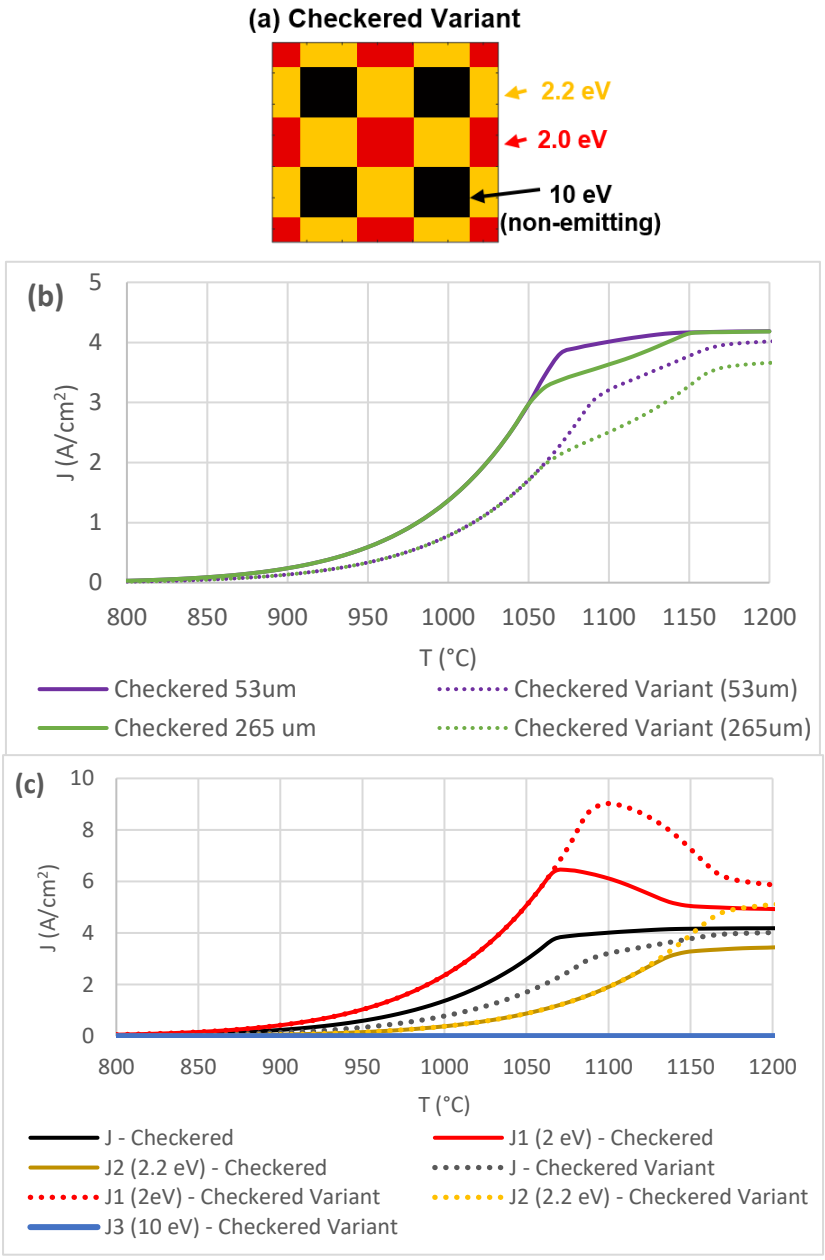

Figure 4.7: (a) Checkered variant pattern (b) Comparison of checkered vs checkered variant patterns for two square widths s = 53µm, 265µm, (c) Separate current density contributions from ϕ_1, ϕ_2, and non-emitting regions for checkered and checkered variant cases, s = 53 µm.

temperatures, both checkered variant cases eventually achieve the 1D Child-Langmuir current density (~4.2A/cm^2), apparently behaving as if the entire cathode were emitting. However, larger tile sizes significantly delay this process, highlighting the importance of the length scale of different work function regions on the cathode surface in determining the shape of the Miram

curve. [This effect of tile size may readily be seen in the hypothetical case where the tile size in Figure 4.7a is much larger than the AK gap spacing, *d*.] Figure 4.7d breaks down the current density contribution from each work function and demonstrates how *both* the 2.0 eV and 2.2 eV regions attempt to compensate current for the non-emitting region, which contributes effectively zero current in the operational temperature range. Under these conditions, the 2.0 eV regions are capable of supplying a current density over double the 1D space charge limit. Generally, we observe that the low work function regions contribute to the majority of the anode current, even when they make up a relatively small fraction of the cathode area, as is apparent when we study a more realistic representation of a cathode surface, as follows.

Table 4.1: Work function area distribution percentages

Work Function (eV)	Experiment [72]	Rand I	Rand II	Rand III
1.61	18.54	17.97	12.89	7.42
1.79	10.32	9.77	8.59	7.42
2.3	10.99	9.38	11.33	11.33
2.31	37.69	43.75	37.50	37.11
10 (non-emitting)	22.46	19.14	29.69	36.72

To model a real cathode, we first refer to the work function area distribution, labeled "Experiment [72]" in

Table 4.1. The data in this column are the percentages of cathode area for the indicated work function, obtained from electron backscatter diffraction measurements on a tungsten dispenser cathode [72]; the work function values were calculated using density functional theory (DFT) [73]. We once again note the sizeable fraction of non-emitting area that is typical of these cathodes (~22%, on the order of the checkered variant test in Figure 4.7a) as well as the ability of the cathode to retain the full 1D Child-Langmuir current at sufficiently high temperatures as if the entire cathode were emitting, as we shall also show shortly. We construct the work function

distribution pattern in Figure 4.8a (in which the “Rand I” case is generated by a random number generator to mimic “Experiment [72]” data). A random sequence of 256 work functions is generated from the distributions in Table 1. Each tile of work function has an area of 2.5μm × 2.5 μm and is modelled by 4 (2 × 2) simulation cells. Improving the resolution of this grid or testing different randomly generated patterns (with the same work function distribution) did not significantly alter our results. We also constructed two other patterns; in one, the size of the non-emitting area was boosted by 10% (Rand II, Figure 4.8b), while in the other it was increased by 15% (Rand III, Figure 4.8c). In both, the area of the 1.61eV regions was reduced to compensate. The resulting Miram curves are given in Figure 4.8d.

First, we note how the knee of Rand I appears much more rounded than its 2-1/2D counterparts by comparing with Figure 4.7b, indicating significant progress towards reproducing an experimental curve. (The smaller tile size used in Figure 4.8d than in Figure 4.7b is also a contributing factor, see below) Increasing the non-emitting area shifts the knee down and to the right, lowering the current density in the knee. In Figure 4.8d, we also include the results of a particle-in-cell simulation of Rand I using the MICHELLE code [71], in which a 20 T magnetic field was applied to restrict all electron motion to be parallel to the z axis. We observe excellent agreement across the various electron flow regimes: temperature-limited, space-charge-limited and the transition between them. We additionally remark that the computational time required to solve the anode current at a single temperature is on the order of hours for a MICHELLE simulation, compared to several minutes for the 2-1/2D code. We stress that this is an extremely rigorous numerical test in that both the 2-1/2D model and MICHELLE code need to resolve the potential minimum (if it exists) of each of the 256 tiles and the mutual electrostatic interactions among the tiles, consistent with the electron orbits that make up the charge distributions within

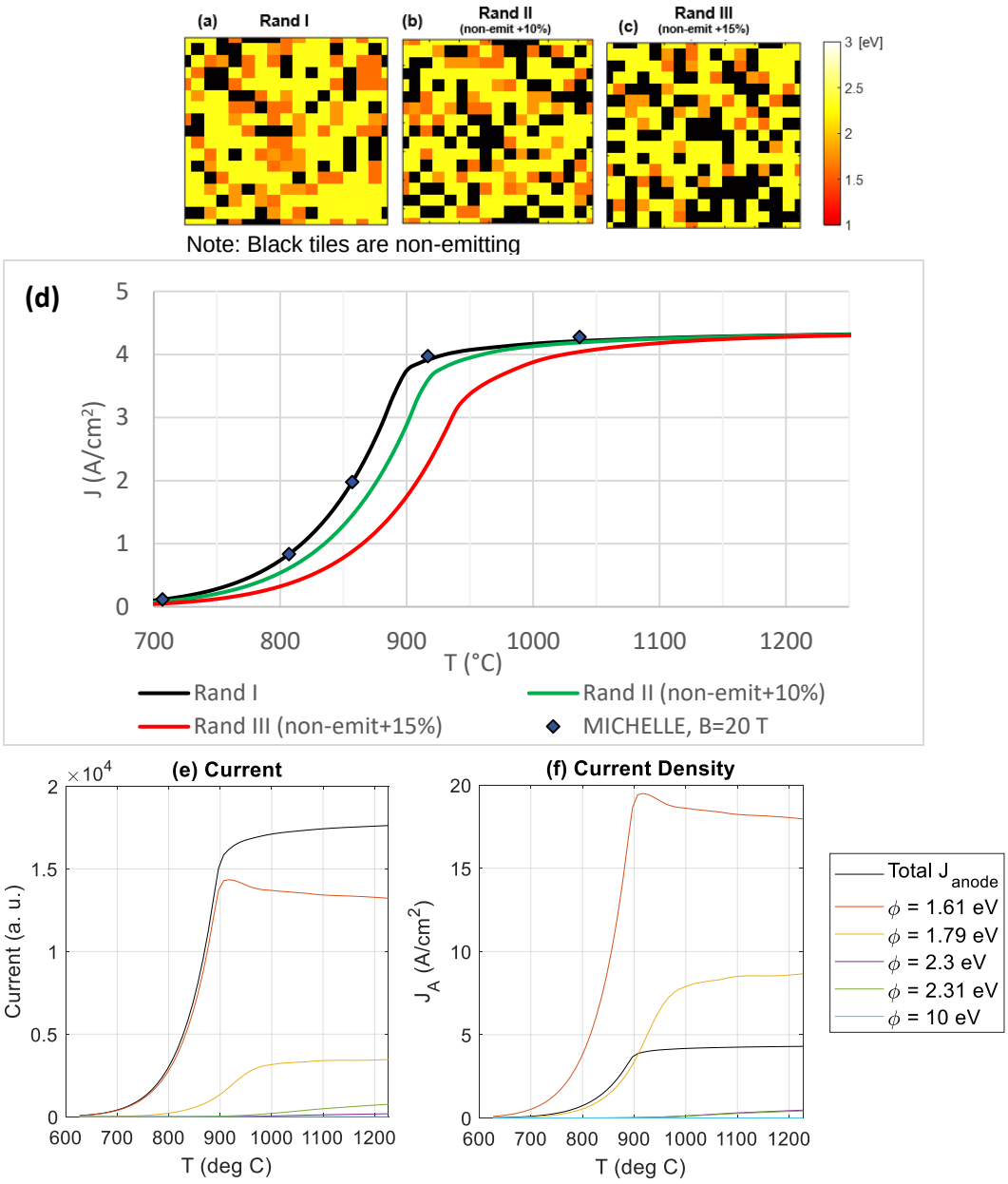

Figure 4.8: (a,b,c) Randomly generated work function maps using distributions Rand I, II, and III from Table 4.1 (d) Miram curves of Rand I, II, and III where the non-emitting area is increased by 10% in Rand II and by 15% in Rand II while the 1.61eV area is decreased to compensate. The MICHELLE simulation results for Rand I using a 20 T B_z field are included, showing excellent agreement with analytic theory (e) Anode current and (f) anode current density for entire cathode(black curve) and from different work function regions (color curves).

each tile. Excellent agreement between the two was observed in Fig. 4.8d for all temperature of interest. MICHELLE simulations of Rand I with $B = 0$ shows an increase of anode current by

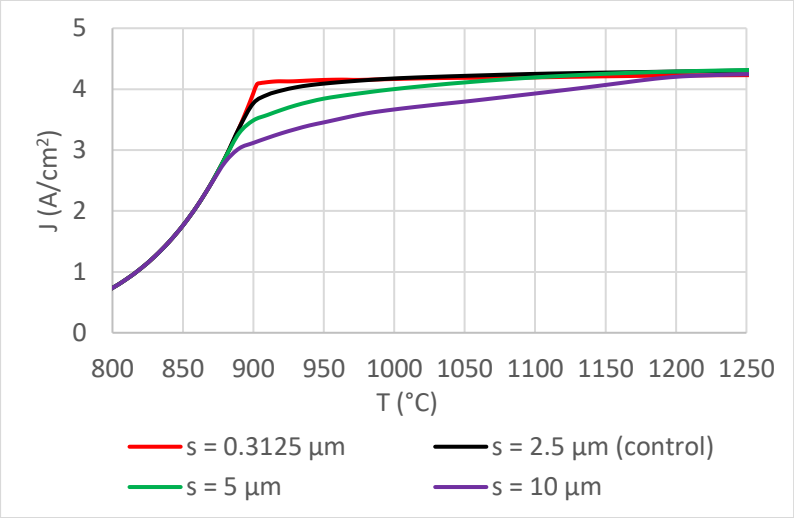

Figure 4.9: Effect of varying work function tile size *s* on shape of Miram curve using work function map Rand I.

only 2.4 percent at the knee, compared with the MICHELLE run using $B = 20$ T (Figure 4.8d) and consistent with our previous observation [70] that the electron motion parallel to the cathode surface has little effect on the shape of the Miram curves. We also show the contribution of current (Figure 4.8e) and current density (Figure 4.8f) from each work function region for Rand I. Remarkably, the 1.61eV region accounts for over 85% of the current contribution in the knee despite only making up ~18% of the actual cathode surface; the current density ascribed to this region is nearly 5 times the 1D Child-Langmuir current.

Next, we use the work function map Rand I (Figure 4.8a) and vary the width of each work function square from $s = 0.3125$µm to 10µm, plotting the resulting Miram curves in Figure 4.9. We observe that as s decreases, the knee grows dramatically sharper. As in the checkered cases, (Figure 4.5 & Figure 4.7) smaller tile sizes imply a greater proportion of boundaries relative to surface area. Since the current compensation effect occurs primarily at the boundaries, one would expect this effect to become progressively stronger as the tile size decreases. This phenomenon have some implications on cathode design; if the length scale of work function

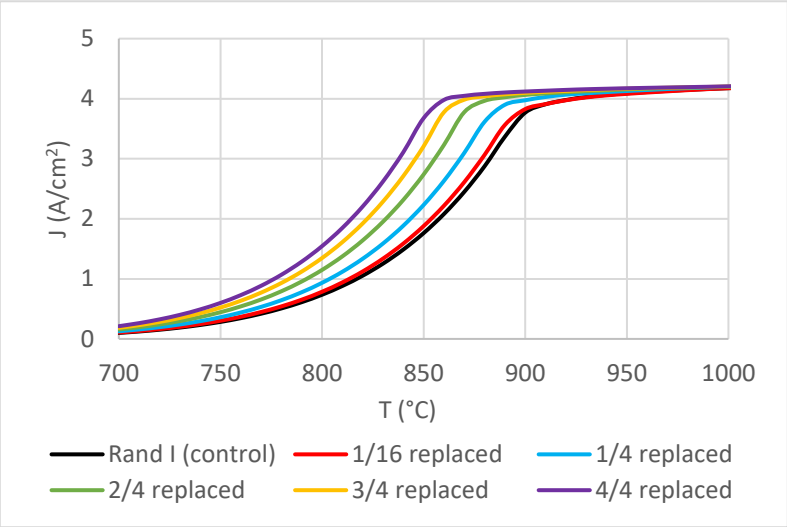

Figure 4.11: Simulation of work function map Rand I, with increasing fraction of non-emitting (10eV) tiles replaced by the highly emitting 1.61eV tiles.

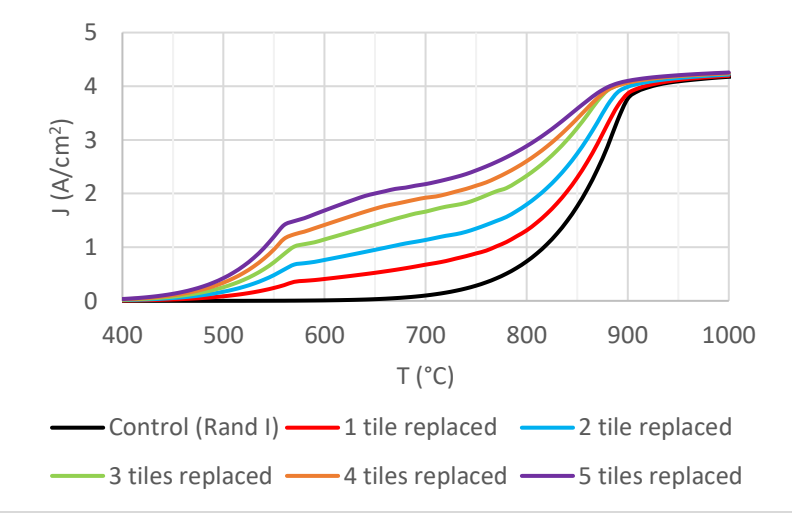

Figure 4.10: Simulation of work function map Rand I with increasing number of non-emitting (10eV) tiles, replaced by very highly emitting 1.0 eV tiles.

variations can be reduced, one could obtain a higher anode current density for a lower cathode temperature, thereby improving lifetime and performance [3].

We next perform two additional tests, on the gradual reduction of non-emitting regions (Figure 4.11), and on the effects of some local "hot spots", modelled by very low work functions so that the local emission current density may be excessively high (Figure 4.10). In Figure 4.11, we replace the non-emitting tiles in Rand I (Figure 4.8a) with 1.61eV tiles in increasing

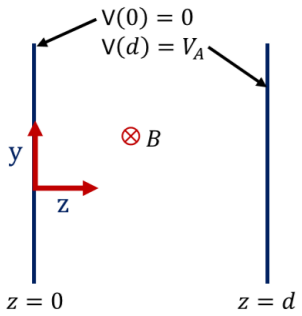

Figure 4.12: Planar crossed field diode geometry.

fractions: 1/16, 1/4, 1/2, 1. As one might expect, as the number of low work function tiles increase, the transition temperature between space-charge-limited and temperature-limited flow drops and the knee sharpens as the overall curve shifts to the left. The second test also used Rand I, where we replaced an increasing number of 10 eV work function tiles (which are non-emitting) with 1 eV work function tiles (which are highly emitting). The result is shown in Figure 4.10. Comparison of the lowest two curves in Figure 4.10 shows that just one tile of excessively low work function (of 1 eV) can have a rather significant modification of the Miram curve. Both Figure 4.11 and Figure 4.10 use tile sizes $s = 2.5$ μm. We are tempted to use such a highly emitting local spot to represent strong field emission resulted from a local cathode surface roughness that is difficult to model, either analytically or in numerical codes. These local hot spots could increase the intrinsic emittance of the generated electron beam [111], [112].

4.4 Thermionic emission for crossed field flow

Next we consider thermionic emission in a crossed-field diode, in which an external magnetic field is applied orthogonal to the vacuum electric field, i.e. parallel to the cathode surface (See Figure 4.12). Conventional magnetrons used in all domestic microwave ovens are prime examples of crossed-field devices that use thermionic cathodes. We remark that the analytic solution for a thermionic cathode in crossed fields, similar to those of Fry [31] and Langmuir [29] including a careful analysis of the electron sheath that results from an initial

Maxwellian velcoity distribution of electrons, has never been published until our recent paper by Chernin et al. [75]. The nature of the solutions would shed light onto other high power microwave devices including relativistic magnetrons [3], magnetically insulated line oscillators (MILOs) [59], as well as pulsed power devices such as the linear transformer driver (LTD) [60]. The current at the anode then depends not only on the density of space charge in the gap (as in the previous section) but also the magnetic field, which curves the trajectory of emitted electrons, causing them to potentially miss the anode and return to the cathode. For a non-relativistic electron emitted with zero velocity, at the critical magnetic field $B = B_H = \sqrt{\frac{2mV_A}{ed^2}}$, called the Hull cutoff [113], this electron barely misses the anode. For a realistic diode with a range of electron emission energies, we would then expect that the current collected at the anode quickly approaches zero as B approaches and exceeds B_H. For $B > B_H$, the crossed-field diode is said to be magnetically insulated.

The theoretical analysis of current transport in a crossed-field diode is rather subtle and is typically performed assuming that all electrons have some mono-energetic emission velocity or furthermore, that the electric field on the cathode surface is zero [53], [114]–[117]. These assumptions allow simultaneous, steady state solutions to the Poisson equation, the force law and the continuity equations. However, as indicated above, there has been no previous theory describing the crossed-field diode current for a Maxwellian electron distribution, similar to that of Fry [31], Langmuir [29], and the work in the previous section. In this section, we present details of simulation results which will be compared with the novel theory of crossed-field electron flow for a thermal distribution, in which the space charge effect is solved self-consistently with the orbital motion of the electrons [75]. While we will not describe the theory itself in any great detail in this chapter, we will show how key results from this theory, which

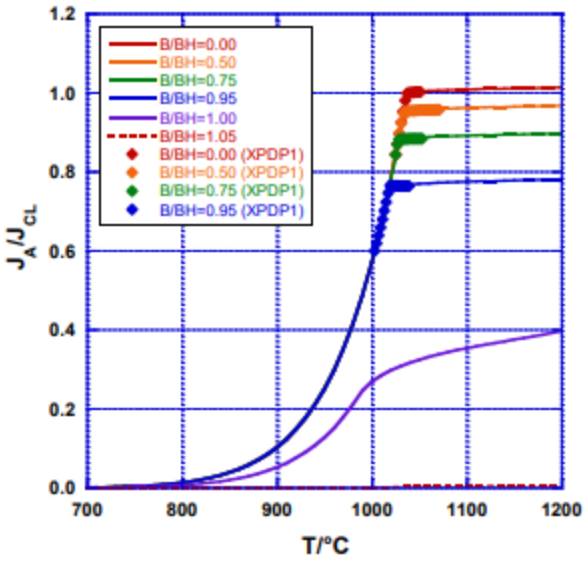

Figure 4.13: Miram curves for various values of a magnetic field B/B_H applied orthogonal to the electric field. Solid lines are from numerical solution of the theory in [91] and solid diamond points are results of particle-in-cell simulations in XPDP1.

assumes steady state cycloidal electron orbits consistent with initial Maxwellian velocity distributions, were validated through the use of particle-in-cell (PIC) simulations in XPDP1 [118]. As we shall see, the PIC simulations always show breakdown of the initially laminar cycloidal flow into a turbulent shear flow when B approaches and exceeds B_H, preventing meaningful comparison between the analytic theory and PIC for those values of magnetic field. The analytic theory was due to Chernin, while the author did the PIC simulations.

The theory of planar crossed-field flow [75] generally follows a similar procedure as the one undertaken in [70] and in the previous section, albeit with significant complications due to the orbital motion of the electrons even with the assumption of a uniform emission at the cathode surface, i.e. no spatial work function variations. The charge density and potential are assumed to depend only on z, while the electrons may move in both y and z. A solution to Vlasov's equation may be determined in terms of the total energy of an electron $E = \frac{1}{2}mv_y^2 + \frac{1}{2}mv_z^2 + qV(z)$, which is a constant of motion. The charge density ρ as well as the limits of its integration over

velocity space (cf. Eq. 4.7) may then be calculated through the use of an effective potential that accounts for particle reflection due to the reversed electric field due to space charge and/or the influence of the magnetic field. Poisson's equation is then solved numerically (using the iterative method similar to the one described in the previous section and [70]) and the current density at the anode may be obtained.

We use the same diode parameters as in the previous section, with $V_A = 179.5$ V and $d = 0.381$ mm. The work function is fixed at $\phi = 2$ eV. We may then generate the Miram curves in Figure 4.13 for various values of B normalized to the Hull cutoff, which for our parameters is $B_H = 0.1186$ T. The anode current is normalized to the Child-Langmuir current density with the finite temperature correction introduced by Langmuir [29] [Eq. (4.2b)]. For $B < B_H$, we find that all the Miram curves have sharp knees, due to the onset of space-charge effects for a cathode with a uniform work function. As the magnetic field is increased from zero to just below B_H, the maximum current drops as an increasing number of electrons are turned away from the anode due to the magnetic field. Just above the Hull cutoff B/B_H =1.05, the current drops to nearly zero (Figure 4.13). Note that we use the expression for the Hull cutoff that assumes zero electron emission velocity, as opposed to a Maxwellian distribution, so B/B_H must be slightly larger than 1 for the complete cutoff of anode current.

We have used the PIC code XPDP1 [118] to study electron transport in the gap as B increases from 0 to beyond B_H. XPDP1 is an electrostatic, nonrelativistic code that solves Poisson's equation in 1D but records electron motion in all three dimensions of velocity space. In these simulations, the electrons are emitted with a Maxwellian distribution with temperature T and the emission current density is set to be equal to the Richardson-Dushman law (Eq. 4.1) evaluated at T with a work function ϕ =2 eV . The simulation results for B/B_H =0, 0.5, 0.75,

0.95, represented by the diamond data points in Figure 4.13 agree extremely well with the analytic theory, even in the most demanding 'knee' region where the transition between temperature-limited and space-charge limited flow occurs.

However, for B/B_H =1, 1.05, the simulations show that the initially laminar electron flow (which remained stable for $B < B_H$) breaks down into a turbulent state, even at very low temperatures, at which the Richardson-Dushman current density is only a small fraction of the Child-Langmuir value. For $B > B_H$, this turbulent state is in the form of a turbulent shear flow, due to an accumulation of space charge, caused by electrons with a low emission velocity that failed to return to the cathode surface. These observations are consistent with previous PIC studies, where turbulent shear flows (also known as Brillouin flows [55]) always formed from initially laminar cycloidal orbits if there is a small AC voltage perturbation [119] or a small stray resistance [57], or a small misalignment of the magnetic field [120]. This turbulent shear flow is also formed in a crossed-field diode (with $B > B_H$) when the injection current exceeds some critical value [114]. For thermal emission studied here, however, no threshold emission current was found by the author.

To investigate this transition into turbulence for thermionic cathodes, we additionally performed a series of high fidelity PIC simulations, beyond those reported in our paper [75]. Here, we test three temperatures T =850, 950, 1000°C and two magnetic fields B/B_H =2,5. These simulations used 10,000 spatial steps in z ($\Delta z = 38.1$ nm) with time steps of $\Delta t = 0.02$ ps. The particle weighting parameter nc2p (the ratio of real particles to computer particles) differed from run to run but varied between 1×10^3 to 5×10^3, maintaining the number of computer particles on the order of 10^6. Figure 4.14 shows the electric field at the cathode (normalized to the magnitude of the electric field) rises before "stabilizing" at some final value that may be

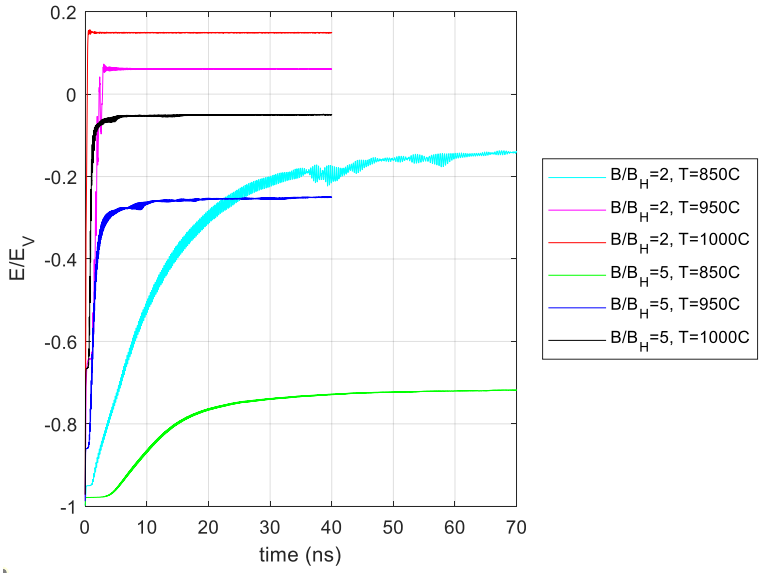

Figure 4.14: Electric field at the cathode normalized to vacuum electric field.

either positive or negative. Higher magnetic fields and lower cathode temperatures are in general correlated with longer "stabilization times" and a lower final electric field. Note that a Brillouin hub is formed in all cases, so some turbulent oscillatory behaviour is always observed, even at the final time. We demonstrate in Figure 4.15 the turbulent state for each case at the final time ($t_{final} = 70$ ns for $T = 850$°C , $t_{final} = 40$ ns for $T = 950$°C, 1000°C) in phase space plots of v_z vs z. To illustrate the breakdown from laminar flow into turbulence, we show in Figure 4.16 the temporal evolution in v_z vs z phase space for the $B/B_H = 2,\ T = 950$°C case. To investigate the possibility that high magnetic fields could suppress turbulence, we additionally tested an even higher magnetic field $B/B_H = 10$ (this was the reason for such a high fidelity simulation, to be able to adequately resolve the Brillouin hub height $h = D\left[1 - \sqrt{1 - \frac{B_H}{B}}\right] \approx 2$ μm at this magnetic field). However, this only increased the formation time for the instability, but did not prevent it.

As a caveat, we note that this breakdown into turbulence may have originated as a numerical instability due to the inherent limitations of the PIC model, particularly in light of the

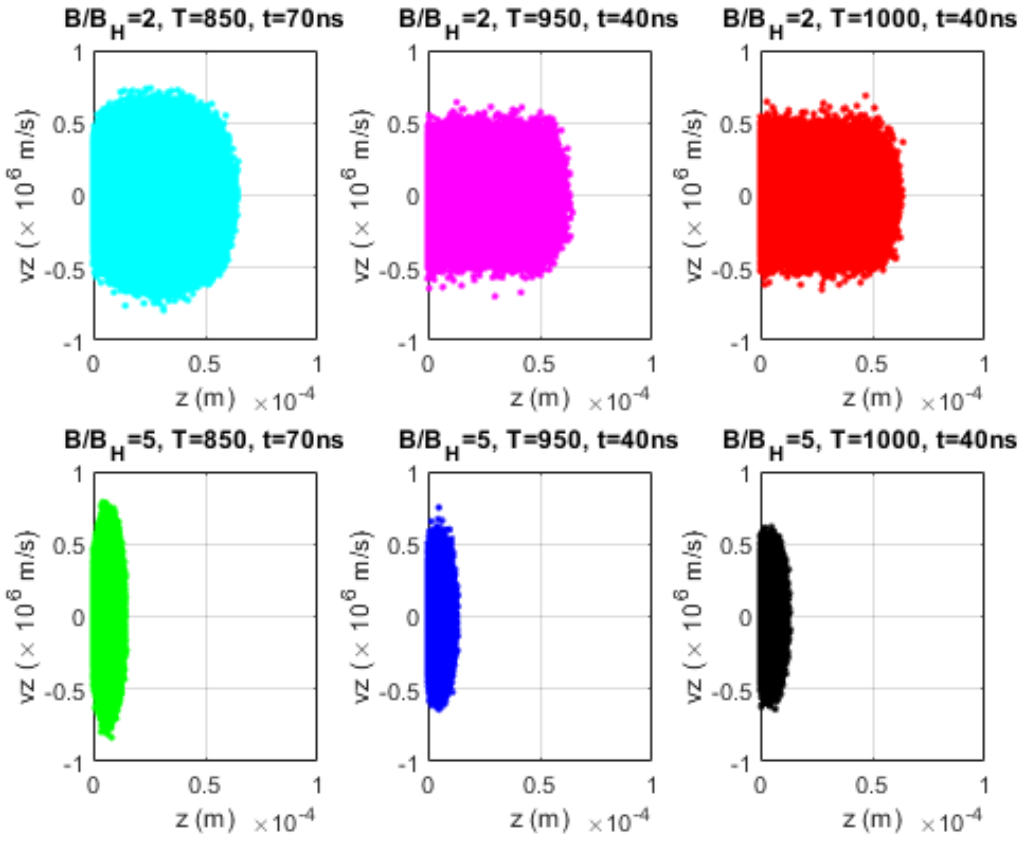

Figure 4.15: Phase space plots at the "final time" showing that all tests conducted above the Hull cutoff result in a turbulent Brillouin hub.

high discretization in space and time. However, this study is yet another among many [57], [114], [116], [121] that support the notion [53], [57], [122] that Brillouin flow, not laminar cycloidal flow is the preferred state for a magnetically insulated ($B > B_H$) diode. This is an important matter, since these two different modes yield very different results for the Buneman-Hartree (wave-particle synchronism) condition for a cylindrical magnetron [55]. Nevertheless, it is apparent that the cycloidal flow state is highly unstable, and any real crossed field device has a number of destabilizing effects that would certainly perturb this state and cause it to devolve into the preferred Brillouin flow state.

Finally, we remark that in both magnetically insulated line oscillators [59], as well as pulsed power devices such as the linear transformer driver [60], there is a region that marks the

transition from non-magnetically insulated to magnetically insulated operation. Further studies of these transitions, in the region $B/B_H \approx 1$ such as those displayed in Figure 4.13, are greatly desired.

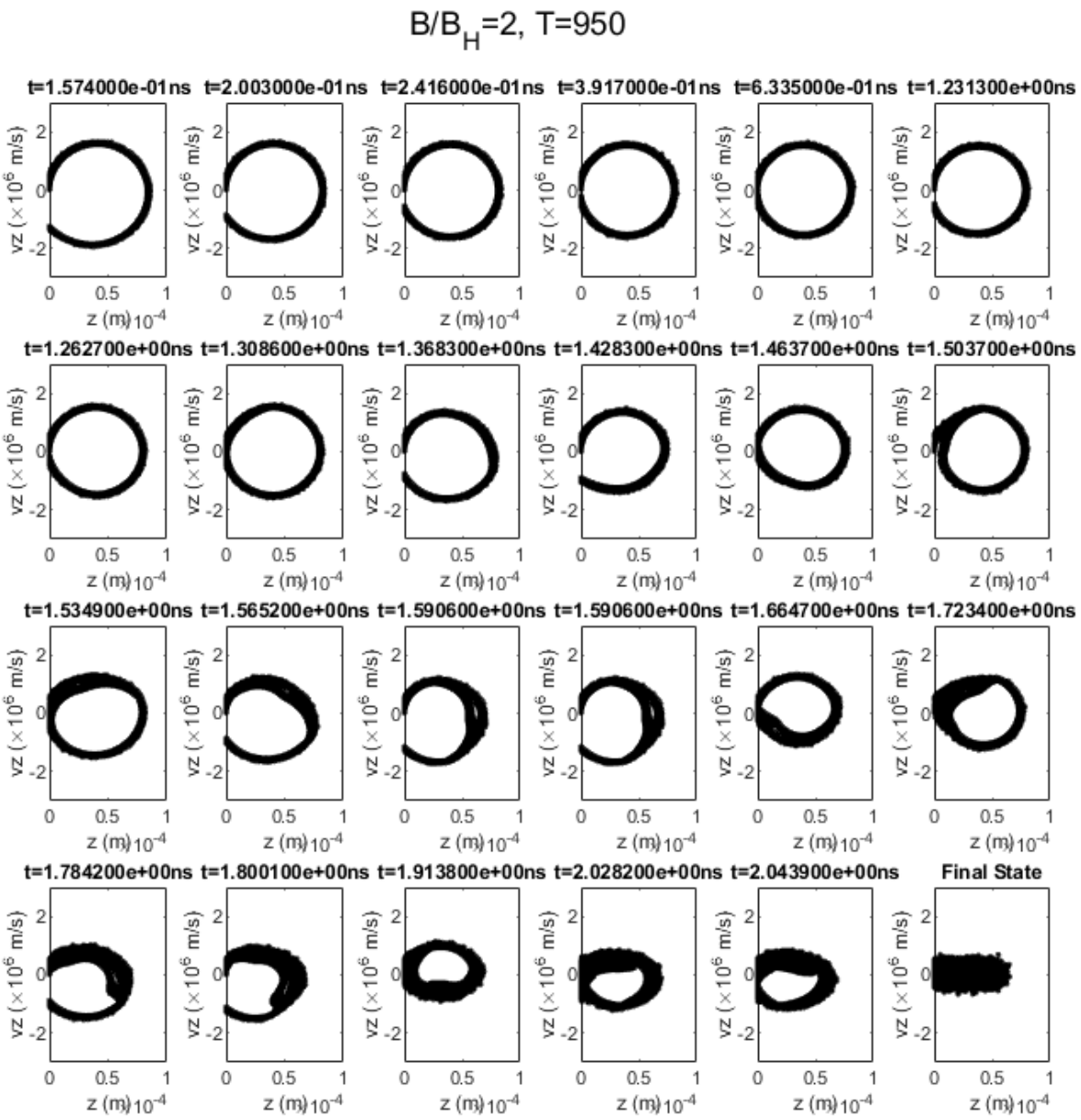

Figure 4.16: Temporal evolution of v_z vs z phase space showing collapse of cycloidal flow into turbulence for the case B/B_H = 2, T = 950°C.

4.5 Conclusions

In this chapter, we have described an analytic formulation for thermionic emission in a diode that includes space charge effects and used it to model work function variations along the two dimensions on a cathode, describing their effects on the shape of the Miram curve [74]. We have observed that that inclusion of 2D variations in the work function yields a Miram curve that is notably more rounded than its 1D counterpart [70], and is therefore closer to experimental Miram curves. From a number of 2D work function patterns, we recovered the 1D Child-Langmuir space-charge-limited current as if the entire cathode were emitting despite the sizable portion of the area being non-emitting. It remains an intriguing mystery why patch cathode emission, in either the 1D or 2D model, conspires to yield an anode current that is governed by the 1D Child-Langmuir law, as if the entire cathode were emitting. We also illustrate how the low work function regions contribute the most current despite making up a relatively small fraction of the cathode area. In addition, we examine how the size of the patchiness in the work function affects the shape of the Miram curve. In general, smaller length scales yield a sharper knee and hence improved cathode performance. A simple model also suggests that a single highly emitting local spot may produce a noticeable modification of the Miram curve.

However, these studies of a 2D work function distribution imply tremendous difficulty to solve the inverse problem: calculating the work function distribution from experimental Miram curves. Since the emission from a specific location on the cathode surface is highly dependent on the neighboring work function distribution as well as the patchiness length scales, and on whether there are some highly emitting local hot spots, the Miram curve is unlikely to deconvolve into its constituent work function distribution.

Furthermore, we have described an extension of this theory into crossed-field geometries [75], where a magnetic field is applied parallel to the cathode surface albeit with a uniform cathode. Unlike any theories preceding it, this model describes electron emission with a Maxwellian velocity distribution. We have shown that the anode current sharply drops as the applied magnetic field approaches the Hull cutoff. Using the PIC code XPDP1, we have validated this theory below the Hull cutoff; however, these simulations show that the initially laminar cycloidal orbits break down into a turbulent Brillouin flow above the Hull cutoff, even at very low cathode temperatures. The transition region $B \approx B_H$ requires further study.

Chapter 5 Summary and Future Work

5.1 Summary

In this thesis, we made several extensions to the classical theory of traveling wave tubes (TWTs), mainly to model various realistic effects which were not studied previously, whose importance has surfaced in recent years.

In Chapter 2, we showed how the effects of realistic circuit loss could be incorporated into the recently formulated exact hot-tube dispersion for a practical tape helix TWT. This is an important modification to the classical TWT theory of Pierce. We found that the exact and classical Pierce theories only agreed well in a restricted frequency range. This discrepancy arose from the effects of higher order circuit modes and their space harmonics, which modify all of Pierce's TWT parameters, including the introduction of a new space charge parameter q, which accounts for the detune of the circuit mode, and which was absent in Pierce's original theory.

In Chapter 3, we described the phenomenon of backward wave oscillation (BWO) and the threshold conditions required for its onset, which may disrupt the operation of TWTs. We extended the classical theory of Johnson to separately include the effects of random manufacturing errors and end reflections. We found that the threshold conditions were relatively insensitive to random variations in circuit phase velocity; and thus, similarly, insensitive to the space charge parameter, q. The explanation for this surprising result is that q mainly affects the phase relation, and therefore it primarily modifies the oscillation frequency at the onset of BWO. The BWO oscillation frequency drops with increased q, leaving the threshold beam current essentially unchanged. However, we did find that the threshold beam current depends sensitively

on the phase and magnitude of the composite reflection coefficient. In the idealized case of zero space charge, zero cold circuit loss case, we showed that on average, the starting current is decreased due to the effect of reflections. Proprietary and other constraints prevented comparison of the theory with experiments.

In Chapter 4, we described an analytic formulation for thermal emission from a cathode that solves the Vlasov and Poisson equations in 3D under the assumption of an infinite focusing magnetic field. We showed that 2D variations in the work function at the cathode surface could produce rounded Miram curves more readily than its 1D counterpart, a significant step towards understanding and replicating the experimental Miram curves from a theoretical model. The Miram curve is a plot of the anode current vs the cathode temperature T in a thermionic cathode; it has been a mystery for decades regarding why and how it exhibits a smooth, rounded knee that marked the transition from the temperature limited to the space charge limited regime as T increases. We showed how the phenomenon of patchy cathode emission, including significant non-emitting areas, can contribute to a rounded knee. It also allows low work function regions to locally exceed the 1D Child-Langmuir current density, compensating for their weakly emitting or non-emitting neighbors. This addresses how a cathode may be overall governed by the 1D Child-Langmuir law despite a large fraction of the cathode surface being non-emitting. We also demonstrated that smaller length scales of work function variations are correlated with a sharper knee, improving cathode performance. Furthermore, we described an extension of the thermal emission model into the crossed-field case and presented particle-in-cell simulations that validated its results at a low magnetic field, below the Hull cutoff. Above the Hull cutoff, we demonstrated that the laminar cycloidal orbits of the theory are unstable and always break down into a turbulent shear flow (turbulent Brillouin flow) for a Maxwellian electron distribution, even

at a low cathode temperature at which the emitted current density is significantly below the Child-Langmuir value.

5.2 Future Work

There are several possible avenues for advancing or clarifying some of the results of this thesis. Regarding the exact hot-tube dispersion relation, we note that when the beam voltage exceeds ~10kV, a relativistic formulation is needed to accurately determine the beam velocity, and hence the detune factor, for the dispersion relation. Neglecting these effects may result in errors comparable to or exceeding than the detuning effect of q. The role of q in alternate TWT geometries or other vacuum electronic devices remains to be seen. In fact, there has been an intense discussion in the TWT community how to properly include q in existing simulation codes. It is also unknown how q is modified if one takes into account the scalloping motion of the electron orbits. On backward wave oscillations, the exact theory for BWO in a tape helix TWT has not yet been obtained. The aforementioned exact TWT dispersion relation was obtained only for the forward wave branch. Similar attempts on the BWO branch have failed for reasons not yet understood. Some theoretical analysis may be required to compare our approach to that of Levush et al, which differs significantly. Furthermore our extensions to Johnson's theory were not able to identify why an L3 TWT was not able to oscillate, despite meeting Johnson's criteria. The recent work on thermionic cathodes (presented in Chapter 4 and in [70]) represents a significant advance in understanding the factors that contribute to the shape of the Miram curve. This area is fertile ground for a variety of extensions to include, for example, patch field effects [107], [108], the role of field emission and of surface roughness, etc. Although our results indicate significant difficulty in determining the work function distribution from an experimental Miram curve, further work is required to assess the viability of such an approach,

which has been popular in the community but without a convincing physical basis. Finally, concerning crossed-field flows, we note that the transition across the Hull cutoff requires further study; this is crucial in important high power crossed-field devices such as magnetically insulated line oscillators (MILOs) and linear transformer drivers (LTDs), which exhibit such a transition. Additionally the role of secondary electron emission and its contribution to space charge effects might also be considered.

Bibliography

[1] R. J. Barker, J. H. Booske, N. C. Luhmann Jr., and G. S. Nusinovich, *Modern Microwave and Millimeter-Wave Power Electronics*. Wiley-IEEE Press, 2005.

[2] S. E. Tsimring, *Electron Beams and Microwave Vacuum Electronics*. John Wiley & Sons, Ltd, 2006.

[3] A. S. Gilmour, *Klystrons, Traveling Wave Tubes, Magnetrons, Crossed-field Amplifiers, and Gyrotrons*. Artech House, 2011.

[4] C. M. Armstrong, "The quest for the ultimate vacuum tube," *IEEE Spectr.*, vol. 52, no. 12, pp. 28–51, Dec. 2015, doi: 10.1109/MSPEC.2015.7335797.

[5] A. V. Haeff, "Device for and method of controlling high frequency currents," US2064469A, Dec. 15, 1936.

[6] A. V. Haeff, "Device for and method of controlling high frequency currents," US2233126A, Feb. 25, 1941.

[7] N. E. Lindenblad, "Electron discharge device system," US2300052A, Oct. 27, 1942.

[8] R. Kompfner, "The Traveling-Wave Tube as Amplifier at Microwaves," *Proc. IRE*, vol. 35, no. 2, pp. 124–127, Feb. 1947, doi: 10.1109/JRPROC.1947.231238.

[9] R. Kompfner, "The invention of traveling wave tubes," *IEEE Trans. Electron Devices*, vol. 23, no. 7, pp. 730–738, Jul. 1976, doi: 10.1109/T-ED.1976.18477.

[10] J. Copeland and A. A. Haeff, "The true history of the traveling wave tube," *IEEE Spectr.*, vol. 52, no. 9, pp. 38–43, Sep. 2015, doi: 10.1109/MSPEC.2015.7226611.

[11] J. R. Pierce, "Theory of the Beam-Type Traveling-Wave Tube," *Proc. IRE*, vol. 35, no. 2, pp. 111–123, Feb. 1947, doi: 10.1109/JRPROC.1947.226217.

[12] J. R. Pierce, *Traveling-Wave Tubes*. New York, NY, USA: Van Nostrand, 1950.

[13] J. W. Gewartowski and H. A. Watson, *Principles of Electron Tubes: including Grid-controlled Tubes, Microwave Tubes, and Gas Tubes*. New York, NY, USA: Van Nostrand, 1965.

[14] Z. Huang and K.-J. Kim, "Review of x-ray free-electron laser theory," *Phys. Rev. Spec. Top. - Accel. Beams*, vol. 10, no. 3, p. 034801, Mar. 2007, doi: 10.1103/PhysRevSTAB.10.034801.

[15] V. Kumar and K.-J. Kim, "Analysis of Smith-Purcell free-electron lasers," *Phys. Rev. E Stat. Nonlin. Soft Matter Phys.*, vol. 73, no. 2 Pt 2, p. 026501, Feb. 2006, doi: 10.1103/PhysRevE.73.026501.

[16] B. E. Carlsten, "Axial free-electron laser interaction between an annular electron beam and an axisymmetric TM mode," *IEEE J. Quantum Electron.*, vol. 31, no. 10, pp. 1753–1763, Oct. 1995, doi: 10.1109/3.466049.

[17] H. P. Freund, *Principles of Free-Electron Lasers*. Springer Netherlands, 1992.

[18] C. W. Roberson and P. Sprangle, "A review of free-electron lasers," *Phys. Fluids B Plasma Phys.*, vol. 1, no. 1, pp. 3–42, Jan. 1989, doi: 10.1063/1.859102.

[19] T. C. Marshall, *Free-electron Lasers*. Macmillan Publishing Company, 1985.

[20] P. Zhang, L. K. Ang, and A. Gover, “Enhancement of coherent Smith-Purcell radiation at terahertz frequency by optimized grating, prebunched beams, and open cavity,” *Phys. Rev. Spec. Top. - Accel. Beams*, vol. 18, no. 2, p. 020702, Feb. 2015, doi: 10.1103/PhysRevSTAB.18.020702.
[21] M. Thumm, “State-of-the-Art of High-Power Gyro-Devices and Free Electron Masers,” *J. Infrared Millim. Terahertz Waves*, vol. 41, no. 1, pp. 1–140, Jan. 2020, doi: 10.1007/s10762-019-00631-y.
[22] K. R. Chu, “The electron cyclotron maser,” *Rev. Mod. Phys.*, vol. 76, no. 2, pp. 489–540, May 2004, doi: 10.1103/RevModPhys.76.489.
[23] Y. Y. Lau, K. R. Chu, L. R. Barnett, and V. L. Granatstein, “Gyrotron travelling wave amplifier: I. Analysis of oscillations,” *Int. J. Infrared Millim. Waves*, vol. 2, no. 3, pp. 373–393, May 1981, doi: 10.1007/BF01007408.
[24] Y. Y. Lau, “Simple macroscopic theory of cyclotron maser instabilities,” *IEEE Trans. Electron Devices*, vol. 29, no. 2, pp. 320–335, Feb. 1982, doi: 10.1109/T-ED.1982.20703.
[25] “Traveling-wave tube | electronics,” *Encyclopedia Britannica*. https://www.britannica.com/technology/traveling-wave-tube (accessed Dec. 15, 2020).
[26] O. W. Richardson, *The Emission of Electricity from Hot Bodies*. London, U. K.: Longmans, Green and Company, 1916.
[27] S. Dushman, “Electron Emission from Metals as a Function of Temperature,” *Phys. Rev.*, vol. 21, no. 6, pp. 623–636, Jun. 1923, doi: 10.1103/PhysRev.21.623.
[28] C. D. Child, “Discharge From Hot CaO,” *Phys. Rev. Ser. I*, vol. 32, no. 5, pp. 492–511, May 1911, doi: 10.1103/PhysRevSeriesI.32.492.
[29] I. Langmuir, “The Effect of Space Charge and Initial Velocities on the Potential Distribution and Thermionic Current between Parallel Plane Electrodes,” *Phys. Rev.*, vol. 21, no. 4, pp. 419–435, Apr. 1923, doi: 10.1103/PhysRev.21.419.
[30] P. Zhang, A. Valfells, L. K. Ang, J. W. Luginsland, and Y. Y. Lau, “100 years of the physics of diodes,” *Appl. Phys. Rev.*, vol. 4, no. 1, p. 011304, Mar. 2017, doi: 10.1063/1.4978231.
[31] T. C. Fry, “The Thermionic Current between Parallel Plane Electrodes; Velocities of Emission Distributed According to Maxwell’s Law,” *Phys. Rev.*, vol. 17, no. 4, pp. 441–452, Apr. 1921, doi: 10.1103/PhysRev.17.441.
[32] R. J. Umstattd, C. G. Carr, C. L. Frenzen, J. W. Luginsland, and Y. Y. Lau, “A simple physical derivation of Child–Langmuir space-charge-limited emission using vacuum capacitance,” *Am. J. Phys.*, vol. 73, no. 2, pp. 160–163, Jan. 2005, doi: 10.1119/1.1781664.
[33] P. M. Bellan, *Fundamentals of Plasma Physics*. Cambridge: Cambridge University Press, 2006.
[34] C. K. Birdsall and T. E. Everhart, “Modified contra-wound helix circuits for high-power traveling-wave tubes,” *IRE Trans. Electron Devices*, vol. 3, no. 4, pp. 190–204, Oct. 1956, doi: 10.1109/T-ED.1956.14187.
[35] C. C. Motta, “A Large-Signal Analysis of a Ring-Bar TWT,” in *2007 IEEE 34th International Conference on Plasma Science (ICOPS)*, Jun. 2007, pp. 875–875, doi: 10.1109/PPPS.2007.4346181.
[36] J. R. M. Vaughan, “Calculation of coupled-cavity TWT performance,” *IEEE Trans. Electron Devices*, vol. 22, no. 10, pp. 880–890, Oct. 1975, doi: 10.1109/T-ED.1975.18237.

[37] C. F. Dong, P. Zhang, D. Chernin, Y. Y. Lau, B. W. Hoff, D. H. Simon, P. Wong, G. B. Greening, and R. M. Gilgenbach, "Harmonic Content in the Beam Current in a Traveling-Wave Tube," *IEEE Trans. Electron Devices*, vol. 62, no. 12, pp. 4285–4292, Dec. 2015, doi: 10.1109/TED.2015.2490584.
[38] P. Y. Wong, Y. Y. Lau, D. Chernin, B. W. Hoff, and R. M. Gilgenbach, "Origin of Second-Harmonic Signals in Octave Bandwidth Traveling-Wave Tubes," *IEEE Trans. Electron Devices*, vol. 65, no. 2, pp. 710–715, Feb. 2018, doi: 10.1109/TED.2017.2785284.
[39] D. Shiffler, J. Luginsland, D. M. French, and J. Watrous, "A Cerenkov-like Maser Based on a Metamaterial Structure," *IEEE Trans. Plasma Sci.*, vol. 38, no. 6, pp. 1462–1465, Jun. 2010, doi: 10.1109/TPS.2010.2046914.
[40] Y. S. Tan and R. Seviour, "Wave energy amplification in a metamaterial-based traveling-wave structure," *EPL Europhys. Lett.*, vol. 87, no. 3, p. 34005, Aug. 2009, doi: 10.1209/0295-5075/87/34005.
[41] Y. Y. Lau and D. Chernin, "A review of the ac space-charge effect in electron–circuit interactions," *Phys. Fluids B Plasma Phys.*, vol. 4, no. 11, pp. 3473–3497, Nov. 1992, doi: 10.1063/1.860356.
[42] G. M. Branch and T. G. Mihran, "Plasma frequency reduction factors in electron beams," *IRE Trans. Electron Devices*, vol. 2, no. 2, pp. 3–11, Apr. 1955, doi: 10.1109/T-ED.1955.14065.
[43] S. K. Datta and L. Kumar, "A Simple Closed-Form Formula for Plasma-Frequency Reduction Factor for a Solid Cylindrical Electron Beam," *IEEE Trans. Electron Devices*, vol. 56, no. 6, pp. 1344–1346, Jun. 2009, doi: 10.1109/TED.2009.2017649.
[44] T. M. Antonsen and B. Levush, "Traveling-wave tube devices with nonlinear dielectric elements," *IEEE Trans. Plasma Sci.*, vol. 26, no. 3, pp. 774–786, Jun. 1998, doi: 10.1109/27.700830.
[45] D. Dialetis, D. Chernin, T. M. Antonsen, and B. Levush, "An Improved Representation of AC Space-Charge Fields in Steady-State Simulation Codes for Linear-Beam Tubes," *IEEE Trans. Electron Devices*, vol. 54, no. 4, pp. 888–892, Apr. 2007, doi: 10.1109/TED.2007.891858.
[46] S. J. Cooke, Chia-Lie Chang, T. M. Antonsen, D. P. Chernin, and B. Levush, "Three-dimensional modeling of AC space charge for large-signal TWT simulation," *IEEE Trans. Electron Devices*, vol. 52, no. 5, pp. 764–773, May 2005, doi: 10.1109/TED.2005.845870.
[47] P. Y. Wong, D. Chernin, and Y. Y. Lau, "Modification of Pierce's Classical Theory of Traveling-Wave Tubes," *IEEE Electron Device Lett.*, vol. 39, no. 8, pp. 1238–1241, Aug. 2018, doi: 10.1109/LED.2018.2851544.
[48] P. Y. Wong, "A Contemporary Study in the Theory of Traveling-Wave Tubes," Ph.D. dissertation, University of Michigan, Ann Arbor, MI, USA, 2018.
[49] D. H. Simon, P. Wong, D. Chernin, Y. Y. Lau, B. Hoff, P. Zhang, C. F. Dong, and R. M. Gilgenbach, "On the evaluation of Pierce parameters C and Q in a traveling wave tube," *Phys. Plasmas*, vol. 24, no. 3, p. 033114, Mar. 2017, doi: 10.1063/1.4978474.
[50] H. R. Johnson, "Backward-Wave Oscillators," *Proc. IRE*, vol. 43, no. 6, pp. 684–697, Jun. 1955, doi: 10.1109/JRPROC.1955.278054.
[51] F. F. Chen, "Single-Particle Motions," in *Introduction to Plasma Physics and Controlled Fusion*, F. F. Chen, Ed. Cham: Springer International Publishing, 2016, pp. 19–49.

[52] Y. Y. Lau, “Theory of Crossed-Field Devices and a Comparative Study of Other Radiation Sources,” in *High-power microwave sources*, I. Alexeff and V. L. Granatstein, Eds. Norwood, MA: Boston: Artech House, 1987, pp. 309–351.
[53] J. C. Slater, *Microwave Electronics*. Van Nostrand, 1951.
[54] J. Benford, J. A. Swegle, and E. Schamiloglu, *High Power Microwaves*. CRC Press, 2015.
[55] Y. Y. Lau, J. W. Luginsland, K. L. Cartwright, D. H. Simon, W. Tang, B. W. Hoff, and R. M. Gilgenbach, “A re-examination of the Buneman–Hartree condition in a cylindrical smooth-bore relativistic magnetron,” *Phys. Plasmas*, vol. 17, no. 3, p. 033102, Mar. 2010, doi: 10.1063/1.3328804.
[56] R. M. Gilgenbach, Y. Y. Lau, H. McDowell, K. L. Cartwright, and T. A. Spencer, “Crossed Field Devices,” in *Modern Microwave and Millimeter-Wave Power Electronics*, Wiley-IEEE Press, 2005.
[57] P. J. Christenson, D. P. Chernin, A. L. Garner, and Y. Y. Lau, “Resistive destabilization of cycloidal electron flow and universality of (near-) Brillouin flow in a crossed-field gap,” *Phys. Plasmas*, vol. 3, no. 12, pp. 4455–4462, Dec. 1996, doi: 10.1063/1.872064.
[58] G. E. Dombrowski, “Simulation of magnetrons and crossed-field amplifiers,” *IEEE Trans. Electron Devices*, vol. 35, no. 11, pp. 2060–2067, Nov. 1988, doi: 10.1109/16.7428.
[59] M. C. Clark, B. M. Marder, and L. D. Bacon, “Magnetically insulated transmission line oscillator,” *Appl. Phys. Lett.*, vol. 52, no. 1, pp. 78–80, Jan. 1988, doi: 10.1063/1.99330.
[60] R. D. McBride, W. A. Stygar, M. E. Cuneo, D. B. Sinars, M. G. Mazarakis, J. J. Leckbee, M. E. Savage, B. T. Hutsel, J. D. Douglass, M. L. Kiefer, B. V. Oliver, G. R. Laity, M. R. Gomez, D. A. Yager-Elorriaga, S. G. Patel, B. M. Kovalchuk, A. A. Kim, P.- Gourdain, S. N. Bland, S. Portillo, S. C. Bott-Suzuki, F. N. Beg, Y. Maron, R. B. Spielman, D. V. Rose, D. R. Welch, J. C. Zier, J. W. Schumer, J. B. Greenly, A. M. Covington, A. M. Steiner, P. C. Campbell, S. M. Miller, J. M. Woolstrum, N. B. Ramey, A. P. Shah, B. J. Sporer, N. M. Jordan, Y. Y. Lau, and R. M. Gilgenbach, “A Primer on Pulsed Power and Linear Transformer Drivers for High Energy Density Physics Applications,” *IEEE Trans. Plasma Sci.*, vol. 46, no. 11, pp. 3928–3967, Nov. 2018, doi: 10.1109/TPS.2018.2870099.
[61] D. Chernin, T. M. Antonsen, B. Levush, and D. R. Whaley, “A three-dimensional multifrequency large signal model for helix traveling wave tubes,” *IEEE Trans. Electron Devices*, vol. 48, no. 1, pp. 3–11, Jan. 2001, doi: 10.1109/16.892161.
[62] D. Chernin, T. M. Antonsen, and B. Levush, “Exact treatment of the dispersion and beam interaction impedance of a thin tape helix surrounded by a radially stratified dielectric,” *IEEE Trans. Electron Devices*, vol. 46, no. 7, pp. 1472–1483, Jul. 1999, doi: 10.1109/16.772493.
[63] P. Pengvanich, D. Chernin, Y. Y. Lau, J. W. Luginsland, and R. M. Gilgenbach, “Effect of Random Circuit Fabrication Errors on Small-Signal Gain and Phase in Traveling-Wave Tubes,” *IEEE Trans. Electron Devices*, vol. 55, no. 3, pp. 916–924, Mar. 2008, doi: 10.1109/TED.2007.914840.
[64] P. Pengvanich, D. Chernin, Yue Ying Lau, J. W. Luginsland, and R. M. Gilgenbach, “Effect of random circuit fabrication errors on small signal gain and phase in traveling wave tubes,” in *2008 IEEE International Vacuum Electronics Conference*, Apr. 2008, pp. 48–49, doi: 10.1109/IVELEC.2008.4556409.
[65] S. Sengele, M. L. Barsanti, T. A. Hargreaves, C. M. Armstrong, and J. H. Booske, “Impact of random fabrication errors on backward-wave small-signal gain in traveling wave tubes

with finite space charge electron beams," *J. Appl. Phys.*, vol. 113, no. 7, p. 074905, Feb. 2013, doi: 10.1063/1.4792666.
[66] S. D'Agostino and C. Paoloni, "Helix wire tolerances in TWT small-signal gain prediction," *Microw. Opt. Technol. Lett.*, vol. 29, no. 3, pp. 208–209, 2001, doi: https://doi.org/10.1002/mop.1132.
[67] S. D'Agostino and C. Paoloni, "A study on helix pitch tolerance impact on TWT small-signal gain," *IEEE Electron Device Lett.*, vol. 23, no. 12, pp. 746–748, Dec. 2002, doi: 10.1109/LED.2002.806296.
[68] I. M. Rittersdorf, "Effects of Random Manufacturing Errors on the Performance of Contemporary Coherent Radiation Sources," Ph.D. dissertation, University of Michigan, Ann Arbor, MI, USA, 2014.
[69] M. J. Cattelino, G. V. Miram, and W. R. Ayers, "A diagnostic technique for evaluation of cathode emission performance and defects in vehicle assembly," in *1982 International Electron Devices Meeting*, Dec. 1982, pp. 36–39, doi: 10.1109/IEDM.1982.190205.
[70] D. Chernin, Y. Y. Lau, J. J. Petillo, S. Ovtchinnikov, D. Chen, A. Jassem, R. Jacobs, D. Morgan, and J. H. Booske, "Effect of Nonuniform Emission on Miram Curves," *IEEE Trans. Plasma Sci.*, vol. 48, no. 1, pp. 146–155, Jan. 2020, doi: 10.1109/TPS.2019.2959755.
[71] J. Petillo, K. Eppley, L. Chernyakova, D. Panagos, J. Burdette, E. Nelson, Xiaoling Zhai, N. Dionne, M. Cattelino, J. DeFord, K. Nguyen, B. Held, and B. Levush, "Recent advances in the MICHELLE 2D/3D electron gun and collector modeling code," in *Fifth IEEE International Vacuum Electronics Conference (IEEE Cat. No.04EX786)*, Apr. 2004, pp. 322–323, doi: 10.1109/IVELEC.2004.1316341.
[72] D. Chen, R. Jacobs, V. Vlahos, D. Morvan, and J. Booske, "Statistical Model of Non-Uniform Emission/rom Polycrystalline Tungsten Cathodes," in *2019 International Vacuum Electronics Conference (IVEC)*, Apr. 2019, pp. 1–2, doi: 10.1109/IVEC.2019.8745051.
[73] R. Jacobs, D. Morgan, and J. Booske, "Work function and surface stability of tungsten-based thermionic electron emission cathodes," *APL Mater.*, vol. 5, no. 11, p. 116105, Nov. 2017, doi: 10.1063/1.5006029.
[74] A. Jassem, D. P. Chernin, J. J. Petillo, Y. Y. Lau, A. Jensen, and S. Ovtchinnikov, "Analysis of Anode Current from a Thermionic Cathode with a Two-Dimensional Work Function Distribution," *IEEE Trans. Plasma Sci.*, in press 2020.
[75] D. Chernin, A. Jassem, and Y. Y. Lau, "Thermal Electron Flow in a Planar Crossed-Field Diode," *IEEE Trans. Plasma Sci.*, vol. 48, no. 9, pp. 3109–3114, Sep. 2020, doi: 10.1109/TPS.2020.3017715.
[76] A. Jassem, P. Y. Wong, D. P. Chernin, Y. Y. Lau, F. Antoulinakis, D. Packard, T. A. Hargreaves, and C. M. Armstrong, "Extensions of Johnson's Theory of Backward-Wave Oscillations in a Traveling-Wave Tube," *IEEE Trans. Electron Devices*, vol. 66, no. 3, pp. 1519–1524, Mar. 2019, doi: 10.1109/TED.2019.2893574.
[77] A. Jassem, Y. Y. Lau, D. P. Chernin, and P. Y. Wong, "Theory of Traveling-Wave Tube Including Space Charge Effects on the Circuit Mode and Distributed Cold Tube Loss," *IEEE Trans. Plasma Sci.*, vol. 48, no. 3, pp. 665–668, Mar. 2020, doi: 10.1109/TPS.2020.2969049.
[78] I. M. Rittersdorf, "Effects of Random Manufacturing Errors on the Performance of Contemporary Coherent Radiation Sources.," University of Michigan, 2014.

[79] T. M. Antonsen, P. Safier, D. P. Chernin, and B. Levush, “Stability of traveling-wave amplifiers with reflections,” *IEEE Trans. Plasma Sci.*, vol. 30, no. 3, pp. 1089–1107, Jun. 2002, doi: 10.1109/TPS.2002.801563.
[80] F. Antoulinakis, P. Wong, A. Jassem, and Y. Y. Lau, “Absolute instability and transient growth near the band edges of a traveling wave tube,” *Phys. Plasmas*, vol. 25, no. 7, p. 072102, Jul. 2018, doi: 10.1063/1.5028385.
[81] D. M. H. Hung, I. M. Rittersdorf, P. Zhang, D. Chernin, Y. Y. Lau, T. M. Antonsen, J. W. Luginsland, D. H. Simon, and R. M. Gilgenbach, “Absolute Instability near the Band Edge of Traveling-Wave Amplifiers,” *Phys. Rev. Lett.*, vol. 115, no. 12, p. 124801, Sep. 2015, doi: 10.1103/PhysRevLett.115.124801.
[82] R. J. Briggs, *Electron Stream Interactions with Plasmas*. Cambridge, MA: MIT Press, 1964.
[83] A. Bers, *Handbook of Plasma Physics*, Edited by M. N. Rosenbluth and R. A. Sagdeev. New York: North-Holland, 1983.
[84] L. K. Ang and Y. Y. Lau, “Absolute instability in a traveling wave tube model,” *Phys. Plasmas*, vol. 5, no. 12, pp. 4408–4410, Nov. 1998, doi: 10.1063/1.873178.
[85] A. P. Kuznetsov, S. P. Kuznetsov, A. G. Rozhnev, E. V. Blokhina, and L. V. Bulgakova, “Wave Theory of a Traveling-Wave Tube Operated Near the Cutoff,” *Radiophys. Quantum Electron.*, vol. 47, no. 5, pp. 356–373, May 2004, doi: 10.1023/B:RAQE.0000046310.29763.c1.
[86] M. A. K. Othman, M. Veysi, A. Figotin, and F. Capolino, “Giant amplification in degenerate band edge slow-wave structures interacting with an electron beam,” *Phys. Plasmas*, vol. 23, no. 3, p. 033112, Mar. 2016, doi: 10.1063/1.4942791.
[87] M. R. Currie and J. R. Whinnery, “The Cascade Backward-Wave Amplifier: A High-Gain Voltage-Tuned Filter for Microwaves,” *Proc. IRE*, vol. 43, no. 11, pp. 1617–1631, Nov. 1955, doi: 10.1109/JRPROC.1955.277988.
[88] R. Kompfner and N. T. Williams, “Backward-Wave Tubes,” *Proc. IRE*, vol. 41, no. 11, pp. 1602–1611, Nov. 1953, doi: 10.1109/JRPROC.1953.274186.
[89] S. Sengele, M. L. Barsanti, T. A. Hargreaves, C. M. Armstrong, J. H. Booske, and Y. Y. Lau, “Backward-Wave Suppression Analysis, and Design and Fabrication of a Prototype Millimeter-Wave Ring-Bar Slow-Wave Structure,” *IEEE Trans. Plasma Sci.*, vol. 42, no. 12, pp. 3949–3960, Dec. 2014, doi: 10.1109/TPS.2014.2366243.
[90] A. Jassem, P. Y. Wong, D. P. Chernin, Y. Y. Lau, F. Antoulinakis, T. A. Hargreaves, and C. M. Armstrong, “On Johnson’s backward wave oscillation thresholds in TWT,” in *2018 IEEE International Vacuum Electronics Conference (IVEC)*, Apr. 2018, pp. 171–172, doi: 10.1109/IVEC.2018.8391479.
[91] D. Chernin, I. Rittersdorf, Y. Y. Lau, T. M. Antonsen, and B. Levush, “Effects of Multiple Internal Reflections on the Small-Signal Gain and Phase of a TWT,” *IEEE Trans. Electron Devices*, vol. 59, no. 5, pp. 1542–1550, May 2012, doi: 10.1109/TED.2012.2186141.
[92] I. M. Rittersdorf, T. M. Antonsen, D. Chernin, and Y. Y. Lau, “Effects of Random Circuit Fabrication Errors on the Mean and Standard Deviation of Small Signal Gain and Phase of a Traveling Wave Tube,” *IEEE J. Electron Devices Soc.*, vol. 1, no. 5, pp. 117–128, May 2013, doi: 10.1109/JEDS.2013.2273794.

[93] J. C. Lagarias, J. A. Reeds, M. H. Wright, and P. E. Wright, “Convergence Properties of the Nelder--Mead Simplex Method in Low Dimensions,” *SIAM J. Optim.*, vol. 9, no. 1, pp. 112–147, Jan. 1998, doi: 10.1137/S1052623496303470.
[94] B. Levush, T. M. Antonsen, A. Bromborsky, W.- Lou, and Y. Carmel, “Theory of relativistic backward-wave oscillators with end reflectors,” *IEEE Trans. Plasma Sci.*, vol. 20, no. 3, pp. 263–280, Jun. 1992, doi: 10.1109/27.142828.
[95] R. H. Byrd, M. E. Hribar, and J. Nocedal, “An Interior Point Algorithm for Large-Scale Nonlinear Programming,” *SIAM J. Optim.*, vol. 9, no. 4, pp. 877–900, Jan. 1999, doi: 10.1137/S1052623497325107.
[96] D. R. Whaley, R. Duggal, C. M. Armstrong, C. L. Bellew, C. E. Holland, and C. A. Spindt, “100 W Operation of a Cold Cathode TWT,” *IEEE Trans. Electron Devices*, vol. 56, no. 5, pp. 896–905, May 2009, doi: 10.1109/TED.2009.2015614.
[97] D. R. Whaley, B. M. Gannon, V. O. Heinen, K. E. Kreischer, C. E. Holland, and C. A. Spindt, “Experimental demonstration of an emission-gated traveling-wave tube amplifier,” *IEEE Trans. Plasma Sci.*, vol. 30, no. 3, pp. 998–1008, Jun. 2002, doi: 10.1109/TPS.2002.801527.
[98] R. H. Fowler and L. Nordheim, “Electron emission in intense electric fields,” *Proc. R. Soc. Lond. Ser. Contain. Pap. Math. Phys. Character*, vol. 119, no. 781, pp. 173–181, May 1928, doi: 10.1098/rspa.1928.0091.
[99] W. Schottky, “Über den Einfluss von Strukturwirkungen, besonders der Thomsonschen Bildkraft, auf die Elektronenemission der Metalle,” *Phys. Zeitschr*, vol. 15, pp. 872–878, 1914.
[100] J. B. Scott, “Extension of Langmuir space-charge theory into the accelerating field range,” *J. Appl. Phys.*, vol. 52, no. 7, pp. 4406–4410, Jul. 1981, doi: 10.1063/1.329367.
[101] R. T. Longo, “Long life, high current density cathodes,” in *1978 International Electron Devices Meeting*, Dec. 1978, pp. 152–155, doi: 10.1109/IEDM.1978.189375.
[102] R. Vaughan, “A synthesis of the Longo and Eng cathode emission models,” *IEEE Trans. Electron Devices*, vol. 33, no. 11, pp. 1925–1927, Nov. 1986, doi: 10.1109/T-ED.1986.22844.
[103] M. Cattelino and G. Miram, “Predicting cathode life expectancy and emission quality from PWFD measurements,” *Appl. Surf. Sci.*, vol. 111, pp. 90–95, Feb. 1997, doi: 10.1016/S0169-4332(96)00718-0.
[104] J. W. Luginsland, Y. Y. Lau, and R. M. Gilgenbach, “Two-Dimensional Child-Langmuir Law,” *Phys. Rev. Lett.*, vol. 77, no. 22, pp. 4668–4670, Nov. 1996, doi: 10.1103/PhysRevLett.77.4668.
[105] Y. Y. Lau, “Simple Theory for the Two-Dimensional Child-Langmuir Law,” *Phys. Rev. Lett.*, vol. 87, no. 27, p. 278301, Dec. 2001, doi: 10.1103/PhysRevLett.87.278301.
[106] R. J. Umstattd and J. W. Luginsland, “Two-Dimensional Space-Charge-Limited Emission: Beam-Edge Characteristics and Applications,” *Phys. Rev. Lett.*, vol. 87, no. 14, p. 145002, Sep. 2001, doi: 10.1103/PhysRevLett.87.145002.
[107] W. B. LaBerge, R. J. Munick, J. A. Dezoteux, J. F. Whalen, and E. A. Coomes, “Patch Effect for the Thermionic Emission from Polycrystalline Tantalum,” *J. Appl. Phys.*, vol. 26, no. 2, pp. 241–243, Feb. 1955, doi: 10.1063/1.1721967.
[108] C. Herring and M. H. Nichols, “Thermionic Emission,” *Rev. Mod. Phys.*, vol. 21, no. 2, pp. 185–270, Apr. 1949, doi: 10.1103/RevModPhys.21.185.

[109] L. H. Thomas, “Elliptic Problems in Linear Difference Equuations Over a Network,” New York, NY, USA: Columbia University, 1949.
[110] S. D. Conte and C. de Boor, *Elementary Numerical Analysis*. Society for Industrial and Applied Mathematics, 2017.
[111] E. Borie and U. Horcher, “Effect of surface roughness on the velocity spread in electron guns for gyrotrons,” *Int. J. Infrared Millim. Waves*, vol. 18, no. 3, pp. 577–594, Mar. 1997, doi: 10.1007/BF02677996.
[112] K. L. Jensen, D. A. Shiffler, J. J. Petillo, Z. Pan, and J. W. Luginsland, “Emittance, surface structure, and electron emission,” *Phys. Rev. Spec. Top. - Accel. Beams*, vol. 17, no. 4, p. 043402, Apr. 2014, doi: 10.1103/PhysRevSTAB.17.043402.
[113] A. W. Hull, “The Effect of A Uniform Magnetic Field on the Motion of Electrons Between Coaxial Cylinders.,” *Phys. Rev.*, vol. 18, no. 1, pp. 31–57, Jul. 1921, doi: 10.1103/PhysRev.18.31.
[114] P. J. Christenson and Y. Y. Lau, “Transition to turbulence in a crossed-field gap,” *Phys. Plasmas*, vol. 1, no. 12, pp. 3725–3727, Dec. 1994, doi: 10.1063/1.870915.
[115] Y. Y. Lau, P. J. Christenson, and D. Chernin, “Limiting current in a crossed-field gap,” *Phys. Fluids B Plasma Phys.*, vol. 5, no. 12, pp. 4486–4489, Dec. 1993, doi: 10.1063/1.860563.
[116] M. Lopez, Y. Y. Lau, J. W. Luginsland, D. W. Jordan, and R. M. Gilgenbach, “Limiting current in a relativistic diode under the condition of magnetic insulation,” *Phys. Plasmas*, vol. 10, no. 11, pp. 4489–4493, Oct. 2003, doi: 10.1063/1.1613654.
[117] R. V. Lovelace and E. Ott, “Theory of magnetic insulation,” *Phys. Fluids*, vol. 17, no. 6, pp. 1263–1268, Jun. 1974, doi: 10.1063/1.1694876.
[118] J. P. Verboncoeur, M. V. Alves, V. Vahedi, and C. K. Birdsall, “Simultaneous Potential and Circuit Solution for 1D Bounded Plasma Particle Simulation Codes,” *J. Comput. Phys.*, vol. 104, no. 2, pp. 321–328, Feb. 1993, doi: 10.1006/jcph.1993.1034.
[119] P. J. Christenson and Y. Y. Lau, “One-Dimensional Modulational Instability in a Crossed-Field Gap,” *Phys. Rev. Lett.*, vol. 76, no. 18, pp. 3324–3327, Apr. 1996, doi: 10.1103/PhysRevLett.76.3324.
[120] A. L. Garner, Y. Y. Lau, and D. Chernin, “Collapse of cycloidal electron flows induced by misalignments in a magnetically insulated diode,” *Phys. Plasmas*, vol. 5, no. 6, pp. 2447–2453, May 1998, doi: 10.1063/1.872921.
[121] A. Palevsky and G. Bekefi, “Microwave emission from pulsed, relativistic e-beam diodes. II. The multiresonator magnetron,” *Phys. Fluids*, vol. 22, no. 5, pp. 986–996, May 1979, doi: 10.1063/1.862663.
[122] O. Buneman, “Symmetrical States and their Breakup,” in *Crossed-Field Microwave Devices*, New York: Academic, 1961.